RECENT ADVANCES IN CHEMICAL SYNTHESIS METHODOLOGY OF INORGANIC MATERIALS AND THEORETICAL COMPUTATIONS OF METAL NANOPARTICLES/CARBON INTERFACES

by

Andrew G. Harris

Dissertation
Submitted to the Faculty of the
Graduate School of Vanderbilt University
in partial fulfillment of the requirements
for the degree of

DOCTOR OF PHILOSOPHY

in
Chemistry
December, 2015
Nashville, Tennessee

Approved by:
Charles M. Lukehart, Ph.D.
Timothy P. Hanusa, Ph.D.
Borislav L. Ivanov, Ph.D.
Janet E. Macdonald, Ph.D.
D. Greg Walker, Ph.D.

To my loving wife, Tiffany

ACKNOWLEDGMENTS

I would like to thank my supervisor, Professor Lukehart, who always made time to discuss anything I was interested in discussing. He always encouraged me to pursue any project or idea I found interesting. In addition to all his guidance on matters of Chemistry, he provided me with well-rounded discussions on many life topics. I would also like to thank my committee members, Drs. Timothy Hanusa, Borislav Ivanov, Janet Macdonald, and Greg Walker, for keeping me focused and on goal.

I want to thank my fellow Lukehart group members, past and present, for providing a foundation from which to go forward and a sounding board for ideas along the way.

Finally I couldn't have made it through graduate school without the love and support of my family. My loving wife, Tiffany, for her willingness to follow me across the world and back, and for her love and support all along the way. My parents for fostering my thirst for knowledge and never letting me settle for 'good enough'. And most importantly God, for all the talents he has given me and for surrounding me with so much love and support.

Research is not possible without financial support. Student stipend support was provided through the National Science Foundation Graduate Research Fellowship (NSF DGE-0909667). This research was also supported in part by grants provided by TNSCORE Thrust II (NSF EPS-1004083), Savannah River National Laboratory, NSF Nordic Research Opportunity (NSF DGE-0909667 Amendment 006), and the Vanderbilt University IDEAS grant program.Efforts at Vanderbilt University were conducted in collaboration with Savannah River National Laboratory. The university effort was funded under subcontract #0000163498 with Savannah River Nuclear Solutions, LLC and conducted within project #SR13-MRFM-1-PD1Ab funded by the National Nuclear Security Administration, office of Defense Nuclear Nonproliferation.

TABLE OF CONTENTS

Chapter

Appendix

LIST OF FIGURES

LIST OF TABLES

LIST OF ABBREVIATIONS

acac	acetylacetonate
AFM	atomic force microscope/microscopy
CPCD	confined-plume chemical deposition
DFT	density functional theory
DOS	density of states
EDS	(x-ray) energy dispersive spectroscopy
Et	ethyl
fcc	face-centered cubic
FEL	free electron laser
FWHM	full width half maximum
GCNF	graphitic carbon nanofiber
HR	high resolution
IR	infrared
LCAO	linear combination of atomic orbitals
MEA	membrane electrode assembly
MRFM	magnetic resonance force microscope/microscopy
NMR	nuclear magnetic resonance
PBE	Perdew-Burke-Ernzehof
PDF	powder diffraction file
PDOS	projected density of states
PEMFC	polymer electrolyte membrane fuel cell
PL	photoluminescence
Pr	propyl
RPM	rotations per minute
SAED	selected area electron diffraction
SCLS	surface core level shift

SEM	scanning electron microscope/microscopy
SRNL	Savannah River National Lab
STP	standard temperature and pressure (25 °C and 1 atm)
TEM	transmission electron microscope/microscopy
THF	tetrahydrofuran
UHMWPE	ultra-high molecular weight polyethylene
xc	exchange and correlation
XRD	(powder) x-ray diffraction/diffractometer

CHAPTER I

GENERAL INTRODUCTION

Materials Science

Materials science is a multidisciplinary science incorporating chemistry, physics, and engineering. The field utilizes synthesis techniques from all branches of chemistry to make materials that are relevant to solving problems in every field of the physical sciences. Four major elements make up the traditional materials science tetrahedron (MST) which guides research in materials chemistry: synthesis, structure, properties, and performance, see Figure 1[1]. Synthesis strategies must be accessible by a wide range of scientists and engineers. The composition and structure of a product must be closely controllable. And finally the product must perform within its application area; it must have a particular set of properties that fulfill some niche. Not all of these goals can be optimized at one time, but generally any foray into the field addresses one or more of these goals.

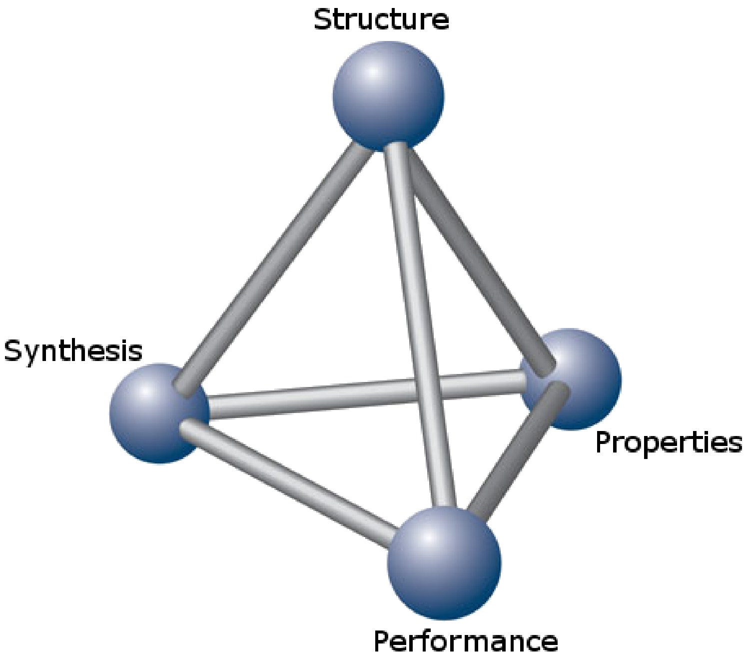

Figure 1: The Materials Science Tetrahedron as proposed by the COSMAT in 1974.

In seeking to address current problems, material chemists focus on making new materials. This involves synthesis strategies from both organic and inorganic chemistry, as these new materials often incorporate both aspects to make a product with tunable and wieldy properties somewhere between a traditional inorganic or organic product. Research endeavors are often at the intersection of these two fields, e.g. proton electromotive membrane research focuses on generating metal nanoparticles, immobilized on a polymer bead[2] or other carbonaceous support[3]. Some of the higher performing catalysts for fuel cells involve immobilizing platinum or platinum-ruthenium alloy on electrically conductive carbon supports.[3] As another example, current research into high magnetic susceptibility particles utilizes organometallic precursors and organic reducing agents to form lanthanide metal nanoparticles suspended in a fluid.[4]

While synthesizing new materials is important, having control over the composition and structure of these materials can be even more important. These two concepts are interrelated in the sense that control usually comes from the synthesis method, but the structure or composition can also be controlled post-synthesis by other methods. For example, chunks of lanthanide metal can be ground down to smaller particles and then using microwave heating, the particles can be rounded. Catalysis applications frequently require control over the structure of materials as well. In catalytically active materials, usually only one or a few crystallographic facets are strongly active.[5] This observation means that controlling particle structure to produce more of the catalytically active facets exposed to the surface will increase activity and turnover rate of the overall material.

Finally the performance of any material must be optimized, which involves tweaking the properties. This idea again is interrelated to the other goals, but usually cannot be optimized at the same time. For Magnetic Resonance Force Microscopy, high magnetic saturation as well as appropriately sized particles that are stable under imaging conditions are desirable.[6] Magnetic saturation is an intrinsic property of a given material, but after picking a material with high saturation, the size and stability can be tuned. These properties of materials can be optimized by using capping layers, changing from bulk materials to micro- or nanoparticles, or other techniques that do not necessarily change the identity of the material.

Synthesis Techniques and Current Problems

Synthesis techniques can be broken down into three major categories: wet techniques, physical techniques, and a combination of the two techniques. Wet techniques[7] include solution reduction[8,9], metathesis of dissolved ions[10], and any other techniques which utilize a solvent in a non-solid phase[11]. Physical techniques[12] usually involve elements in their pure state reacted at high temperature and/or pressure. The combination of the two would include things like precursor synthesis (a wet technique) followed by tube furnace decomposition (a physical technique), or sol-gel synthesis, where a solution is usually evaporated down to a gel (wet technique) and then subjected to high temperature to dehydrate the product completely and cause densification to the final desired material (physical technique).

Wet techniques usually provide for better control over the composition and structure of the final materials than physical techniques. Usually when a new material is initially sought with a specific composition, a physical technique will be employed. By mixing the elements in an appropriate stoichiometric ratio and allowing them to react under high temperature and/or pressure, the desired final phase can be created, but it will be a bulk material and will be the most thermodynamically stable phase. With wet techniques, metastable phases as well as lower temperature phases of materials become feasible to produce. However many times the most thermodynamically stable phase of system is desirable, while keeping the energy cost to produce it low. In these situations a combination of the two techniques may be best.

These two techniques however do not allow for control over all aspects that will need to be controlled for future materials development. There have been some forays into solving these problems. For instance, microwave synthesis[13,14] is still a physical technique, but the heating and cooling times are much more rapid than a typical tube furnace synthesis[15]. This allows for not only rapid synthesis of materials, but with the short cooling times, it is sometimes possible to trap meta-stable or high-temperature materials and study them under STP.

Material scientists desire more control over synthesis than can be provided by these techniques. With current physical techniques, new compounds can be made at the correct stoichiometry and phase, but controlling the interface between materials and the facets present in the materials is very difficult. Wet techniques allow for more control over the facets present in the materials, but interfaces between particles and their support or two quite different materials is still very difficult. New techniques are needed that allow for more control, which may not replace old techniques, but enhance materials research and the options available.

Current Research Endeavors

A step towards developing a new synthesis technique has been made in the Lukehart group, namely Confined-Plume Chemical Deposition (CPCD)[16]. This method is also a type of physical technique, with even more accelerated synthesis than microwave methods. Using a laser to generate a plasma pulse between two confining media, the reaction is confined both spatially and temporally. This confinement helps generate exotic phases not normally observed at such mild conditions in extremely short period of time. CPCD has been used to synthesize ReB_2 directly on a Kevlar fiber polymer support. This is noteworthy because the temperatures needed to form ReB_2 are typically around 3000 K, but Kevlar will melt and decompose around 750 K. This must mean that while enough energy is present in the system to form ReB_2, the local temperature of the Kevlar fibers never goes above 750 K. Also of note from this experiment was the tight interfacial interaction of ReB_2 to the Kevlar fibers, which has not been seen and is not possible by other methods. Finally no special conditions are needed during this synthesis, such as cooling plates, high vacuum, or special atmospheric gases like nitrogen or argon. CPCD is performed in open air with the application of precursors and assembly of the confining media all taking place at normal conditions. Even if final products are moderately sensitive to air or humidity, the system is usually stable enough to be extracted from the confining media and coated with a protecting layer like sputtered gold or a spin-coat polymer.

Since the initial discovery and development of CPCD within the Lukehart group, continuing strides have been made to bring this technique to general applicability in materials research. Using CPCD, metals on both hard and soft supports have been synthesized, ceramics on both hard and soft supports have been synthesized, and some exotic patterning has been investigated. The coatings made by CPCD are not typically atomically smooth, but more like particles that are closely packed together. This type of coating is great for increasing durability or putting particles on a surface. Applications and properties of materials synthesized by CPCD are still under investigation.

Utilizing standard techniques to achieve novel results is another research interest within the Lukehart group. When simple metal nanoparticles are desired, solution reduction is still one of the best techniques[17]. By dissolving the correct elements into a solution and then reducing the compounds that contain those elements, metallic particles can be produced that can be well-controlled in structure and composition. The reduction potential needed for a compound as well as the reducing power of the reducing agent must both be considered and matched in solution reduction synthesis. Generally transition metals are not too difficult to reduce with reduction potentials in the range of +2 to -1.5 eV[18]. The rare-earth elements tend to be a lot more difficult to reduce with reduction potentials closer to -2.5 eV[18]. This means that more powerful reducing agents have to be used for rare-earth elements than transition metals, including sodium naphthalenide, sodium benzophenide, and potassium(15-crown-5)sodide[18]. Choice of precursor molecules also has a strong influence on the reduction potential as well as the final product. Too many ancillary elements can lead to introduction of undesired dopants in the final material.

Developing new techniques is a much needed step within materials chemistry; however, without target materials to aim for, it is difficult to know in what direction to start looking. Studying chemical reactions and possible precursors is best accomplished using theoretical frameworks. Density Functional Theory (DFT) is one such framework, and it is used to investigate the ground-state electronic structure of many-body systems[19]. DFT is modeled by using a spatially dependent electron density acting on a virtual single-body that represents the system of study. Traditional quantum mechanics quickly becomes intractable when many different atoms are present in large cells, but DFT handles this by simplifying the model under study. Instead of a system with many atoms, the system is represented as a kind of single-body problem using electron density. All of the properties of interest can be calculated as a function of this electron density and agree well with the experimental values for the system. The types of functionals used to represent this spatially dependent electron density must be chosen carefully to facilitate computationally reasonable systems for study.

Characterization Methods

Materials chemists use many tools to study the systems of interest to them. Whether that system is bulk scale or nanoscale, similar tools are used to fully characterize the system and facilitate further refinement and experimentation. The properties of these materials depends on their chemical composition, structural arrangement, size of particles or crystallite domains, and surface structure. Methods used herein include powder x-ray diffraction (XRD), scanning electron microscopy with energy-dispersive x-ray spectroscopy (SEM-EDS), transmission electron microscopy with energy-dispersive x-ray spectroscopy (TEM-EDS), and photoluminescence (PL) spectroscopy. For details on more physical chemistry characterization methods see *Characterization of Nanophase Materials*, Zhong Lin Wang, Ed. (Wiley- VCH:2000)[20]

Powder X-Ray Diffraction (XRD): XRD is a simple but powerful technique to characterize solid-state materials. It yields information about phase identification, purity, and crystallite domain size, including particle size for small particles. Using x-rays to bounce off of planes of atoms within a crystalline material, XRD generates a unique signal for every constituent in a sample, and can be used to measure purity and oriented growth.

X-Rays are generated from a metal sheet, usually copper, by high-energy electrons that are thermally ejected from the cathode, usually tungsten, to the metal plate. These electrons eject core level electrons; to fill these core vacancies, valence electrons relax and emit x-rays characteristic of the materials energy structure. In modern XRD instruments undesired wavelengths are removed from analysis by using a detector that is only sensitive to a specific range of energies that correspond to a small window of x-ray wavelengths. This arrangement allows for more signal to be generated and collected than the traditional monochromators used previously.

X-Rays are diffracted by planes of atoms within the crystalline material and can be expressed in terms of the Braggs equation:

$$2 \cdot d_{hkl} \cdot \sin\theta = n \cdot \lambda$$

Where d_{hkl} is the spacing between lattice planes for a set of Miller indices (hkl), θ is the angle of the incident x-ray relative to the surface, and λ is the wavelength of the x-rays. According to this equation the maximal signal is generated at certain lattice parameters and indices for a particular diffraction angle. These maxima are what is unique about each sample. Using the maximal signal locations, it is possible to identify which phases of crystalline material are present in the sample. Sample identification is carried out by comparing these peaks in intensity to powder diffraction files (pdf) compiled by the Joint Committee on Powder Diffraction Standards (JCPDS).

Crystallite domain size or, if the particle is small enough, particle size can also be determined from XRD. Typical bulk samples have very narrow peaks indicating a rather homogeneous long-range distribution of the atomic planes they represent. The reason for the intense peak and short tail is the interaction of x-rays from different layers on a single plane. There is maximum constructive interference at the peak and as the x-rays moves farther from this angle, destructive interference quickly dominates sending the signal back down to baseline. However, for small crystallite domains and especially small particles the destructive interference is not as strong and can contribute to peak broadening. Usually this is modeled by the Scherrer equation:

$$\tau = \frac{\kappa \cdot \lambda}{\beta \cdot \cos\theta}$$

Where τ is the mean size of ordered crystalline domains, κ is a shape factor, close to 0.9 for spherical domains, λ is the x-ray wavelength, β is the line broadening at half maximum intensity (FWHM) in radians, taking into account instrumental line-shape broadening, and θ is the angle of the x-ray to the plane of the surface. Scherrers equation only gives a lower bound on the size, because there are many factors other than domain size that contribute to the broadening of a line. These other factors include inhomogeneous strain and crystal lattice imperfections. Usually these contributions are very minor and can safely be assumed to be near zero, but confirmation of crystallite size by TEM is recommended.

Electron Microscopy (SEM and TEM): Scanning Electron Microscopy (SEM) can achieve around 1nm resolution of a sample and provides a detailed picture of the surface of a sample. SEM is capable of 40x all the way to 100,000x magnification, meaning that details from centimeters down to a few nanometers can all be seen. Also the depth of field is very high, meaning many features can be brought into focus at the same time, giving a better picture of the sample than traditional optical microscopy. Transmission electron Microscopy (TEM) can achieve around 100 pm resolution of a sample and provides very detailed information about the entirety of the sample. As the name implies, TEM requires that a sample is at least translucent to an electron beam. TEM is capable of 50x down to 1,000,000x magnification. This means that information can be gained about individual atoms up through to conglomerated particles in a sample.

Both SEM and TEM use a focused beam of electrons to generate their images. SEM images are generated by the secondary electrons emitted by atoms at the surface of the sample. TEM images are collected from the electrons that pass through the sample. Both techniques can also use a Z-contrast mode, called back-scattered electron (BSE) imaging; in order to perform BSE imaging in TEM a high angle detector must be present above the sample and the beam must be focused to a narrow point and used in a scanning mode called scanning transmission electron microscopy (STEM). Z-contrast is based on the atomic number (Z-number) of the elements in the sample, where heavier atoms (those with higher Z-numbers) back-scatter more electrons than lighter atoms (those with lower Z-numbers).

TEM can also be operated in an electron diffraction mode, called selected area diffraction (SAD), which is similar to XRD. If a single crystal sample is present, atomic planes are represented by spots instead of the rings present in polycrystalline samples. The distance of these spots from the center of the beam, along with the angle between spots, gives exact crystallographic information about the location of atomic planes and the relative orientation between different planes.

Energy-dispersive X-ray Spectroscopy (EDS): EDS gives the elemental composition of a sample by measuring the characteristic energy of x-rays emitted by elements within a sample hit by highly energetic electrons. EDS is usually performed as part of either SEM or TEM imaging. The area of each peak is correlated with the relative amount of each element present in the sample, and so EDS can be used to quantitatively identify the constituent elements in a sample.

EDS works by bombarding a sample with highly energetic electrons. These incident electrons eject core electrons from atoms in the sample. Valence electrons then relax into the core and emit characteristic x-rays for each element. Depending on which core electrons are removed, different characteristic signals are generated; these signals are named according to the relative energies of the shells in which they reside. The first shell is called the K shell, the second is called L, the third M, and so on. An electron from a higher energy shell must relax into the shell with the hole to generate the x-ray signal. Most EDS are not sensitive enough to differentiate between transitions from different subshells within the primary shell; however, transitions between different primary shells give rise to different lines. For instance a transition from L to K (or any two adjacent shells) is designated K_α (or the alpha transition of the final state), whereas a transition from M to K (or any shell separated by one intermediate shell) is designated K_β (or the beta transition of the final state), and finally a transition from N to K (or any shell separated by two intermediate shells) is designated K_γ (or the gamma transition of the final state).

Photoluminescence (PL) Spectroscopy: PL spectroscopy measures how much light is emitted by a sample after irradiation at a specific wavelength. This technique is good for detecting dopant molecules and their surrounding chemical or physical environment, which can strongly affect the luminescence wavelength and/or intensity observed.

Luminescence is the process whereby a molecule absorbs energy and subsequently emits light. Using a photon source, such as light, to excite the molecule so that it emits a different wavelength of light is called photoluminescence. If the lifetime of luminescence is short (on the order or a second or less) the process is called fluorescence, but if it is long (on the order or minutes or hours) the process is called phosphorescence. A spectrofluorimeter is used to measure photoluminescence. It comprises two spectrometers, one to measure the wavelength of light illuminating the sample and the other to analyze any fluorescence. First a standard absorption spectrum is measured to find where the sample absorbs energy to possibly luminesce, then each peak is investigated by fixing the illuminating light at each peak wavelength successively and scanning the luminescence spectrometer across all wavelengths. The absorption spectrum is called the excitation spectrum and the luminescence spectrum is called the emission spectrum. The difference in wavelength between the excitation wavelength and the emission wavelength on a particular transition is referred to as Stokes shift.

There are several ways for excited molecules to return to the ground state. Luminescence is a radiative process with emission of a photon. Competing with luminescence are radiative and nonradiative transfers to other molecules or compounds within the sample. A Stokes shift occurs because after excitation, the molecule relaxes to the lowest vibrational level on the excited state before relaxing back to the ground state through photon emission. Nonradiative transitions between excited and ground optical states are undesirable and should be suppressed. Heat (vibrational relaxation) is the major nonradiative decay process. Concentration quenching, one radiative loss mechanism, occurs through a cross-relaxation process whereby some energy from atom A is lost through nonradiative processes until there is a match to an available energy level in nearby atom A$'$. Then the energy is transferred to A$'$ and it relaxes through another set of nonradiative processes.

It is possible to measure fluorescence lifetime (FLT) as well. FLT is an extremely sensitive technique that gives an absolute (concentration independent) measure of system fluorescence properties. PL measurements (intensity vs wavelength) gives an ensemble average and relative (concentration dependent) representation of these fluorescence properties. FLT spectra can be obtained in either the time domain or the frequency domain. FLT measurements in the time domain involve a pulse of energy that causes the system to fluoresce and then measuring intensity vs time for the ensemble system to decay back to 1/e (about 36.8%) of the peak signal. This pulse of energy should be very short to ease the analysis, so usually either a pulsed LED or a short laser pulse (on the order of picoseconds or less) is used. If the excitation pulse is on the same order of magnitude as the fluorescence lifetime, then complicated deconvolution methods must be used to remove the effect of the pulse from the fluorescence intensity measurement. FLT measurements in the frequency domain involve varying the intensity of the excitation source sinusoidally and measuring the phase difference between excitation and emission intensity. By measuring this phase difference over many frequencies it is possible to extract the lifetime and distribution of states in the system.

Research Aims and Goals

Computational modeling, preparation, and characterization of nano- and micro-sized materials are the broad goals of the research being presented in this dissertation. The aims are to extend novel synthesis techniques developed within the Lukehart group, to prepare new compounds, and to use standard soft chemistry techniques to prepare novel materials for use in magnetic imaging. six main research projects were carried out:

- Anchoring of Pt and PtRu to Cup-stacked Carbon Nanofibers Studied by Density Functional Theory. Using Density Functional Theory (DFT) the interface of metal nanoparticles to cup-stacked carbon nanofibers were modeled and studied for binding interactions and characterization signatures. An introduction to DFT and the systems modelled in this study as well as the results and characterization of this study are presented in Chapter II.

- Influence of External Magnetic Field on Confined-Plume Chemical Deposition of Iron Oxide Nanoparticles Using Femtosecond NIR Laser Irradiation: Chain-like Nanoparticle Alignment in a Fluid Medium. Chain-like aggregates of nanoparticles were prepared by Confined-Plume Chemical Deposition (CPCD). An introduction to CPCD and Fe_3O_4 deposited by different methods under magnetic influence as well as experimental results for aligning Fe_3O_4 with magnetic fields oriented in different directions relative to the scanning of the laser beam are presented in Chapter III.

- Confined-Plume Chemical Deposition of Gold Particles on Onion (*Allium cepa*) Tissue: Particle Localization Similar to Hydrothermal Polyol Deposition. Gold particles are deposited directly on onion tissue by CPCD. An introduction to metals on biological supports as well as experimental results for depositing gold particles selectively along the cell wall of onion tissue are presented in Chapter IV.

- Preparation of Surface-Passivated Lanthanide Metal Micropowders for Magnetic Resonance Force Microscopy. Dysprosium particles formation is explored by different synthesis methods. An introduction to Magnetic Resonance Force Microscopy (MRFM) and lanthanide particle synthesis as well as experimental results of two failed and one successful formation procedure of dysprosium microparticles coated with a platinum capping layer are presented in Chapter V.

- Preparation and Photoluminescence Characterization of Yttrium Borate Powders Doped with Lanthanide Phosphors. Yttrium borate powders doped with lanthanide phosphors (YBO_3:Ln) were prepared by Confined-Plume Chemical Deposition (CPCD). An introduction to CPCD and YBO_3:Ln materials as well as experimental results for YBO_3:Ce and YBO_3:Eu are presented in Appendix A.
- Laser-Beam Shaping Through Shadow Masking and Cylindrical Optics. A mask shape to turn a Gaussian beam into a flattop beam is calculated. An introduction to beam shaping and the methodology used to measure beam shape as well as experimental and theoretical results of a mask shape over a Gaussian beam that is then focused through cylindrical optics are presented in Appendix B.

CHAPTER II

ANCHORING OF PT AND PTRU TO CARBON NANOFIBERS STUDIED BY DENSITY FUNCTIONAL THEORY CALCULATIONS

Density Functional Theory: General Introduction

Density Functional Theory (DFT) is used to model the electronic structure of many-bodied systems. This is accomplished by modelling the many-electron system as a functional of the spatially dependent electron density. DFT is among the most popular and versatile methods available in computational chemistry. DFT is now able to model solid-state systems quite well, and most of the properties calculated agree satisfactorily with experimental data.[19]

Since DFT uses a functional of the spatially dependent electron density, it must be corrected for exchange and correlation (xc) interactions. This xc interactions corrects for the indistinguishable properties of fermion particles, like an electron, see discussion below. XC correction is accomplished in the current work using the spin polarized Perdew-Burke-Ernzerhof (PBE) approximation for the xc functional.[21] Ultra-soft scalar-relativistic pseudopotentials are used to describe the interaction of valence electrons with core electrons.[22] Plane-waves are used to describe the spatially dependent electron density. Exchange energy is a strictly quantum mechanical effect between two indistinguishable particles, broadly classified as either fermions or bosons.[23] Fermions include particles which cannot share quantum states such as electrons, protons, and neutrons; however, bosons are particles which can share quantum states, such as photons and alpha particles. Theses quantum states, also called wave functions, give rise to the indistinguishable particles either changing signs (for antisymmetric particles, which are bosons) or remaining unchanged (for symmetric particles, which are fermions) when they are statistically exchanged. Since the particles cannot be distinguished, calculations have to include each of the particles occupying every possible configuration of the wave functions. For fermions this exchange energy gives rise to the distance between the wave function of two indistinguishable particles that should overlap to be greater than the expected value for two distinguishable particles from classical mechanics, and for bosons the expectation value for the distance is lower than for two distinguishable particles in classical mechanics.

Using ultra-soft scalar-relativistic pseudopotentials to describe the interaction of valence electrons with core electrons gives a more accurate representation of the charge density within the atoms. Pseudopotentials are used to replace actual all-electron potential calculations because they require less computing power and generate far fewer nodes for the valence electrons of interest at the core. Pseudopotentials also allow for easier plane-wave constructions of the basis sets. All core electrons are effectively frozen and only the net charge experienced by the valence electrons is used in the calculations with pseudopotentials, which allows for the coulombic potential in the Schrödinger equation to be replaced by a modified effective potential term. Ultra-soft pseudopotentials are used to increase transferability of charge from core electrons to valence electrons, since this pseudopotential construction does not require that all wave functions within the cutoff exactly equal the all-electron potential, like norm-conserving pseudopotentials. Ultra-soft pseudopotentials also allow for easier construction of the pseudo-wave functions with a plane-wave basis function for highly localized valence electrons. Scalar-relativistic pseudopotentials are better able to predict all relativistic properties of atoms besides spin-orbit coupling than previous non-relativistic self-consistent calculations. Spin-orbit coupling is not well modeled by any computationally simple approximations. Scalar-relativistic pseudopotentials approximate the Dirac equation by dropping the spin-orbit coupling term entirely. This immensely speeds up computation while only sacrificing the relatively small effects of the spin-orbit coupling for relativistic (that is heavy or high Z) atoms.

Pt and PtRu Pure Metal and Carbon Interface Models

The polymer electrolyte membrane fuel cell (PEMFC) is a potential technology for future energy conversion in sustainable energy systems.[24,25] By using hydrogen, methanol or formic acid from renewable energy sources and oxygen from the air, fuel cells produce electricity with water and carbon mon-/di-oxide as the main exhaust. Electrode catalysts in the PEMFCs are generally based on platinum. One issue with platinum in low-temperature applications is, however, that the metal is poisoned by CO. Carbon monoxide may be present in trace amounts in the gas feed or may form during the fuel cell reactions. Alloying platinum with ruthenium has been shown to modify the electronic structure and enhance the CO tolerance.[26–29] PtRu particles supported on carbon nanofibers have been reported to have higher activity as anode catalysts in proton exchange membrane fuel cells than conventional catalysts. In a recent study of the effect of carbon supports on fuel cell catalyst performance, the Lukehart group determined narrow herringbone graphitic carbon nanofibers were the best performing supports.[3]

The target system to be modeled are about 6 nm particles and HR-TEM analysis shows these particles are crystallites that expose low index facets to the surroundings.[3] Systems considered include the low energy surfaces (111) and (100) anchored to the exposed edges of cup-stacked carbon nanofibers.[3,30,31] The nanofibers can be viewed as stacked graphene cones, so it is reasonable to represent the carbon support by a single graphene layer. The metal-carbon interface then is modeled by metal surface slabs attached to the edge of a graphene layer. This is justified because the interaction between the graphitic sheets is of van der Waals type and neighboring sheets do not affect the anchoring. It should be noted that the adhesion of a metal surface to the basal plane of graphene is weak and that particles attached in such configurations should sinter at low temperatures. (For reference we explicitly investigated Pt(111) adhered to graphene using a metal (6 x 6) cell which corresponds to a lattice mismatch of only 1.4 percent, and the adhesion energy was calculated to be 0.001 $\mathrm{eV\,Å^{-2}}$.)

The number of electrons treated variationally for each element are: Pt(10), Ru(16), C(4) and H(1). A plane-wave kinetic energy cut-off of 28 Ry is used to expand the Kohn-Sham orbitals. Reciprocal space integration over the Brillouin zone is approximated with finite sampling that correspond to a spacing smaller than 0.041 $\mathrm{Å^{-1}}$ for all considered systems.

As equilibrium nanoparticles adopt shapes according to the Wulff rule, particles larger than 3 nm are conveniently modeled by extended surfaces.[32] Here, the metal-graphite interface is investigated for the two common crystal planes, namely (111) and (100). The surfaces are represented by five atomic layers. Repeated slabs (metal and carbon) are separated by at least 11 Å of vacuum. Structural optimization is performed with the two bottom layers constrained to the theoretical bulk positions. The structures are regarded as converged when the largest element of the energy density gradient is lower than 0.03 $\mathrm{eV\,Å^{-1}}$, the change in energy is less than 10^{-5} eV/atom, and the change in atomic coordinates is smaller than 10^{-3} Å.

The interaction energy, ΔE, between the graphene support and the metal slab is calculated according to:

$$\Delta E = \frac{1}{L}(E_{C/Pt} - E_{Pt} - E_C)$$

Where, the energy of the bare metal (E_{Pt}) and isolated carbon sheet (E_C) are subtracted from the total energy of the interface ($\mathrm{E}_{C/Pt}$). The interaction energy is normalized with respect to the length of the unit cell (L) to make calculations comparable across different lattices. It is also instructive to consider the metal-carbon bond strength, where instead of the cell length, the energy difference is normalized to the number of metal-carbon bonds.

Surface core-level shifts (SCLS) give valuable information on the exact oxidation state, bonding environment, and identity of elements at the surface, or interface, of a sample. SCLSs can be evaluated theoretically within DFT as well by using a pseudopotential that accounts for an electron hole in the appropriate core shell of relevant elements. For carbon the hole is generated in the 1s-shell[33], while in platinum and ruthenium the Z+1 approximation is used[34], meaning platinum and ruthenium will be modelled with gold and rhodium pseudopotentials respectively. This approximation is valid because a core missing an electron can be seen as just having another positive charge in its nucleus, which is exactly what the next element in the periodic table has for a nucleus. These approaches include final state effects and assume complete screening of the core-hole. The SCLSs are calculated with respect to a bulk reference, represented by an atom in the center of the slab for the metal or center of the graphene sheet for the carbon.

For reference two metal systems were considered, monometallic Pt and the PtRu random alloy. The lattice constant of face centered cubic (fcc) Pt is calculated to be 4.00 Å. When the xc-functionals used are applied to bulk crystal systems, the theoretical lattice constant is usually slightly expanded (2%)with respect to the experimental lattice constant, which is exactly what is observed.[35] Ru has a hexagonal lattice and the lattice constants are calculated to be a,b=2.72 Å and c=4.28 Å, which agrees reasonably with the experimental lattice constants. The random PtRu alloy has a Pt_1Ru_1 stoichiometry and adopts the fcc lattice of Pt.[36] Since true randomness is hard to achieve, 100 semi-random configurations with a 1:1 Pt:Ru composition in a large cell containing 32 atoms were used to test the effect of atomic arrangement on ground state energy. The cell size was chosen to be the measured Pt_1Ru_1 lattice constant (3.88 Å[37]), expanded by 2% to account for the known effects of the chosen xc-functional. The energy difference between the highest and lowest energy configuration was calculated to be 0.03 eV/atom. This small difference in energy indicates that many configurations are experimentally possible. A common structural motif for the lowest energy configuration is having a vein of Ru surrounded by Pt. The Pt atoms are on average bonded to 5.8 Ru atoms and 6.2 Pt atoms. The structure with the lowest energy was used to optimize the lattice constant of PtRu. This constant was found to be 3.92 Å, which is within the 2% expansion expected.

The effect of constraining the lattice constant was investigated further to validate our assumptions. First an index of randomness was needed to evaluate how structures should compare to one another. For this a randomness index was defined as:

$$randomness = \sum_i min_i\left(S, D\right)$$

The sum runs over all 32 atoms in the cell and for each atom i, S is the number of nearest neighbors of the same element as compared to i and D is the number of nearest neighbors of different elements as compared to i. Having six same and six different neighbors is the most random case, which gives a theoretical randomness of 192 for the 32 atoms present; however due to periodic boundary conditions, it is actually impossible to achieve such a configuration. An atom having 8 different element neighbors and 4 same element neighbors will contribute the same effect to the index as an atom having 4 different element neighbors and 8 same element neighbors, namely contributing 4 to the sum. To test the assumption that structural relaxation was unnecessary to find the optimal configuration, 26 configurations were completely relaxed. The energy differences for these configurations are collected in Table 1. The greatest energy difference is 0.05 eV/atom within the 26 cases tested, which include configurations sampled from the entire energy distribution of the original 100 structures. Analysis of Table 1 indicates that all the configurations are still very random, and while the lowest energy configuration now changes, the structural motif is still very similar to the optimal structure used in this study.

Even with a bulk PtRu random alloy, it is likely that segregation occurs at the surface. In order to investigate this possibility, different configurations of the (111) surface were explored. To facilitate direct comparison of the different systems, the 1:1 ratio of Pt:Ru was kept constant. Four different cases were studied: (i) only Pt

Structure	Random Index	ΔE/atom Fixed	ΔE/atom Optimized
59	162	0	0.0197
41	164	0.0023	0.0095
16	164	0.0061	0.0007
35	168	0.0064	0.0052
74	168	0.0075	0.0198
36	162	0.0095	0.0203
91	166	0.0099	0.0239
69	168	0.0102	0.0147
21	168	0.0112	0.0034
89	148	0.0117	0.0010
53	168	0.0122	0.0146
99	160	0.0137	0
86	160	0.0152	0.0287
12	168	0.0163	0.0317
25	170	0.0168	0.0360
98	156	0.0174	0.0205
27	158	0.0191	0.0284
68	168	0.0193	0.0209
42	164	0.0193	0.0369
38	168	0.0215	0.0469
51	154	0.0220	0.0316
90	164	0.0231	0.0341
2	150	0.0249	0.0397
58	164	0.0261	0.0515
33	168	0.0276	0.0460
56	160	0.0339	0.0384

Table 1: PtRu random alloy configurations with and without complete optimization

in the top layer (with only Ru in the second layer) with a Pt_1Ru_1 core, (ii) only Ru in the top layer (with only Pt in the second layer) over a Pt_1Ru_1 core, (iii) a core-shell configuration with Pt at the surface, and (iv) the stoichiometric Pt_1Ru_1 surface. These calculations were carried out with slabs of 10 layers each. The structures and their relative energies are shown in Figure 2. The case with only Pt in the surface layer was energetically preferred, whereas segregation of Ru is calculated to be highly energetically disadvantageous.

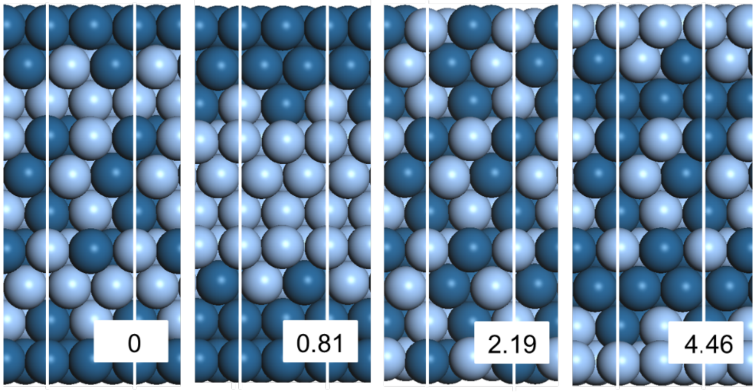

Figure 2: Investigated structures for surface segregation in a 1:1 Pt:Ru alloy. The energies are given with respect to the structure to the left. White lines indicates the p(2x2) surface cell. Atomic color code: Dark spheres (Pt) and bright spheres (Ru).

Experimentally, the metal particles are known to bind to the carbon sheets with a 30° angle to the surface normal.[38] Both the canted and the perpendicular interface between carbon and metal were investigated. The potential energy surface with respect to the angles of interaction investigated is flat. Figure 3 shows the canted graphene sheet with zigzag termination of Pt(111), while Figure 4 shows the perpendicular interface between graphene with zigzag termination and Pt(111). The optimum angle was found to be 29° to surface normal. This configuration is similar in energy (0.1 eV/carbon bond) to the perpendicular configuration (−0.03 eV/carbon bond).

The lattice constant of the graphene sheet was calculated to be 2.46 Å, which is in perfect agreement with previous theoretical studies using similar computational approximations.[39] In the calculations of the anchored nanoparticles, the graphene sheet

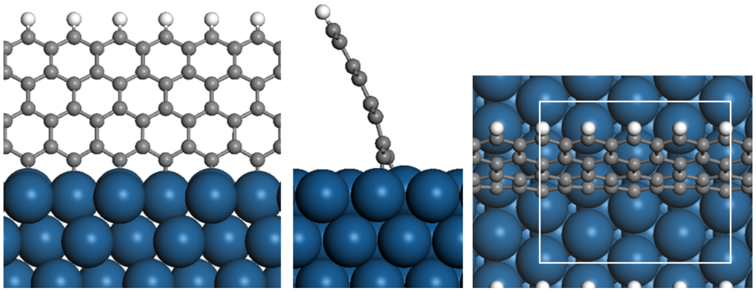

Figure 3: Zigzag graphene interfacing with Pt(111) at 29°

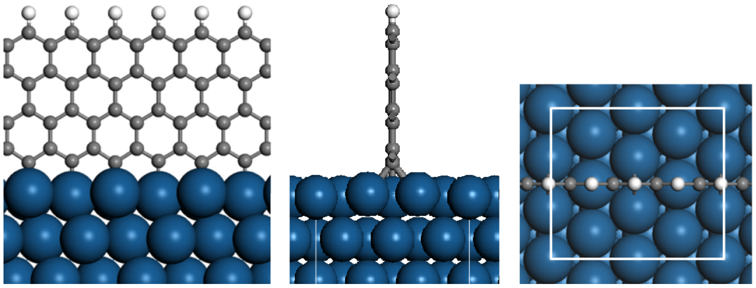

Figure 4: Zigzag graphene interfacing with Pt(111) at 0°

is periodic in one direction and truncated in the second. Three layers of hexagonal carbon units were used and the edge exposed to the vacuum was terminated with hydrogen. Three layers of hexagonal carbon units was found to sufficiently represent the bulk graphene sheet by studying hydrogen-saturated graphene flakes of different sizes. It was found that the carbon-carbon bond distance in the center of these flakes converged to 1.42 Å, which is the nearest neighbor distance observed in two dimensional graphene flakes, when there were three layers of hexagonal carbon units to the perimeter. Two different types of termination on the graphene sheets were considered, namely zigzag and armchair. The carbon nanofibers have edges that contain both of these terminations in order to form a cone.[31,40]

The metal-carbon interfaces were constructed so as to minimize the lattice strain in the two components. To achieve this goal as well as keep the slab sizes reasonable, the Pt(100) surface was modeled with either a (7x2) or (6x2) surface cell and the Pt(111) surface with either a (3x3) or (3x2$\sqrt{3}$)rect surface cell. These choices of surface cell afford a lattice mismatch between platinum and carbon in all cases below 1.6%. For the PtRu alloy, only the (111) surface anchored to the zigzag termination was considered. PtRu(111) was modeled with a $(2\mathrm{x}2\sqrt{3})$rect surface cell which corresponds to a 1.6% lattice mismatch between the metal and carbon cells. For the interface calculations, the lattice constant was set to the metal lattice constant; this, however, is a minor computational approximation as the interaction energy for the stable Pt-based system changes only by 0.07 eV/metal-carbon bond if the lattice constant is instead set to the optimized value of the graphene sheet lattice constant.

Computational Results for Anchoring Pt and PtRu Surfaces to Graphite

Figure 5 shows the optimized structures for the metal-carbon interface in the case of monometallic platinum. Figure 5(a) is the most thermodynamically stable structure with zigzag termination of carbon interfacing Pt(111). In this case, the carbon sheet is running along the (112) direction of the metal surface. The carbon atoms have alternating bridge and atop positions on the surface platinum atoms. The Pt-C bond distance is 2.19 Å and 1.99 Å for the bridge and atop position, respectively. A second possible direction for the graphene layer is the (110) direction; however, this configuration is higher in energy by 0.31 eV/metal-carbon bond. The (110) direction is instead preferred for the armchair edge, shown in Figure 5(b). In this case, the (112) is higher in energy by 0.06 eV/metal-carbon bond. The interface structures between zigzag and armchair terminated carbon edges with Pt(100) surface are shown in Figure 5(c) and Figure 5(d), respectively. In both cases the graphene sheets run along the (010) direction. The match between the surface and the edge is best for the zigzag terminated carbon, whereas the armchair terminated sheet is slightly distorted.

The interaction energy for structures (a)-(d) in Figure 5 are calculated to be -1.35, -1.02, -1.22 and $-1.09\,\mathrm{eV}\,\text{Å}^{-1}$, respectively. Thus, the zigzag termination interfacing Pt(111) is the most thermodynamically preferred system. This is in good

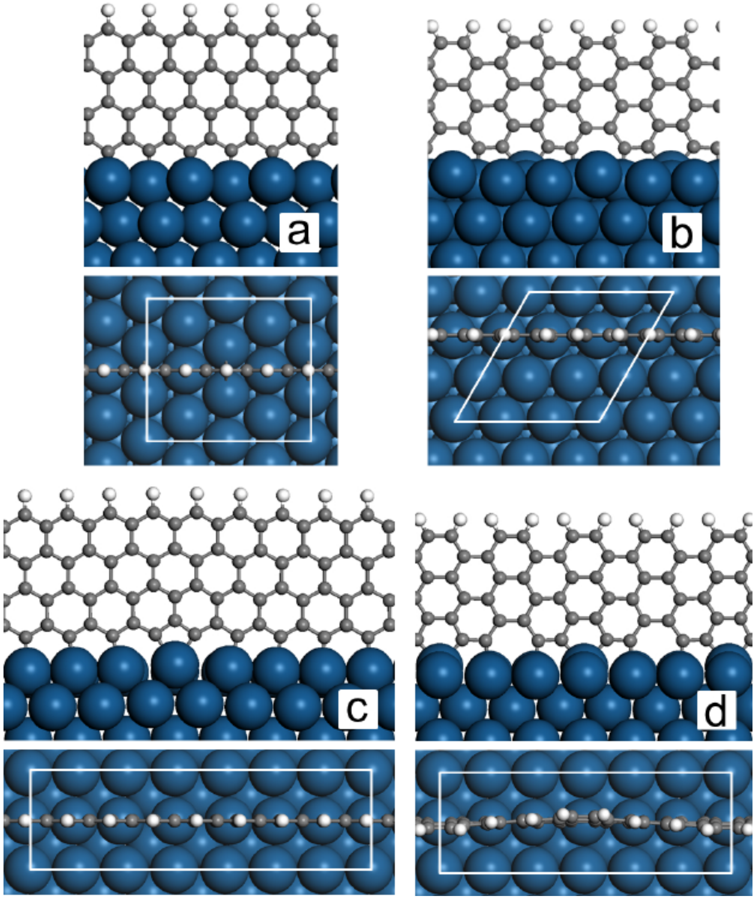

Figure 5: Optimum structures for the interface of monometallic Pt with C. (a) Pt(111) interfacing with zigzag terminated graphene sheet, (b) Pt(111) interfacing with armchair terminated graphene sheet, (c) Pt(100) interfacing with zigzag terminated graphene sheet, and (d) Pt(100) interfacing with armchair terminated graphene sheet.

agreement with the experimental TEM results which show that the (111) facet is anchored preferentially to the carbon nanofiber.[3] The bond strength of each metal-carbon bond is about $-3.3\,\mathrm{eV/bond}$ in this system. The preference for the (111) surface could be attributed to the very good match between the carbon and metal atoms. With this facet exposed to the interface surface, the carbon atoms can form alternating bridge and atop bonds with minor stress. The standard deviation of atop bonds is $5 \times 10^{-4}\,\text{Å}$, whereas it is $5 \times 10^{-5}\,\text{Å}$ for bridging bonds. These deviations favorably compare to the zigzag interface with Pt(100), which has only atop bonds and a standard deviation of metal-carbon bond length of $0.05\,\text{Å}$. Experimentally, graphene sheets are known to make an angle of 30° to the surface normal.[38] The potential energy surface of the interface angle between graphene and monometallic platinum is shallow and a local minimum is also found at about 29° from the surface normal with an interaction energy of $-1.39\,\mathrm{eV\,Å^{-1}}$ for zigzag termination of a graphene sheet with Pt(111).

For PtRu random alloy, the segregation properties of the bare (111) surface must first be investigated. As mentioned earlier, for bare surfaces the system with Pt segregated to the surface layer is preferred thermodynamically. This is reasonable given that the surface energy of Pt(111) is smaller than that of Ru(111). The values calculated in this study are $1.67\,\mathrm{J\,m^{-2}}$ and $2.76\,\mathrm{J\,m^{-2}}$ for Pt(111) and Ru(111), respectively. However, it should be noted that the core-shell structure is not preferred over the segregated PtRu alloy system. Instead the second layer is Ru and the rest of the slab maintains the $\mathrm{Pt_1Ru_1}$ stoichiometry, see Figure 2. This result agrees with experimental observations of the formation of $\mathrm{Pt_1Ru_1}$ alloy.[41]

Two relaxed configurations of the metal-graphene interface are reported in Figure 6. For this interface, the search was restricted to the PtRu(111) surface and the zigzag termination of graphene interfacing the metal along the (112)-direction. The preferred surface segregation changes when the metal is allowed to interface with the graphene sheet. Instead of the all-Pt surface, the stoichiometric composition is preferred. This can be understood by realizing that the interaction between Ru and C is stronger than the interaction between Pt and C. Interactions with the environment changing the surface composition is well known has been discussed in connection to oxidized PdAg surfaces.[42] The two configurations in Figure 6 have the carbon bonded in alternating atop and bridge positions. In (a), the atop position is over Ru, whereas in (b) it is over Pt. The two configurations are almost energetically degenerate, only being separated by 0.01 eV (total energy of the system). The interaction energy for the graphene-PtRu(111) interface is calculated to be $-1.30\,\mathrm{eV\,Å^{-1}}$ which is close to the value of the monometallic Pt surface, $-1.35\,\mathrm{eV\,Å^{-1}}$.

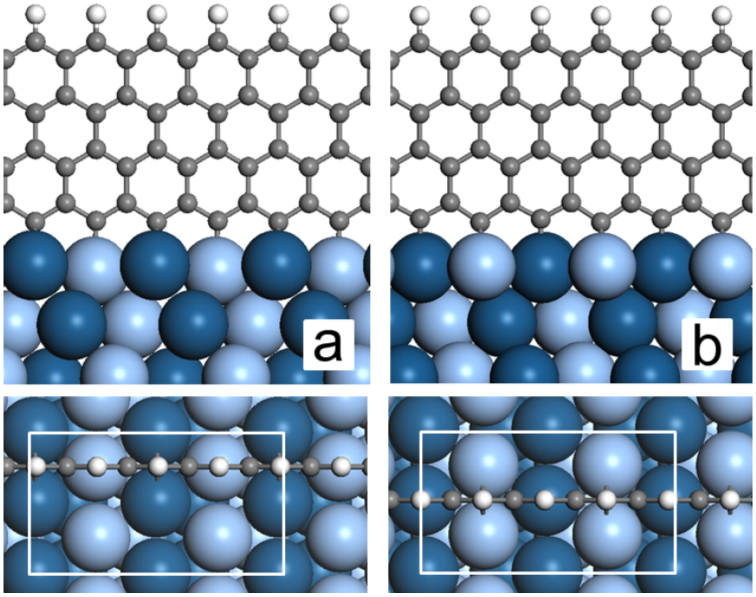

Figure 6: Side and top views of the relaxed zigzag graphene termination interfacing the PtRu(111) surface. (a) shows the configuration with carbon bridging Pt and atop Ru. (b) shows the configuration with carbon bridging Ru and atop Pt. The surface cells are indication by white lines. Atomic color codes: Pt (dark blue), Ru (light blue), C (grey), and H (white).

Characterization of the Metal-Carbon Interface

To study the nature of the metal-graphene interaction, a density of states (DOS) analysis was performed. The projected density of states (PDOS) is calculated by projecting the plane-wave eigenstates onto a linear combination of atomic orbitals (LCAO) eigenstates. Then the contribution from each eigenstate is broken down by angular momentum, giving the contributions from the s, p, d, and f orbitals, if available, in the conduction band. By comparing the valence orbitals from neighboring atoms, it is then possible to deduce which orbitals are involved in bonding and antibonding overlaps, as they will be of degenerate energy.

The PDOS from the graphene-PtRu(111) interface in the case with carbon anchored atop Ru is shown in Figure 7. The DOS is projected on Ru(4d), Pt(5d), and C(2p) for sites of C atop Ru (upper panel) and C bridging Pt (bottom panel). By comparing atoms at the interface to atoms in the bulk, the electrons involved in bond-

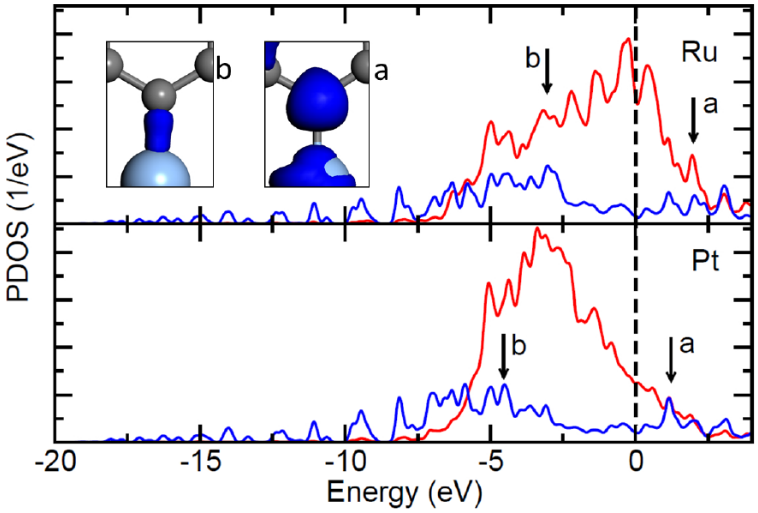

Figure 7: Projected density of states (PDOS) for the interface of a zigzag terminated graphene sheet with PtRu(111). The total density of states (DOS) is projected on Ru(4d), Pt(5d), and C(2p) on the sites of C atop Ru (upper panel) and C bridge Pt (lower panel). The energy is reported with respect to the Fermi energy and the intensity of the carbon contribution is doubled to increase the visibility. The insets show the densities of bonding, (b) located at $-3.22\,\mathrm{eV}$ below the Fermi energy, and antibonding, (a) located $2.52\,\mathrm{eV}$ above the Fermi energy, combinations of metal-carbon Kohn-Sham states. The reported states are indicated by arrows in the PDOS.

ing can be found. Then comparing these potential bonding sites between neighboring carbon and metal atoms, the actual bonding and antibonding overlaps can be found.

The valence electron configuration of Ru is $4d^7 5s^1$ whereas the valence configuration for Pt is $5d^9 6s^1$. This is visible in the PDOS as the d-band is wider and also that a larger part is above the Fermi energy for Ru as compared to Pt. Inspection of the C-states and, in particular, the regions with hybridization between the C(2p) and the metal states, reveals bonding and antibonding combinations. The bonding combinations are located at $-4\,\mathrm{eV}$ below the Fermi energy and the antibonding is only slightly above the Fermi energy at $2\,\mathrm{eV}$. These sets of states are indicated by arrows in Figure 7. The clear separation between bonding and antibonding states is indicative of covalent bonds. This is consistent with visualization of the representative Kohn-Sham orbitals. The orbital densities are shown as inserts in the case of C-Ru bonds. The bonding states have accumulation of charge between the carbon and metal atoms, whereas the antibonding states have nodes between atoms.

To further investigate bond type and polarity, a Bader charge analysis was performed.[43] Using the final ground-state charge density distribution, it is possible to find steepest ascent paths to charge density maxima. These maxima usually correspond to nuclei in the system, and all paths that lead to a maxima are assigned to that nucleus Bader region. By summing all the electron density in these regions, the total electronic charge of each Bader region can be calculated. By comparing atoms far from the graphene-metal interface with atoms at the graphene-metal interface, it is possible to analyze the charge transfer (which indicate strong electronic interactions like bonding). There is a charge transfer from Ru to Pt in the bulk of the PtRu alloy of about 0.25 electrons. At the metal-graphene interface, carbon is slightly negatively charged. The total charge on C atoms in the atop positions is 4.10 electrons, while the bridging C atoms have 4.30 electrons. These charge transfer values are consistent with the interpretation that the bridging and atop C atoms are sp^3 and sp^2 hybridized, respectively. The charge rearrangement in PtRu(111) is similar to Pt(111), where the total charge on C is 4.20 electrons in the bridging position and 4.00 electrons in the atop position.

On an atomic scale, it is generally difficult to experimentally characterize buried interfaces as the one studied here. One experimental technique that could be used is X-ray photoemission spectroscopy (XPS).[44] This technique has been used to reveal the thiol-gold interface which has been a long standing issue in surface science.[45,46] XPS is based on phenomenon that core electrons respond to the re-hybridization and charge transfer in the valence region and thereby shift their binding energies. These shifts are then signatures of the chemical environment of the element under investigation.

In order to facilitate interpretation of future experimental measurements of core-level binding energies, we have calculated the shifts for the metal-graphene interface as shown in Figure 6. The results for the surface core-level shifts (SCLS) are reported in Figure 8. The SCLS are calculated with respect to a bulk reference, represented by an atom in the center of the slab for the metal and in the center of the graphene sheet for the carbon. The calculated SCLS are −0.32 eV and −0.34 eV for Pt(111) and Ru(111) bare metal surfaces, respectively. This is in good agreement with experimental reports[47,48] and justifies this computation approach.

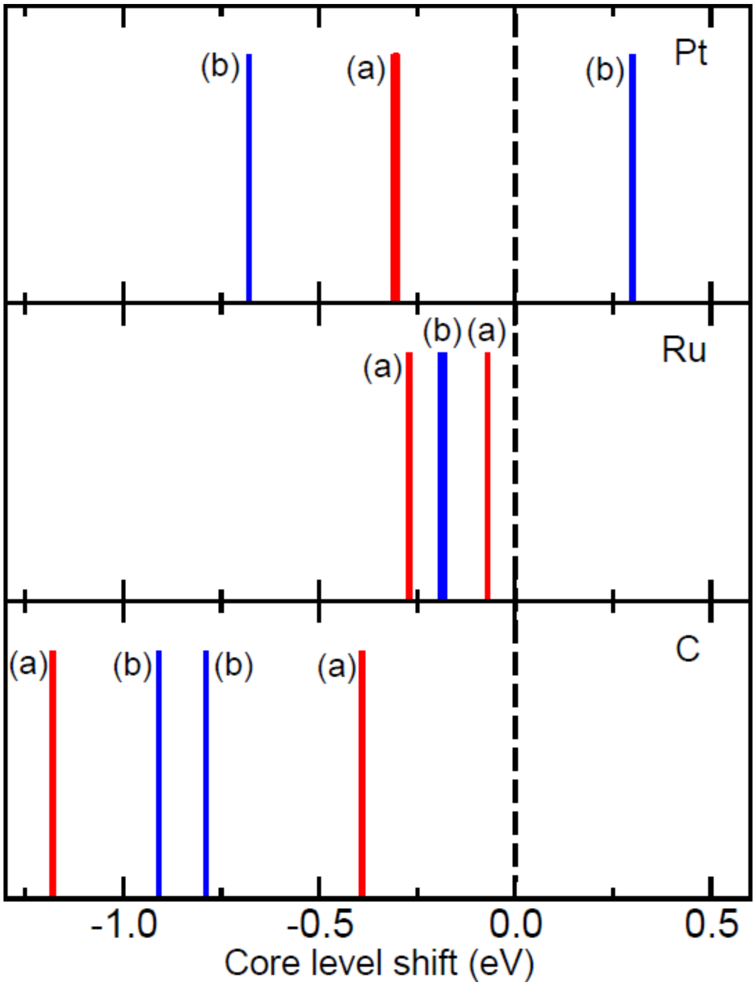

Figure 8: Surface core-level shifts (SCLS) for the (a) and (b) configurations in Figure 6. The shifts are calculated for C, Ru, and Pt. The corresponding references are C in the center of the graphene sheet, Ru in the bulk of the alloy slab, and Pt in the bulk of the alloy slab. See text for discussion.

The calculations show substantial shifts for all three elements. Considering first Pt, a clear difference is predicted for the cases when C is anchored atop or in bridge. In the case of atop, two shifts are observed separated by 1 eV. The positive shift

(0.3 eV) is predicted for the atom bonded to carbon. If the sheet is instead bonded via carbon in a bridge position between Pt, only one peak is observed at −0.3 eV. A similar trend is calculated for Ru; however, the shifts are not as pronounced as for Pt. The shifts for carbon clearly distinguish between the two configurations as well. The largest separation (0.8 eV) between atop and bridging bonded C is calculated for the case when C is adsorbed atop Ru. This is consistent with the interaction between carbon and Ru being much stronger than between carbon and Pt.

Conclusions

Using DFT calculations, the interface between graphene sheets and different crystal facets of monometallic Pt and PtRu alloy have been investigated. The systems model PtRu particles supported on cup-stacked carbon nanofibers used in PEMFCs. The calculations show that the (111) facet of the metals preferentially anchor to the graphene sheet. This result, which is in good agreement with experimental observations[3], is rationalized by good structural match between the metal and carbon lattice constants. The metal-carbon bond is reasonably strong (about 3 eV) and of covalent character. Although the electron conductivity through the interface was not calculated, the calculated strong covalent bonds are consistent with favorable conductive properties that have been measured for the PtRu on cup-stacked carbon nanofiber support[3]. While the bare PtRu alloy surface is rich in Pt, the interaction with carbon stabilizes a surface that preserves the alloy composition. Core-level binding energies of carbon, platinum, and ruthenium are found to provide valuable signatures of the interface and provide a means to interpret future high resolution XPS SCLS experiments.

CHAPTER III

INFLUENCE OF EXTERNAL MAGNETIC FIELD ON CONFINED-PLUME CHEMICAL DEPOSITION OF IRON OXIDE NANOPARTICLES USING FEMTOSECOND NIR LASER IRRADIATION: CHAIN-LIKE NANOPARTICLE ALIGNMENT IN A FLUID MEDIUM

Introduction to Confined-Plume Chemical Deposition

Confined-Plume Chemical Deposition (CPCD) is a new synthesis technique developed in the Lukehart lab. CPCD is a single-step process for preparing asperitic coatings of microscale, crystalline, hard/superhard ceramic asperities on either hard or polymer supports. In CPCD, irradiation of molecular precursor-on-support specimens, spatially confined between transparent solid plates, by a train of picosecond pulses lasting a few micro-seconds of pulsed infrared (IR) Free-Electron Laser (FEL) light tuned to a precursor vibrational band leads to rapid precursor decomposition and deposition of microcrystalline material of high purity in a single-step process. A visible reaction plume forms at the laser/precursor interface, under conditions of spatial and temporal confinement, as pulsed laser light is scanned across physically confined precursor/support specimens. Pulse energy transmission analysis reveals that 75-95% of pulsed FEL IR light energy is absorbed by precursor decomposition. Reaction plume formation and the low duty cycle of pulsed lasers minimize collateral thermal damage to support materials, thereby permitting use of either hard or soft supports for CPCD. Rapid cooling of reaction plume species leads to surface-nucleated, nearly vertical growth of crystalline, ceramic microcrystals without need of subsequent thermal annealing. Using appropriate precursors, silicon wafer or polymer films as supports, and silicon wafer and NaCl plates for physical confinement, microcrystalline asperitic coatings of the known superhard ceramic material ReB_2, ultra-incompressible RuB_2, very hard B_4C, or superhard WB_4 ceramics have been produced by FEL-initiated CPCD.[16]

Now CPCD initiated by pulsed table-top laser light, specifically light produced by an amplified Ti:sapphire laser (795 nm, 100 fs, 1 kHz), a Q-switched Nd:YLF laser

(527 nm, 150 ns, 1 kHz), or an Er:YAG laser (2.94 µm, 150 µs, 20 Hz) is investigated. Given the wide availability of table-top lasers compared to highly restricted access to IR FEL light, CPCD now becomes a generally applicable single-step deposition method for producing asperitic microcrystalline coatings on a wide variety of hard, soft, or bio-tissue supports. While CPCD initiated by pulsed IR FEL light tuned to an IR absorption wavelength of precursor molecules occurs with essentially complete success, identifying suitable precursors for CPCD initiated by the three table-top lasers investigated proved far more challenging. These precursors must be designed to absorb the energy of a laser, but that is no guarantee of plume formation. Some precursors known to absorb at table-top laser wavelengths do not initiate CPCD reaction plume formation, a necessary condition for materials deposition. Although mechanisms of table-top laser light absorption during CPCD remain uninvestigated, reasonable trial-and-error choice of molecular precursors usually leads to successful plume formation and materials deposition. Any inconvenience associated with identifying suitable precursors is greatly compensated by the wide availability of visible and IR table-top lasers.

Greatest success is achieved using 795-nm femtosecond table-top laser light, most likely due to very high power density (ca. $1.6 \times 10^{12}\,\mathrm{W\,cm^{-2}}$) during laser pulses compared to the 2.94-µm laser (ca. $2.5 \times 10^{5}\,\mathrm{W\,cm^{-2}}$) and the 527-nm laser (ca. $2 \times 10^{7}\,\mathrm{W\,cm^{-2}}$). However, there are cases where having control over the laser power or having less power density can be advantageous. To a small extent laser power density can be controlled by the focal spot size, but currently the best method to modulate power is switching from one laser source to another. However, laser power density is not the only consideration; the frequency of molecular transitions in the precursor molecule needs to match the frequency of the laser. For the 795-nm laser, molecules need to have electronic transitions, usually found in conjugated molecules. Electronic transitions are most commonly associated with colored molecules, and with such a high power density any absorption around 795 nm is enough to initiate plume formation. For the 527-nm laser, precursor molecules need to have an electronic transition as well; however due to lower power density the color must be more closely matched to absorb green light. Molecules that absorb green light appear red. For the 2.94-µm laser, precursor molecules need to have vibrational transitions centered around $3400\,\mathrm{cm}^{-1}$. $3400\,\mathrm{cm}^{-1}$ corresponds to vibrational transitions present in alcohols and primary amines.

Introduction to Confined-Plume Chemical Deposition of Magnetic Iron Particles

External magnetic field influences on thin-film or nano/micro-particle materials deposition processing has been used to produce (1) harder and more wear-resistant diamond-like carbon coatings formed by plasma torch, filtered cathodic vacuum arc, or magnetically enhanced plasma deposition methods[49–51], (2) more uniform target etching rates and spatially focused materials deposition on the square-centimeter scale in magnetron sputtering discharges[52,53], (3) smoother films of AlNiCo5 produced by pulsed laser deposition[54], and (4) modification of CdS film thickness, surface morphology, and grain size when formed by aqueous precipitation[55].

External magnetic field influences on magnetic nano-particle deposition performed in fluid media is evidenced by formation of field-aligned, chain-like particle aggregation morphologies. Field-induced deposition of 15-nm diameter Co nanoparticles formed via electroless solution reduction gives chain-like aggregation of Co metal as nanowires of (190 nm average width x ca. 160 µm length[56]. These nanowire structures align in chain-like fashion parallel to external magnetic field lines. Magnetic field-assisted hydothermal synthesis of 80-nm magnetite (Fe_3O_4) nanoparticles under magnetic field influence affords ca. 1 µm long chain-like aggregates that align parallel to magnetic field lines[57].

Magnetic-field-induced alignment of preformed Fe_3O_4/polystyrene Janus microparticles in liquid dispersions provides similar chain-like structures.[58] While applied external magnetic fields influence the macroscale morphology and properties of thin films formed using physical vapor deposition methods, chemical deposition of magnetic materials formed as nano- or microparticle dispersions in liquid phases tends to give field-aligned, chain-like deposition morphologies.[59,60]

A key feature of CPCD processing is that while materials deposition occurs under open-air, ambient laboratory conditions, pulsed-laser decomposition of chemical precursors produces a reaction plume within the tri-layer specimen under spatial and temporal confinement. Scanning the pulsed laser beam across the sample specimen generates reaction-plume pulses that undergo rapid cooling, which initiates nucleated growth of high-melting product microcrystals on solid support surfaces.

An interesting question arises as to how application of an external magnetic field might affect CPCD deposition of a magnetic product phase, particularly when a liquid precursor is used. Given that the kinetics and mechanism of CPCD materials deposition are unknown, it is difficult to predict if a magnetic field effect would be similar to those observed by physical vapor deposition of thin-films or to chain-like particle aggregation observed by chemical deposition from magnetic nano- or microparticle/fluid dispersions (vide ut supra).

Knowing that chemical vapor decomposition or thermal cracking of $Fe(CO)_5$ affords Fe nanoparticles that air-oxidize to Fe_3O_4,[61,62] CPCD processing using liquid $Fe(CO)_5$ as precursor was performed in both the presence and absence of an oriented external magnetic field. In the absence of an external magnetic field, CPCD processing of liquid $Fe(CO)_5$ affords a random deposition of Fe_3O_4 particles. However, in the presence of an applied external magnetic field, CPCD processing of liquid $Fe(CO)_5$ produces chain-like deposition of Fe_3O_4 particles with long-axis alignment parallel to applied field direction. This outcome is consistent with formation of Fe or Fe_3O_4

particle dispersions within the neat liquid $Fe(CO)_5$ precursor medium during CPCD processing.

Experimental

Reagents and General Methodologies $Fe(CO)_5$ was purchased from Strem Chemicals, Inc. and used as received. 1.5 in x 1.5 in x 0.75 in N52 neodymium-iron-boride rectangular block magnet was purchased from K&J Magnetics, Inc. Note: These are very strong permanent magnets (0.5 Tesla), and great care must be taken when handling them around ferromagnetic metal. A 0.5 in ultrahigh molecular weight polyethylene (UHMWPE) dowel was purchased from McMaster-Carr. This dowel was cut into 3 mm disks using a thin dremel blade. 12.5 mm x 3 mm circular sapphire windows were purchased from ThorLabs, Inc. A commercial FTIR pellet holder (13 mm diameter) was used as the sample holder for CPCD experiments.

Powder X-ray diffraction scans were obtained on a Scintag X1 θ/θ automated powder X-ray diffractometer with a Cu target, a Peltier-cooled solid-state detector, and a zero-background Si(510) sample support with UHMWPE spacers. SEM images were obtained on a Hitachi S-2400 electron microscope with an accelerating voltage of 10 kV to 20 kV. This SEM is equipped with a thin-window energy dispersive x-ray spectrometer (EDS) for microanalytical specimen characterization.

Confined-Plume Chemical Deposition Processing Femtosecond UV pulses are produced in an amplified titanium-sapphire (Ti:sapphire)-based laser system operating at a fundamental wavelength of 795 nm. A continuous wave (cw) pumped mode-locked Ti:sapphire oscillator, producing <100 fs pulse widths at a repetition rate of 82 MHz, is used to seed the Ti:sapphire amplifier which increases the energy of the femtosecond pulses to ca. 1 mJ/pulse in a regenerative and linear double-pass amplifier arrangement while maintaining pulse widths of ca. 150 fs. This gives a peak power of 6.6 GW, which is focused through cylindrical optics into a line of approximately 40 µm by 6 mm, giving a peak intensity of 2.7 TW cm^{-2}. This is enough energy to decompose almost any precursor with absorption in the visible spectrum.

UHMWPE disks were coated with 5 µL of $Fe(CO)_5$ liquid and sandwiched on top by sapphire windows in a commercial FTIR pellet holder. This system was then irradiated from the top through the sapphire window using a stepping motor scanning stage to raster (at 25 µm/s) the sample through the line-focused 795-nm laser beam. The laser beam was focused into a line that was approximately 40 µm x 6 mm with the beam perpendicular to the direction of scanning. Laser experiments were conducted in the open, ambient atmosphere and stored in the same. The sandwich assembly was separated, and the coated UHMWPE was characterized by SEM, EDX, and XRD. Control experiments confirmed that changing the orientation of the laser light polarization did not affect the pattern of magnetic particle deposition.

Magnetic field influence on particle formation and deposition was investigated by placing a neodymium-iron-boride magnet under the sample (approximately 2 cm away, due to stage constraints) under different relative orientations. Iron particles were deposited (a) with no magnet field influence, then the magnet was placed such that the north-south field lines were (b) perpendicular to the sample (so-called up), (c) parallel to the specimen plane but perpendicular to the direction of scanning, and (d) parallel to the specimen plane and parallel to the direction of scanning (see Figure 9). All experiments were conducted in a single day from a single batch of $Fe(CO)_5$ with the same magnet being oriented in different directions relative to the sample.

Results and Discussion

Preliminary experiments confirmed that CPCD initiates reaction plume formation when line-focused, pulsed 795-nm femtosecond laser light is scanned across a tri-layer sample specimen consisting of a liquid $Fe(CO)_5$ precursor layer confined between a 3 mm thick sapphire top disc and a 3 mm thick ultra-high-molecular-weight polyethy-

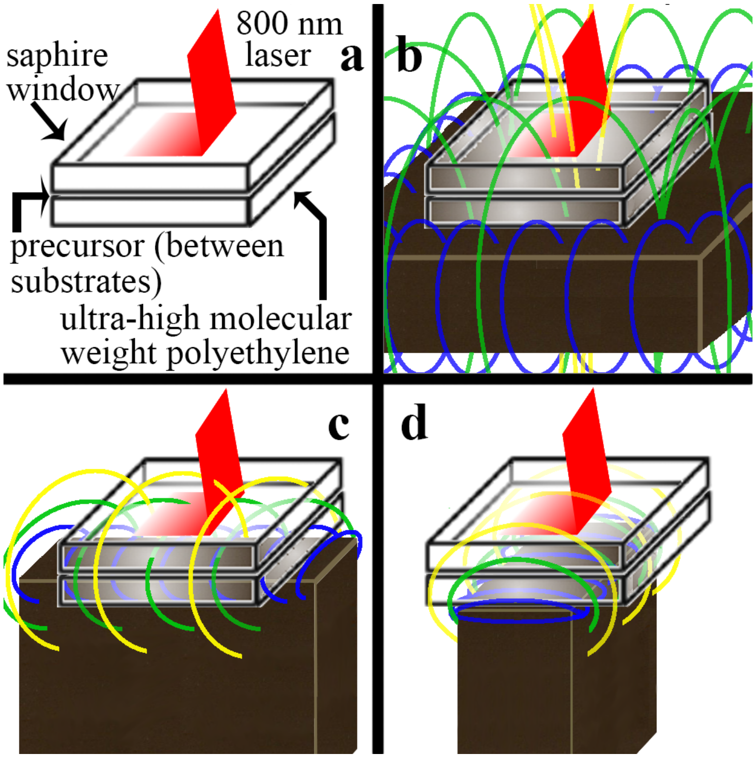

Figure 9: Cartoon descriptions of performed CPCD experiments. (a) CPCD tri-layer specimen composition showing laser line focus scanning from left to right with no applied magnetic field. (b) CPCD performed with applied magnetic field north-south axis normal to specimen plane. (c) CPCD performed with applied magnetic field north-south axis parallel to specimen plane and field lines perpendicular to scanning direction. (d) CPCD performed with applied magnetic field north-south axis parallel to specimen plane and field lines parallel to scanning direction.

lene (UHMWPE) film bottom disc, see Figure 9 (a). A visible reaction plume travels with the laser line focus producing concomitant formation of a thin, black surface deposit. Powder XRD (Figure 10) reveals weak diffraction peaks consistent with the presence of Fe_3O_4 as the only crystalline phase deposited onto the highly ordered UHMWPE specimen support. Thermal decomposition of $Fe(CO)_5$ is known to occur through formation of Fe particles that oxidize in air to give Fe_3O_4.[61,62]

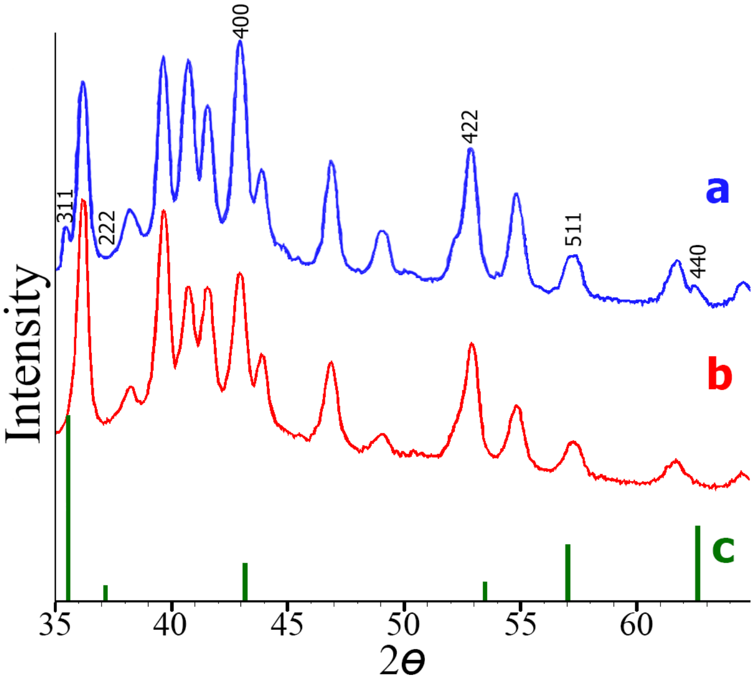

Figure 10: Powder x-ray diffraction patterns of (a) thin-film black deposit on UHMWPE support and (b) UHMWPE support. Line pattern of pure Fe_3O_4 (PDF#19-0629) is shown in (c).

SEM micrographs of the blackened surface reveal a moderately dense coating of nearly spherical particles having diameters ranging from ca. 100 nm to 500 nm, see Figure 11 (a). EDX elemental mapping of particle aggregates reveals uniform distribution of Fe and oxygen atoms throughout the entire aggregate, consistent with an iron oxide composition (see Figure 12).

To determine external magnetic field effects on particle deposition, the above CPCD synthesis was repeated on top of a neodymium permanent block magnet

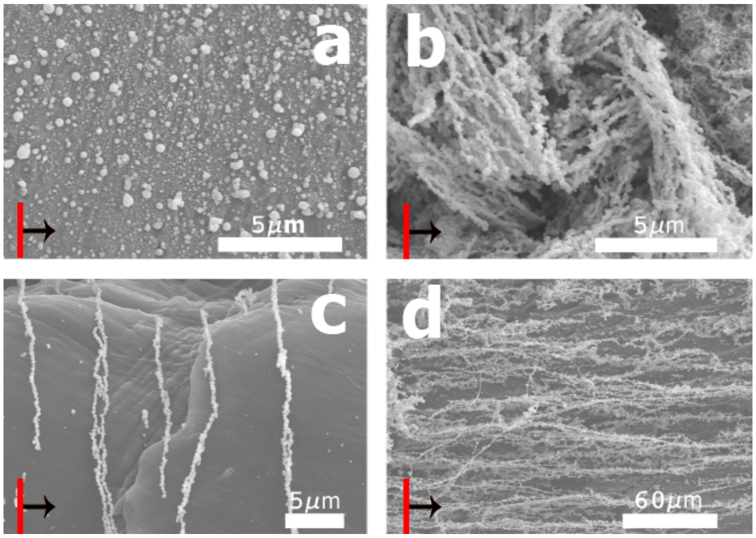

Figure 11: SEM micrographs. (a) CPCD performed with no applied magnetic field. (b) CPCD performed with applied magnetic field north-south axis normal to specimen plane. (c) CPCD performed with applied magnetic field north-south axis parallel to specimen plane and field lines perpendicular to scanning direction. (d) CPCD performed with applied magnetic field north-south axis parallel to specimen plane and field lines parallel to scanning direction. The red line inset indicates the line-focused laser beam and the black arrow indicates direction of scanning, which were held constant through all four experiments.

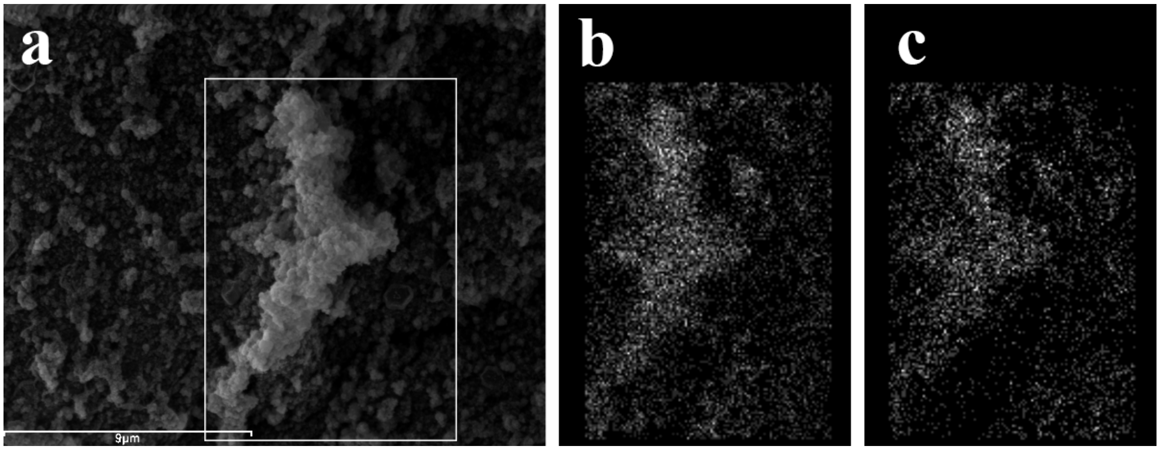

Figure 12: EDX elemental mapping of a Fe_3O_4 particle aggregate formed by CPCD on UHMWPE showing (a) SEM image of a reference aggregate. (b) Image showing overlapping Fe $K_\alpha 1$ emission. (c) Image showing overlapping O $K_\alpha 1$ emission.

(0.5 Tesla) in which the north-south magnetic field lines were oriented end-on (or normal) to the plane of the sample specimen, Figure 9 (b), parallel to the specimen plane but perpendicular to the light beam scanning direction, Figure 9 (c), or parallel to the specimen plane and parallel to the light beam scanning direction, Figure 9 (d). Both the light beam scanning direction and line focus direction were kept constant as indicated in Figure 9. Appreciable magnetic field effects are observed, as revealed in SEM images Figure 11 (b-d). Toroidal-like magnetic field lines passing normal to the specimen plane, Figure 9 (b), give a twisted chain-like aggregation of deposited particles, Figure 11 (b). However, magnet orientations having field lines passing parallel to the specimen plane but either perpendicular, Figure 9 (c), or parallel, Figure 9 (d), to the scanning direction give chain-like particle aggregation oriented parallel to the applied magnetic field lines, Figure 11 (c) and Figure 11 (d), respectively. SEM images of the latter two samples at higher magnification, Figure 13, reveal highly ordered chain-like particle aggregation.

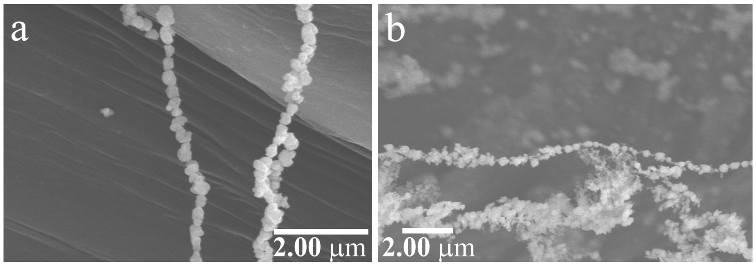

Figure 13: SEM micrographs at higher magnification showing chain-like particle alignment. (a) CPCD performed with applied magnetic field north-south axis parallel to specimen plane and field lines perpendicular to scanning direction. (b) CPCD performed with applied magnetic field north-south axis parallel to specimen plane and field lines parallel to scanning direction.

Dependence of deposition product on scan-rate was noticed. As seen in Figure 14, if the scan rate is too fast particles are formed too far from one another to aggregate adequately during deposition; however it would seem as long as the scan-rate is slow enough to allow aggregation, chain-like aggregates will form. For these experiments 25 μm/s was found to be slow enough to form chain-like aggregates of magnetic nanoparticles.

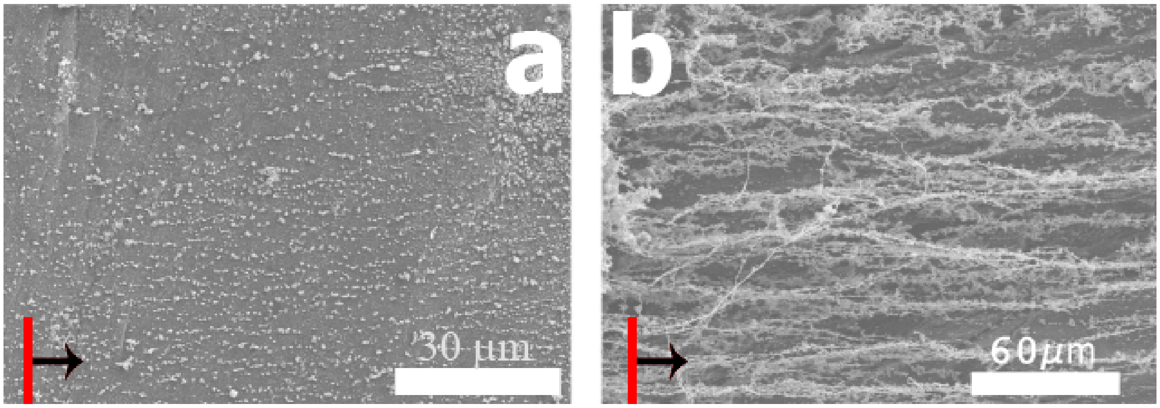

Figure 14: SEM micrographs. (a) CPCD performed at a scan-rate of 100 µm/s with applied magnetic field north-south axis parallel to the specimen plane and field lines parallel to scanning direction. (b) CPCD performed at a scan-rate of 25 µm/s with applied magnetic field north-south axis parallel to the specimen plane and field lines parallel to scanning direction. The red line inset indicates the line-focused laser beam and the black arrow indicates direction of scanning, which were constant through both experiments.

With a scan-rate of 25 µm/s, the entire 240 µm area seen in Figure 11 (d) can be formed and deposited in ca. 10 seconds. Compared to hydrothermal synthesis[57] and electroless solution reduction[56] techniques, which take about an hour for synthesis of 1 µm to 190 µm chains, respectively, and then use of an post-reduction deposition step, CPCD offers a much quicker and easier synthesis methodology. CPCD can be used to form ca. 250 µm long × 0.2 µm wide chain-like aggregates at the site needed in ca. 10 seconds.

Such chain-like aggregation of magnetic particles under the influence of an applied external magnetic field is strongly indicative of magnetic particle deposition from a liquid-phase dispersion.[56,58] Under the spatial and temporal confinement conditions of CPCD, light-initiated decomposition of $Fe(CO)_5$ molecules apparently produces local concentrations of liquid-stabilized Fe atoms that rapidly condense as chains of Fe/Fe_3O_4 nanoparticles. With the permanent magnet used in this initial study, nanoparticle interchain distance is ca. 5 µm, independent of in-plane perpendicular or parallel magnetic field alignment, see Figure 9 (c) and Figure 9 (d) respectively.

This separation probably indicates the distance over which a nanoparticle chain can attract another magnetic particle before new chain growth occurs.

Conclusions

Confined-Plume Chemical Deposition of Fe particles using neat liquid $Fe(CO)_5$ as precursor and under ambient atmosphere gives a highly dispersed pattern of nearly spherical Fe_3O_4 nanoparticles (average diameter of ca. 200 nm). Repeating this deposition under the influence of an external magnetic field (0.5 T), with field lines oriented within the specimen plane but parallel or perpendicular to the scanning direction, give chain-like particle aggregation oriented parallel to the applied magnetic field lines. Magnetic nanoparticle chains have single-particle width and average length of ca. 200 µm.

Production of magnetic particles within liquid media via CPCD under the influence of an applied magnetic field represents a new, one-step method for preparing chain-like magnetic nanowire morphologies. Although the scope of this method and experimental control of magnetic nanoparticle size and inter-chain distance need to be determined/optimized, this method allows much more rapid particle chain deposition than is possible via either solution electroless reduction or hydrothermal reduction (ca. 10 min for CPCD compared to ca. 1 h for the others). In addition, chain-like magnetic particle deposition using CPCD occurs with spatial precision of laser beam width directly on a substrate of choice. In contrast, electroless or hydrothermal reduction methods usually lack spatial precision and entail a solution-phase synthesis followed by a post-synthesis deposition step. Direct deposition using CPCD would also permit formation of magnetic nanoparticle chain-like networks, such as those used in MEMS and microdevice technologies, by real-time alteration of applied magnetic field direction during synthesis. Realizing such possibilities will require further optimization of CPCD methods.

CHAPTER IV

CONFINED-PLUME CHEMICAL DEPOSITION OF GOLD PARTICLES ON ONION (*ALLIUM CEPA*) TISSUE: PARTICLE LOCALIZATION SIMILAR TO HYDROTHERMAL POLYOL DEPOSITION

Introduction to Metal on Biological Supports

Deposition of inorganic materials on biotissues is of interest to show the breadth of application for CPCD synthesis techniques. Green-onion tissue was chosen as the biological support for this study because of its wide availability and easily viewable cellular structure. Noble metal deposition on onion tissue is known, and gold was chosen for its ease of reduction and deposition. Evaporation or sputtering of gold[63] or platinum[64] onto cellulosic material, such as onion tissue, at mild temperatures gives thin-layer metal deposition up to 10 nm thick suitable for scanning electron microscopy imaging. Likewise, sputtering gold/palladium alloy onto cellulose nanopaper gives thin-film deposition of noble metal alloy.[65] However, gold metal deposition on cellulose nanocrystals by hydrothermal chemical reduction of Au ions occurs with Au nanoparticle formation rather than thin-film deposition.[66] In aqueous solution at 120 °C, Au(III) ions undergo polyol reduction by nanocellulose surface OH groups and deposit as gold nanoparticles 20 nm to 40 nm in diameter. Polyol reduction of aqueous Au(III) ions using only α-D-glucose, sucrose, or maltose as reducing agents and rapid heating by microwave irradiation also forms Au nanoparticles.[67]

Confined-Plume Chemical Deposition (CPCD) is an excellent method for preparing crystalline coatings of ceramic microparticles on either inorganic or polymer supports.[16] In CPCD, laser light initiates precursor decomposition generating a visible reaction plume at the precursor/laser beam interface. Under optimized conditions, deposition of crystalline ceramic particles occurs without noticeable collateral thermal damage to hard or soft support materials.

A key feature of CPCD processing is that while materials deposition is performed under open-air, ambient laboratory conditions, pulsed-laser decomposition of chemical precursors produces a reaction plume within the multicomponent specimen system under spatial and temporal confinement. Scanning a laser beam across the sample specimen generates a spatially confined reaction plume (of elevated temperature and pressure but short lifetime) that travels across the specimen. Upon rapid cooling, high-melting product phases condense from the reaction plume and deposit on the surfaces of the solid support materials. Compositional control of the deposited material is achieved by proper choice of precursor.[16]

At present, the temperature, pressure, reaction kinetics, time evolution, and chemical speciation of CPCD-generated reaction plumes remain unknown. However, achieving successful coating depositions by CPCD on thermally sensitive polymer supports raises the intriguing possibility that CPCD could be used to fabricate hard coatings on biological supports, such as gold deposition on onion tissue. Likely outcomes of CPCD plume generation on such a highly cellulosic support include complete decomposition of onion tissue support, gold deposition on partially degraded onion tissue, or thin-film deposition of gold with little or no collateral thermal damage to onion tissue support.

To test for these outcomes, CPCD processing of onion tissue specimens was attempted using $(Et_3P)AuBr$ as precursor layer. Au(I) phosphine complexes readily reduce to Au(0) via direct thermolysis[68,69] or chemical reduction[70,71]. CPCD deposition of gold metal on green-onion (*Allium cepa Baja Verde*) tissue is now reported to occur with partial degradation of onion cell tissue and Au nanoparticle deposition on cell wall features. Au nanoparticles deposit as cubiod agglomerates with significant preference on inter-cellular double-wall surfaces. This deposition morphology is consistent with exposure of cellulose microfibrils within cell walls[72] and subsequent hydrothermal polyol reduction of Au ions present within the CPCD reaction plume by surface cellulose OH groups to form Au nanoparticles. Neither a complete degradation of onion tissue nor thin-film deposition of Au metal is observed. Confined-Plume Chemical Deposition initiated using pulsed laser radiation from a tabletop laser is reported.

Experimental

Reagents and General Methodologies *Allium cepa* (green onion) was purchased from a local grocer. 0.5 in x 1 mm circular glass supports were cut at Vanderbilt in the glass shop from microscope glass slides. 12.5 mm x 3 mm circular sapphire windows were purchased from ThorLabs, Inc. A commercial FTIR pellet holder (13 mm diameter) was used as the sample holder for CPCD experiments.

Powder X-ray diffraction scans were obtained on a Scintag X1 θ/θ automated powder X-ray diffractometer with a Cu target, a Peltier-cooled solid-state detector, and a zero-background Si(510) sample support and UHMWPE spacers. SEM images were obtained on a Hitachi S-2400 electron microscope with an accelerating voltage of 10 kV to 20 kV.

Confined Plume Chemical Deposition Processing Femtosecond UV pulses are produced in an amplified titanium-sapphire (Ti:sapphire)-based laser system operating at a fundamental wavelength of 795 nm. A continuous wave (cw) pumped mode-locked Ti:sapphire oscillator, producing 100 fs pulse widths at a repetition rate of 82 MHz, is used to seed the Ti:sapphire amplifier which increases the energy of the femtosecond pulses to ca. 1 mJ/pulse in a regenerative and linear double-pass amplifier arrangement while maintaining pulse widths of ca. 150 fs. This gives a peak power of 6.6 GW, which is focused through cylindrical optics into a line of approximately 40 µm by 6 mm, giving an intensity per pulse of 2.7 TW cm^{-2}. This is enough energy to decompose almost any precursor showing absorption in the visible spectrum.

A circular piece of green onion skin (0.5 in diameter x ca. 1 mm thickness) supported on a circular glass wafer (0.5 in diameter x 1 mm thickness) was coated with ca. 60 µL of 100 mM solution of bromo(triethylphosphine)gold in chloroform. Following solvent evaporation, a circular sapphire wafer (0.5 in diameter x 3 mm thickness) was placed on top of the coated onion, and the entire assembly was secured onto a scanning stage. Pulsed irradiation produced by a 800 nm femtosecond Ti:Sapphire IR laser, operating at 1 kHz and at ca. 1 mJ pulse energy, was passed through a cylindrical lens and focused near to the onion layer. The specimen assembly was rastered at a scan rate of ca. 300 µm/s. During laser irradiation, a reaction plume is observed along with formation of an apparent black/purple coating of product metal. Powder x-ray diffraction (XRD) confirms formation of Au metal, and scanning electron microscope (SEM) images reveal good particle coverage and uniformity and an average metal alloy particle size of ca. 3 µm.

Results and Discussion

Preliminary experiments confirmed that under CPCD conditions, as a line-focused, pulsed 795-nm femtosecond laser light is scanned across a quad-layer sample specimen, a reaction plume is initiated. The quad-layer sample specimen consists of a bromo(triethylphosphine)gold layer on onion tissue confined between a 3-mm thick sapphire top disc and a 1-mm thick glass bottom disc, see Figure 15. A visible reaction plume travels with the laser line focus producing concomitant formation of a black/purple surface deposit, but no visible change to the onion tissue. Powder XRD reveals weak diffraction peaks consistent with the presence of Au as the only crystalline phase deposited onto the onion, see Figure 16. Onion cells have some ordering present to give two large background peaks centered at about 23° and 38° 2θ.

SEM of the gold deposited on onion shows the cell structure of the onion is intact. The edges of the cell show slight damage and definite gold deposition, see Figure 17. These SEM images indicate that enough energy per pulse is available to decompose the gold precursor and deposit gold particles on the edge of onion cells. The low magnification SEM images (Figure 17 (a)) show almost nothing is deposited on the cells. High magnification SEM images (Figure 17 (c)) show cuboid particles clustered on the cell walls, consistent with the cubic unit cell of gold particles.

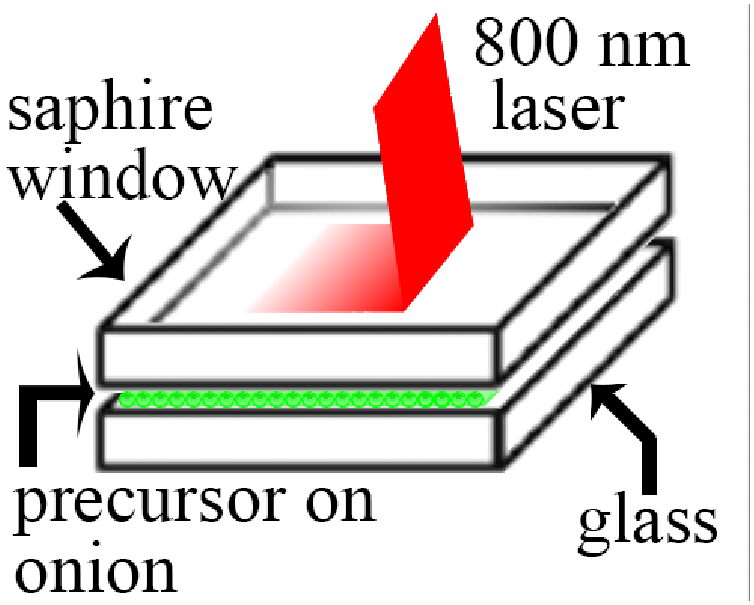

Figure 15: Cartoon descriptions of performed CPCD experiments showing a CPCD tri-layer specimen composition with laser line focus scanning from left to right.

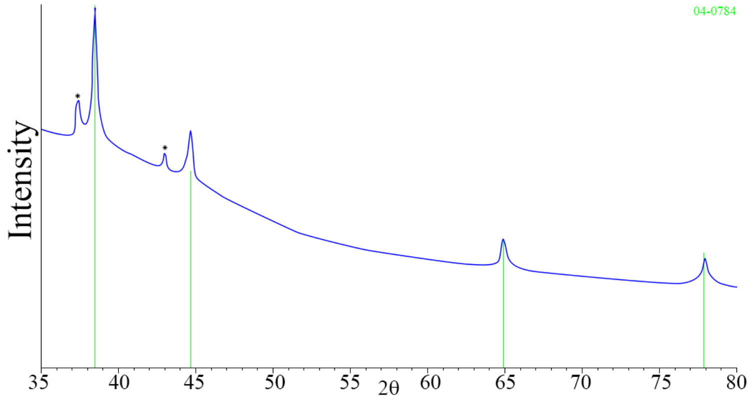

Figure 16: Powder x-ray diffraction(Cu K_α radiation) pattern of the Au/onion tissue/glass along with the line pattern of pure Au metal (PDF# 4-0784). The stars indicate background impurities present in the onion.

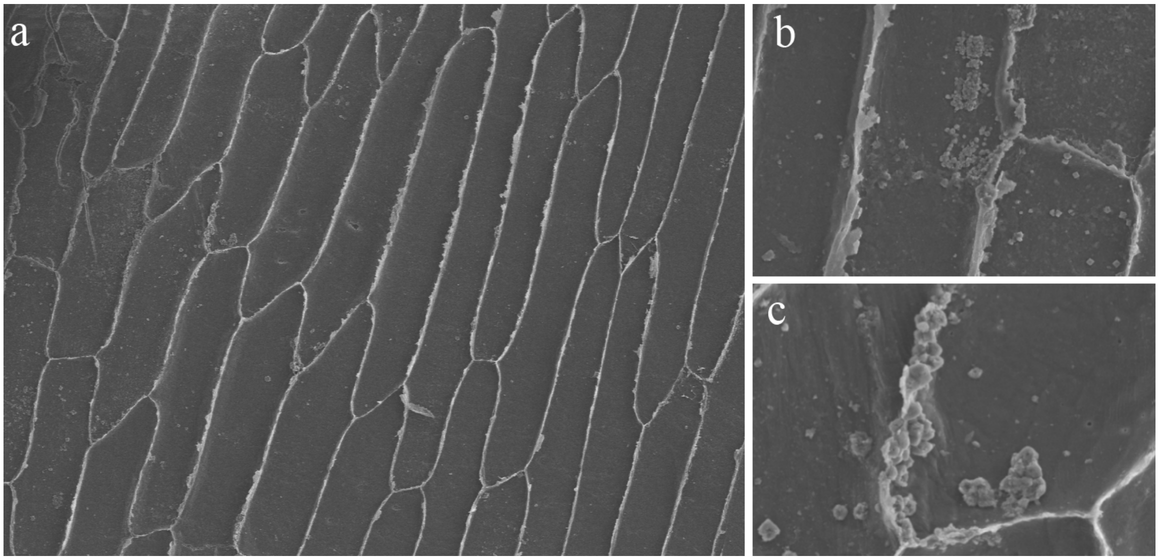

Figure 17: SEM micrographs of Au/onion tissue specimen following CPCD of gold metal at three magnifications. (a) Image showing multiple onion cells with Au deposition predominately at inter-cell double walls and some intra-cell locations. (b) Image at higher magification. (c) Image at highest magnification showing the nanoparticulate structure of deposited gold.

To confirm that a reduction similar to polyol was responsible for reducing gold, several other base and noble metals were investigated. Using acetylacetonate salts of zinc, copper, palladium, platinum, and silver, it is seen that the reduction conditions are not strong enough to reduce zinc or copper, and are just barely strong enough to give very minor metal peaks for palladium and platinum, but can easily reduce silver (see Figure 18). These precursors were decomposed under the same CPCD conditions as $(Et_3P)AuBr$, namely using the 795-nm laser with a cylindrical focus rastered at a scan rate of 300 µm/s.This metal precursor reduction trend is consistent with what is known of polyol reductions, and is further confirmation of the reaction pathway. Figure 18 (f) shows the background peaks for laser irradiated onion, which gives rise to broad peaks at about 23° and 38° 2θ.

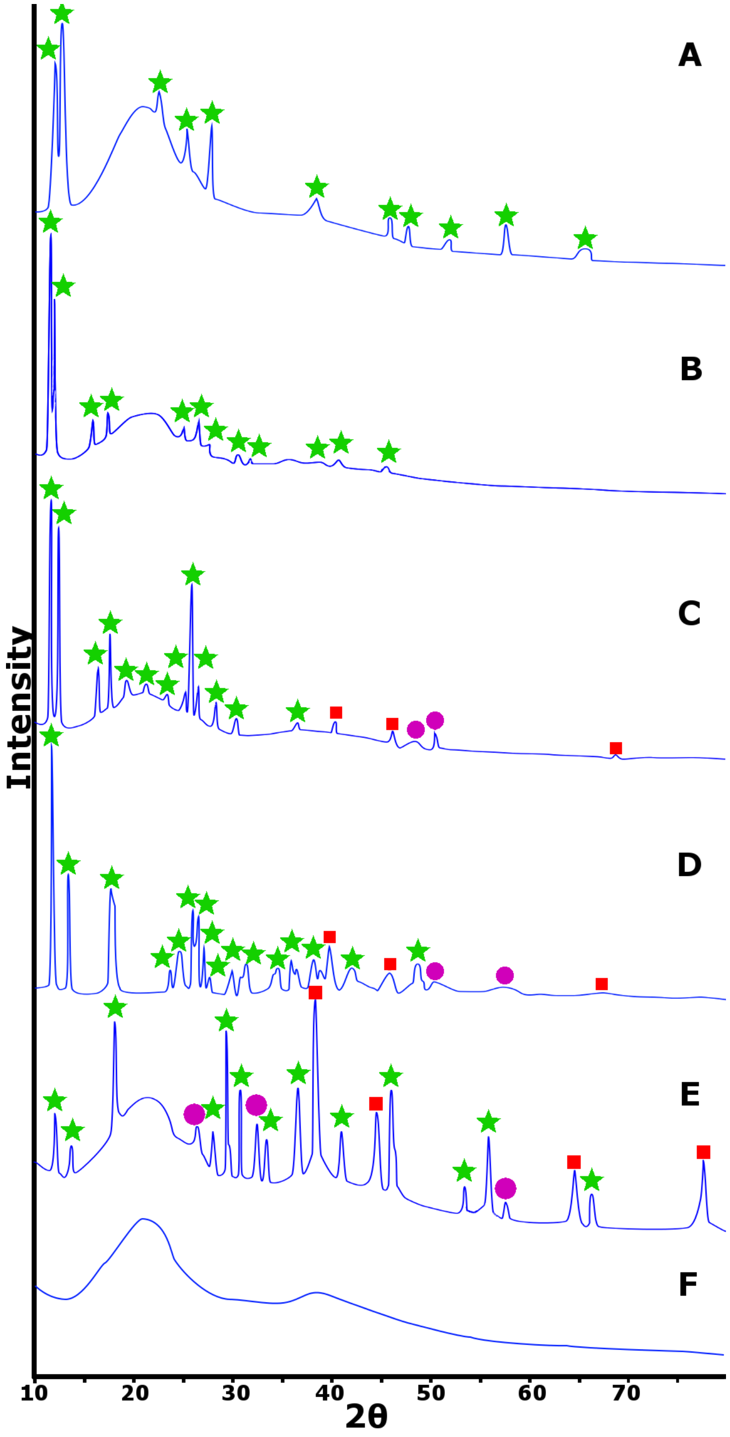

Figure 18: XRD pattern of various metal reduction reactions by CPCD on onion. A) $Zn(acac)_2$ on onion shows only peaks for precursor (green stars) B) $Cu(acac)_2$ on onion showing only peaks for precursor (green stars) C) $Pd(acac)_2$ on onion shows peaks for precursors (green stars), a few low intensity peaks for Pd metal (red squares), and two unidentifiable peaks (purple cirlces) D) $Pt(acac)_2$ on onion shows peaks for precursor (green stars), peaks for Pt metal (red squares), and unidentifiable peaks (purple circles) E) Ag(acac) on onion shows peaks for precursor (green stars), peaks for silver metal (red square), and unidentifiable peaks (purple circles) F) laser irradiated onion.

Conclusions

Utilizing Confined Plume Chemical Deposition (CPCD) conditions on a bromo-(triethylphosphine)gold precursor on a *Allium cepa Baja Verde* support, gold particles were deposited along onion cell walls as 2 µm to 4 µm cubes. XRD confirms that polyol reduction is the most likely pathway based on which metal precursors can be reduced under the condition of CPCD. Production of metal particles by CPCD represents a much faster method to produce such materials. Reducing and depositing metal nanoparticles on living tissue with some degree of spatial control indicates CPCD is a new synthesis strategy relevant to new applications of nanotechnology.

CHAPTER V

PREPARATION OF SURFACE-PASSIVATED LANTHANIDE METAL MICROPOWDERS FOR MAGNETIC RESONANCE FORCE MICROSCOPY

General Introduction

Magnetic Resonance Force Microscopy New materials with novel properties and improved performance are being created by controlling their composition and structure at the nanometer scale. Progress in the development of these novel materials will depend on instruments capable of providing localized information on the structural, electronic, and magnetic properties of these systems. Current techniques are unable to characterize and image the buried interfaces of multicomponent systems, which is an essential requirement for continued progress.

Magnetic Resonance Force Microscopy (MRFM) is a novel technique which combines the chemical specificity of magnetic resonance spectroscopy with the high spatial resolution of atomic force microscopy (AFM). This technique enables nondestructive characterization of surface and subsurface composition at the nanometer scale for a broad range of materials. The spatial resolution is limited by signal to noise ratio of the interrogated volume, and has recently been shown by the IBM group to be sensitive enough to detect and resolve a single electronic spin.[73] MRFM is a general technique that can be used to study most materials.[6,74–76]

MRFM uses a magnetic tip on a flexible micromechanical cantilever in an external radio-frequency field. The interaction between this probe and the sample is detected by measuring the displacement of the cantilever, which is oscillated above the surface. The local gradient of magnetization is measured by detecting the shift in natural frequency of the cantilever. The sensitive slice is a product of the external field, particle shape, and the magnetic saturation of the particle. Only the external field can be changed during an experiment, so particles with a reasonable shape and high magnetic saturation are desired.

The size of the particles to be used has been shown by Longenecker to be dependent on the size of the sample to be analyzed. In general the optimal radius of the particle is three times the distance from the particle to the area of interest. This means for a sample that is up to 3 µm thick, a particle with a radius of 9 µm is desired to interrogate the entire sample. Micrometer thick particles of materials with high magnetic saturation are not commonly produced and must be custom be fabricated.[77]

Magnetic Particle Synthesis A joint project between SRNL and Vanderbilt University, sponsored by Dr. Matthew S. Wellons at SRNL, had been established with the goal of discovering successful synthesis strategies for the preparation of air-stable microparticles of dysprosium or holmium metals. Dysprosium and holmium are ideal magnetic materials because they have the highest magnetic saturation found, 3.5 T[78] and 3.87 T[79] respectively. Ideal magnetic particles will be ten to twenty micrometers in diameter. The preparation of these metals will be dealt with in three sections. First chemical reduction will be discussed, then mechanochemical reduction, and finally physical preparation methods.

Introduction to Chemical Reduction of Dysprosium Salts

Chemical reduction of rare-earth compounds to form small metal particles is a notoriously difficult problem, for example dysprosium and holmium both have a reduction potential of −6.9 eV[80]. The only known example is alkalide reduction of $GdCl_3$ in THF solution using an excess of $[K^+(15\text{-crown-}5)_2]Na^-$ forming an intermediate dispersion of Gd nanoparticles. Subsequent addition of $AuBr_3$ solution leads to reduction of Au(III) ion and surface passivation through formation of a gold metal shell layer.[4] To date, there have been no other reports of rare-earth metal particle formation via chemical reduction, much less at the micrometer size.

Reduction of $DyCl_3$ by Solvated Electrons Solvated electrons are the strongest reducing agent possible in any given solvent system, but most solvents are reduced by such a strong reductant. In addition, rare-earth halides have low solubility in most solvents, so the solvent of choice must both form a stable solvated electron species and dissolve a rare-earth halide precursor.

Using liquid ammonia as solvent is undesirable due to the anticipated low solubility of dysprosium halides at $-33\,°C$. However, using an amine that is liquid at room temperature and known to form solvated electron species, such as ethylenediamine, precludes this low-temperature problem. Addition of sodium metal to purified ethylenediamine at room temperature generates the expected beautiful blue color of solvated electrons. When this blue solution is added to a solution of $DyCl_3$ in THF, a white precipitate forms immediately. Following isolation, characterization of this white product solid by powder XRD and SEM-EDS indicates the absence of dysprosium metal. Powder XRD patterns show only very broad peaks consistent with dysprosium oxide. Literature reports confirm the high stability of Dy(III) coordination complexes with amines in general, and of $[Dy(en)_3]^{+3}$ specifically. Amine solvents are impractical for dysprosium-ion solution reduction.

Reduction of Dy(III) Ion using Electron-Transfer Agents Given that $DyCl_3$ dissolves best in THF, chemical reduction by alkali metal was attempted using THF-soluble, electron-transfer agents. Initially naphthalene was chosen because of the high reduction potential ($-2.5\,eV$) of naphthalenide ion. A sodium naphthalenide solution in THF was prepared in 10-fold molar excess and was added to a THF solution of $DyCl_3$. Following this addition, a THF solution of $PtCl_2$ was slowly added to the reaction solution in an attempt to surface-passivate any formed Dy particles with a shell of Pt metal, a color change from blue to yellow was noted. A black powder was isolated following the washing away of organic by-products with benzene and hexane and ionic salts, such as sodium chloride, with ethanol and water.

Although powder XRD patterns reveal the presence of only sodium chloride and Pt nanoparticles, SEM-EDS elemental mapping show dysprosium atoms co-localized with platinum atoms, see Figure 19. XRD diffraction peaks consistent with the formation of either Dy metal or Dy-Pt alloy are not observed, so successful reduction of Dy(III) ion cannot be confirmed.

To increase the mass of Dy(III) ion available for reduction, a very soluble neutral, organometallic complex of Dy(III) was purchased. Tris(isopropylcyclopentadienyl)-dysprosium was dissolved in THF and was treated with a 10-fold molar excess of sodium naphthalenide in THF. A small amount of platinum salt, di-μ-chloro-dichloro-bis(ethylene)-diplatinum(II), was added as a THF solution to coat any formed dysprosium particles, a color change from blue to pale yellow was noted. Upon workup by washing with benzene, hexane, ethanol, and water, only a black tar was isolated. Strong Lewis acids are known to ring-open polymerize THF, which can appear as a thick gel. This thick gel with black metallic nanoparticles most likely is the black tar observed. Because this tar did not lend itself to further analysis, tris(isopropylcyclopentadienyl)dysprosium was abandoned as a source of Dy(III) ion.

Chemical reduction of $DyCl_3$ was then attempted using the diphenylketyl radical anion of benzophenone. Alkali diphenylketyl ion was generated by dissolving sodium/potassium alloy in a THF solution of benzophenone. The resulting blue ketyl radical ion solution was then added dropwise to a THF solution of $DyCl_3$ in a 10-fold molar excess, no color change is immediately evident as there is excess blue ketyl radical. A platinum salt, dibromoplatinum(II), was added as a THF solution to surface passivate any formed dysprosium particles, and a color change from blue to yellow/brown is noted. After working up the product by washing with acetone and water, a black free-flowing powder was isolated. This powder smoldered and ignited upon exposure to air. This flammable behavior is consistent with dysprosium metal having been formed.

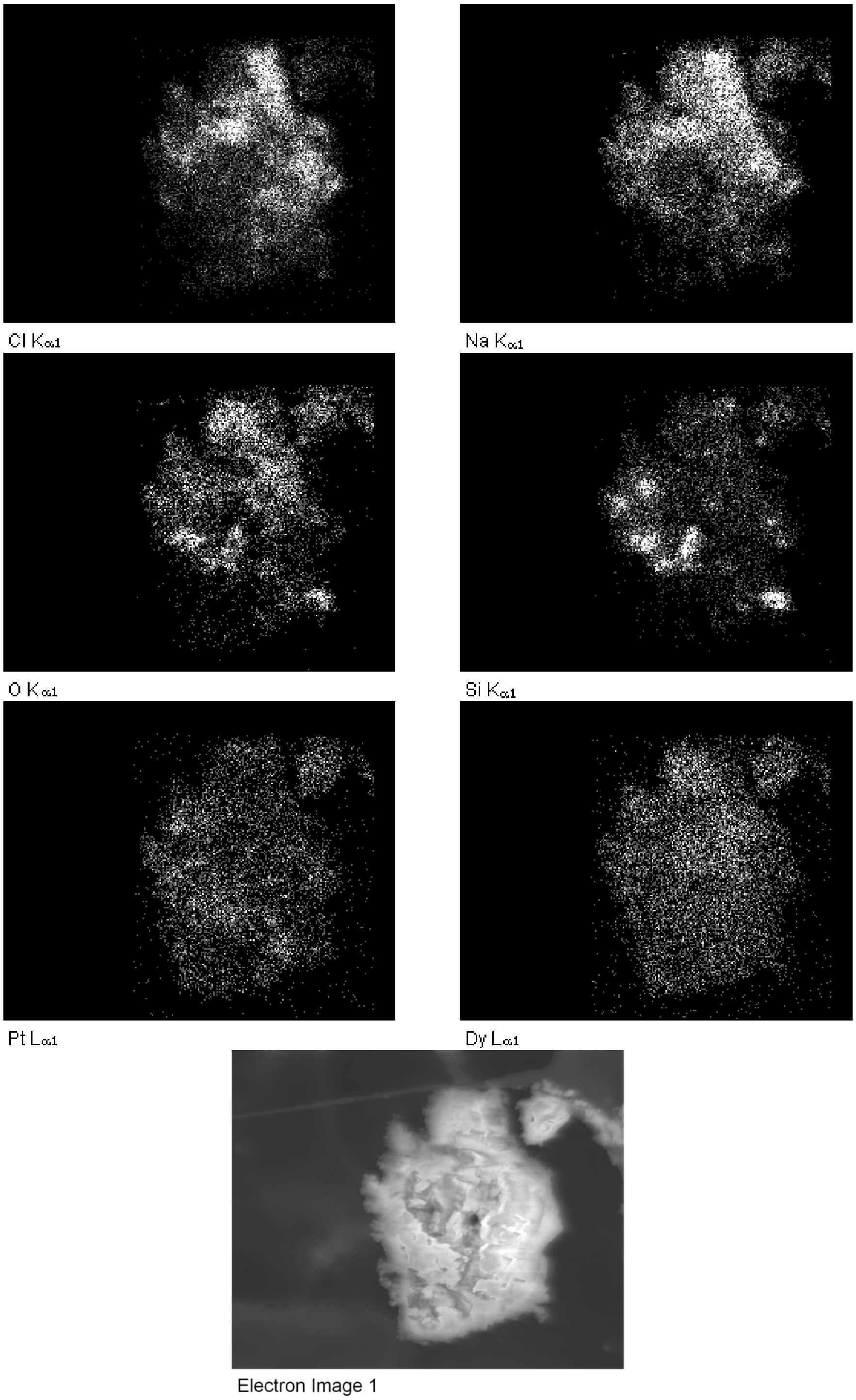

Figure 19: SEM-EDS of Pt-coated Dy reduced by sodium napthalenide. Na and Cl are localized together, Si and O are localized together, and Dy and Pt are localized together. This co-localization is most consistent with NaCl, SiO_2, and PtDy alloy being present.

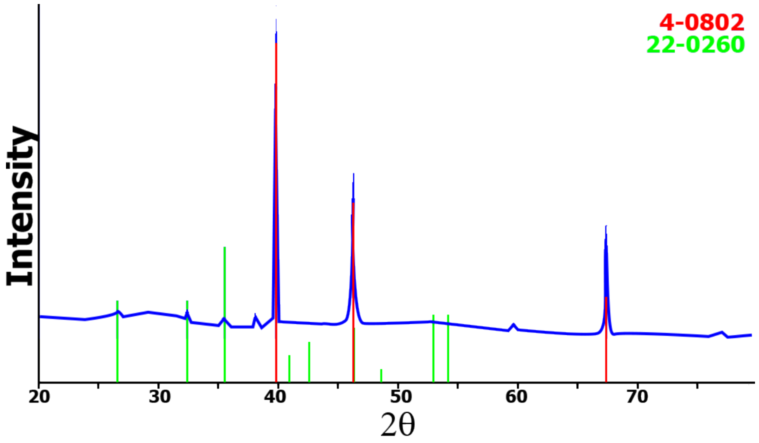

Figure 20: XRD pattern of Pt-coated Dy from reduction of $DyCl_3$ with alkali diphenylketyl. Sample caught fire upon exposure to air. Red lines indicate Pt (PDF# 4-0802) and green lines indicate DyOCl (PDF# 22-0260).

Powder XRD analysis shows the presence of platinum metal and dysprosium oxychloride, see Figure 20. SEM-EDS elemental mapping indicates dysprosium, platinum, and oxygen all localized within the same area. Formation of this black powder is an encouraging result, as it is possible that dysprosium oxychloride is formed from air oxidation of Dy metal particles due to imperfect surface passivation by Pt metal.

With the difficulties presented through use of other electron-transfer agents, THF solutions of $[K^+(15\text{-crown-}5)_2]Na^-$ were examined as a reducing agent. It was found that $[K^+(15\text{-crown-}5)_2]Na^-$ in THF decomposes at room temperature over a few hours. This decomposition time necessitates quick transfers and reactions. In a typical reaction a 10-fold molar excess of $[K^+(15\text{-crown-}5)_2]Na^-$ over dysprosium halide was generated in situ using a 2:1 ratio of 15-crown-5 ether to sodium-potassium alloy in THF with stirring for 1 hour. $[K^+(15\text{-crown-}5)_2]Na^-$ was considered to be fully generated when the solution was dark blue and the beads of sodium-potassium alloy were no longer visible. 200 mL of a 1 mM DyX_3 (X=Cl or I) solution in THF was added over 1 hour using a dropping funnel. 100 mL of a 3 mM $HAuCl_4$ solution in THF was added over 30 minutes. The reaction was allowed to continue stirring for 15 minutes after all the gold salt was added. The products were isolated by centrifuging

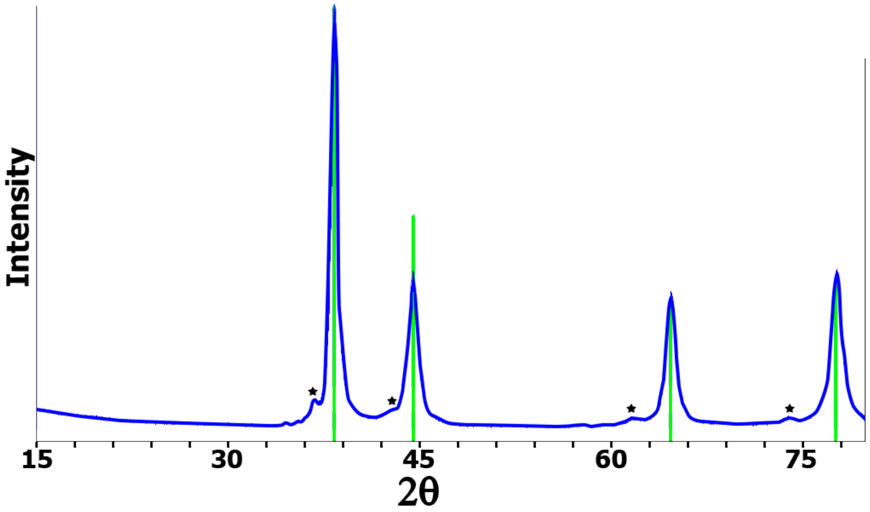

Figure 21: XRD pattern of Au-coated Dy from reduction of DyI_3 with $[K^+(15\text{-crown-}5)_2]Na^-$ in THF. The green lines correspond to gold (PDF# 04-0784) and the stars indicate another cubic phase, consistent with a DyAu alloy. The lattice parameter of the expanded phase is 4.22 Å (3.5% expanded from pure Au).

at 3000 RPM. These products were washed with methanol, acetone, and water to remove any $[K^+(15\text{-crown-}5)_2]Na^-$, NaCl, or other side products. A black powder was isolated that was stable in air.

This powder was analyzed by XRD, SEM-EDS, and TEM-EDS. Powder XRD shows peaks for gold, and minor peaks consistent with a similar cubic structure to gold, but expanded lattice constant, see Figure 21. These minor peaks are consistent with a gold-dysprosium alloy. Vegards Law is not valid for this alloy in the absence of diffraction data for a known fcc dysprosium-gold alloy phase. SEM-EDS shows Dy and Au localized together consistent with alloy formation, and emission peaks for carbon and oxygen are consistent with CO and/or O_2 adsorbing to the powder surface, see Figure 22. TEM-EDS shows separate gold particles as well as areas with both gold and dysprosium localized together. From TEM analysis, there is evidence of oxidation in the dysprosium particles indicating a sufficiently passivating shell was not formed, but this observation is also consistent with an alloy forming and the dysprosium selectively being oxidized out of the alloy.

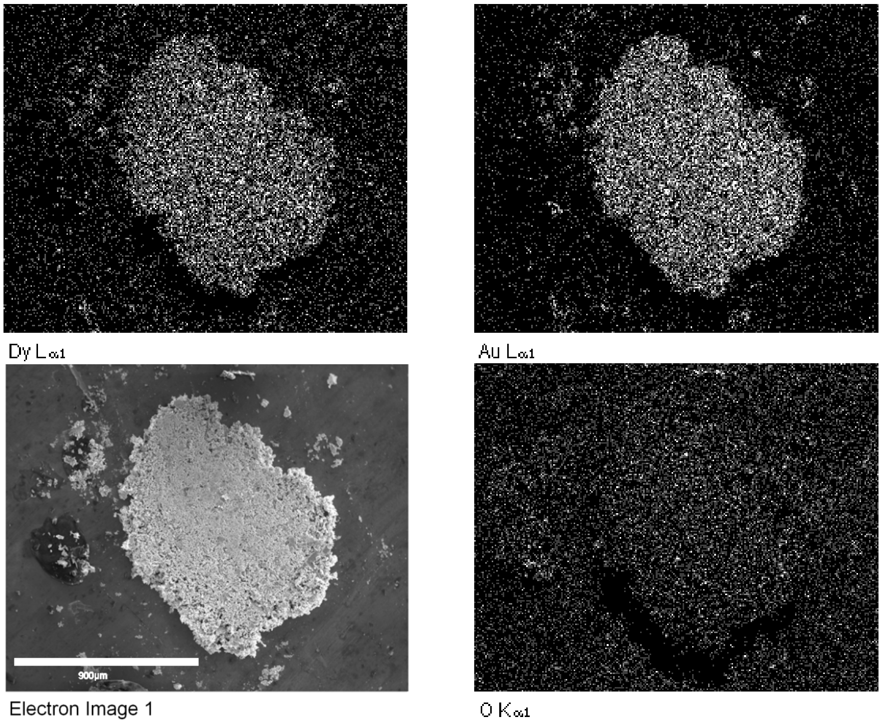

Figure 22: SEM-EDS mapping of an aggregate cluster from the reduction of DyI_3 with $[K^+(15\text{-crown-}5)_2]Na^-$ in THF. The dysprosium and gold are well correlated together and the oxygen peak is consistent with adsorbed O_2 on the surface.

To remove the influence of the capping shell, chemical reduction was attempted again without a gold capping layer. In a typical reaction a 3-fold molar excess of $[K^+(15\text{-crown-}5)_2]Na^-$ over dysprosium iodide was generated in situ using a 2:1 ratio of 15-crown-5 ether to sodium-potassium alloy in THF with stirring for 1 hour. $[K^+(15\text{-crown-}5)_2]Na^-$ was considered to be fully generated when the solution was dark blue and the beads of sodium-potassium alloy were no longer visible. 300 mL of a 2 mM DyI_3 solution in THF was swirled for 15 minutes. $[K^+(15\text{-crown-}5)_2]Na^-$ was added to the DyI_3 solution drop wise by addition funnel at a rate of ca. 9 mL/min. The reaction was swirled for 15 minutes after all the $[K^+(15\text{-crown-}5)_2]Na^-$ was added. The products were isolated by centrifuging at 3000 RPM. These products were washed with THF and diglyme to remove KI and any residual reactants. A black powder was isolated.

Powder XRD patterns of this powder inside a sealed XRD sample holder reveal diffraction peaks from dysprosium metal, potassium iodide, and dysprosium oxide, see Figure 23. There are many unassigned peaks as well, and such a mixture makes it difficult to analyze the pattern definitively. Without any viable way to separate the dysprosium metal from side products, this synthesis method was abandoned in favor of a new method.

Reduction of Dy(III) Ion by Planetary Ball Milling with Calcium Reduction of Dy salts using mechanochemical synthesis techniques was attempted as a novel synthesis strategy for obtaining Dy micropowders. With traditional wet chemistry techniques, solvation spheres exist which mitigate the reduction potential of reaction agents; however, mechanochemical techniques overcome this limitation by grinding reagents in the solid state. The high-energy impacts of grinding balls with the sides of the chamber generate short term forces capable of causing chemical reactions, like oxidation/reduction[81]. Mechanochemical reactions are driven by thermodynamics, not solution oxidation/reduction potentials or solution kinetics.

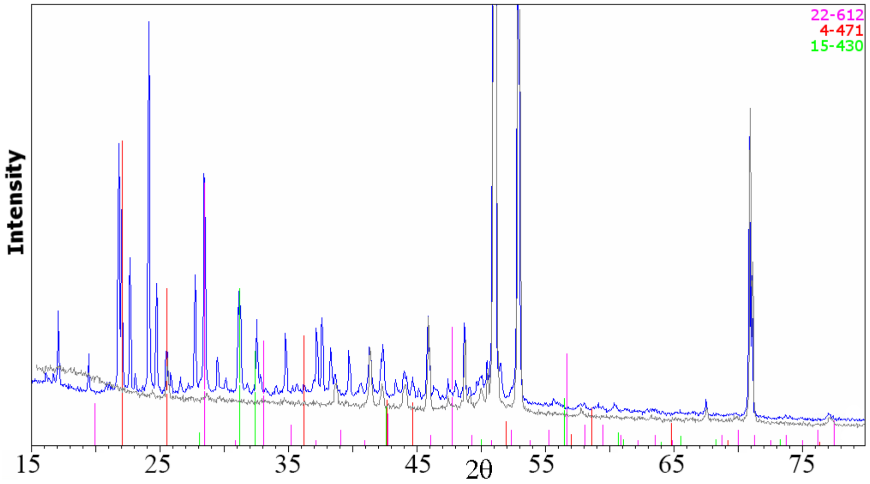

Figure 23: XRD pattern of powder from reduction of DyI_3 with $[K^+(15\text{-crown-}5)_2]Na^-$ in THF. The purple lines correspond to Dy_2O_3 (PDF# 22-0612), the red lines correspond to KI (PDF# 04-0471), and the green lines correspond to Dy metal (PDF# 15-0430). There are many more phases present and assigning all peaks becomes an intractable problem.

Reduction of DyF_3 to Dy^0 has been successfully implemented in a tube furnace using direct reaction with calcium metal. To attempt this synthesis via ball milling, a proof of concept synthesis was attempted. A small disperser container was loaded with 0.250 g $DyCl_3$ and 0.110 g Ca with about 0.1 g (ca. 20) 10 mm steel balls. These materials were then agitated by an internal peg. The proof-of-concept reaction worked well, forming a dark powder around the chunks of calcium. With these encouraging results, the reaction was scaled up to a planetary ball mill (Retsch PM100). A large stainless steel jar was loaded with 0.115 g of calcium pieces, 0.601 g $DyCl_3$ powder, and 0.20 g (ca. 40) 10 mm hardened steel balls in a glove box. The jar was then secured with an air tight clamp and brought out of the box and loaded into the planetary ball mill. The mill was run at 500 RPM for 2 hours and allowed to cool. The jar was then pumped back into the glove box for disassembly and analysis of contents. Using an air-tight XRD holder the products were analyzed by XRD.

X-ray diffraction patterns show a broad peak consistent with nanoparticulate dysprosium metal. Some of the powder was brought out and exposed to air; rapid bubbling consistent with dysprosium metal reacting with water was noted ($CaCl_2$ co-product is deliquescent). TEM-EDS of this sample shows Dy, Cl, and O spatially well correlated and Ca as a coating, see Figure 24. It is difficult to deduce much structural information though as the particles were quite aerated and would collapse under TEM inspection.

The above reaction was repeated using DyF_3 in place of $DyCl_3$. XRD analysis of the resulting black powder shows four broad peaks that are assignable to a fcc unit cell and one peak assignable to CaF_2. The lattice constant of the fcc unit cell phase is consistent with those observed for nanoparticulate powders of rare-earth metals, like gadolinium and dysprosium.[82] TEM-EDS analysis of this powder reveals that Ca, F, and Dy are spatially well mixed, but regions of Ca and F are distinct from Dy. These maps are consistent with the XRD analysis, revealing formation of a highly dispersed mixture of nanoparticulate Dy and CaF_2, see Figure 26 and Figure 27. However, CaF_2 is insoluble in any solvent, which means separating it from the Dy metal is impractical. As the halides go from F to I, solubility increases for CaX_2 (X = halide).

To mitigate the inseparable coproducts problem, different halide salts of calcium were considered. It was found that from a thermodynamic point of view, DyI_3 reacting with Ca to form Dy^0 and CaI_2 was even more thermodynamically favorable than the fluoride, with a Gibbs free energy of formation between $-350\,\mathrm{kJ/mol}$ to $-460\,\mathrm{kJ/mol}$. 0.788 g of DyI_3 and 0.094 g of Ca were added to a stainless steel reaction chamber, with ca. 30 stainless steel balls. This chamber was sealed air-tight and placed into the planetary ball mill. The reaction was performed at 600 RPM for 5 hours at a -2:1 inner:outer spinning rate. After the reaction was stopped, the chamber was brought back into the glove box and unsealed. A black powder was observed. Using THF to transfer the powder and separate it from the grinding media, this suspension was then centrifuged at 3000 RPM for 30 minutes. The final black powder recovered was highly magnetic. The supernatant, which was decanted away, was a dark yellow color.

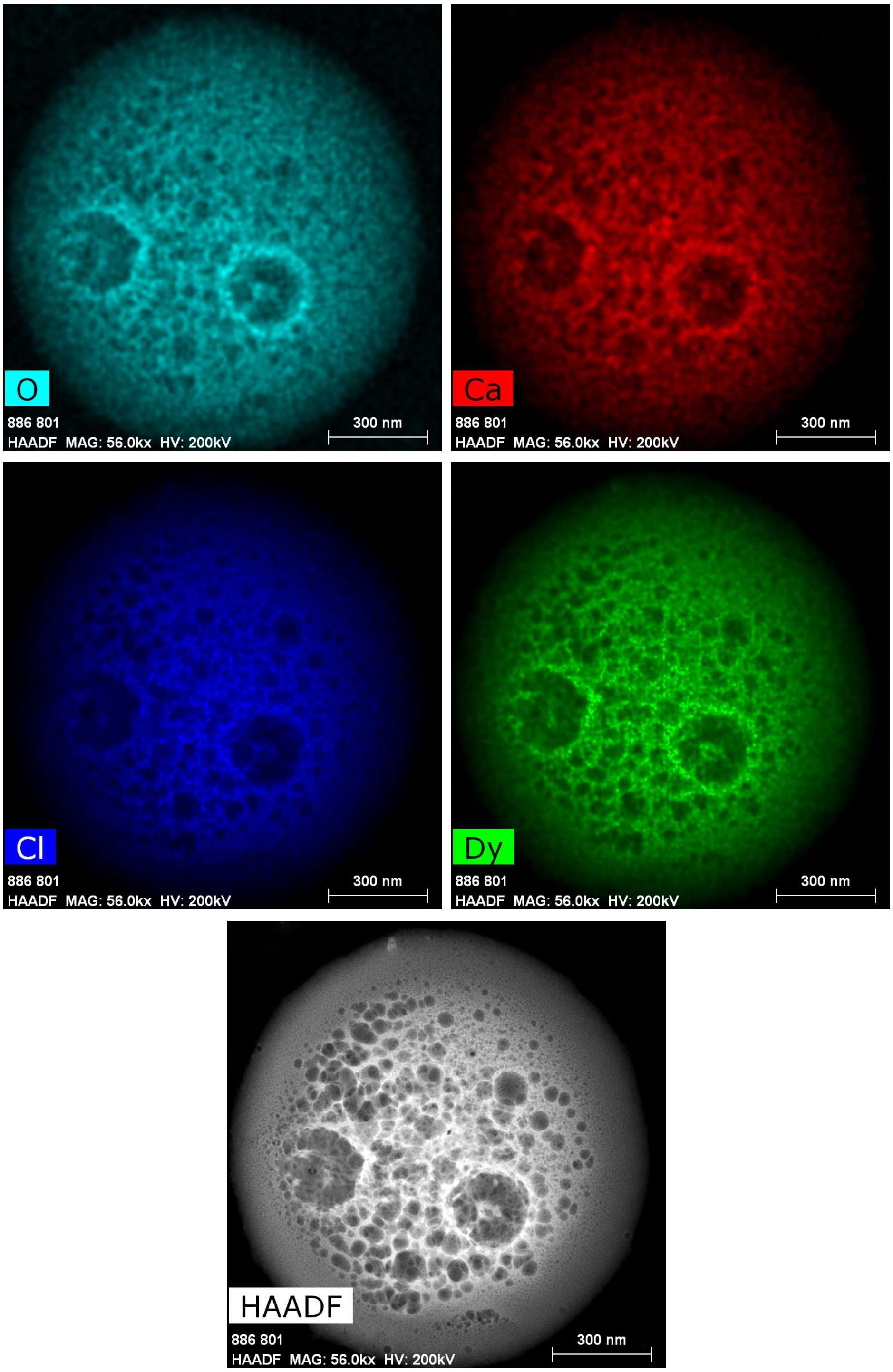

Figure 24: TEM of aerated particle from reduction of $DyCl_3$ with Ca by ball milling. Dy, Ca, Cl, and O are correlated and detailed structural information is difficult to deduce because the structure collapses quickly under TEM illumination.

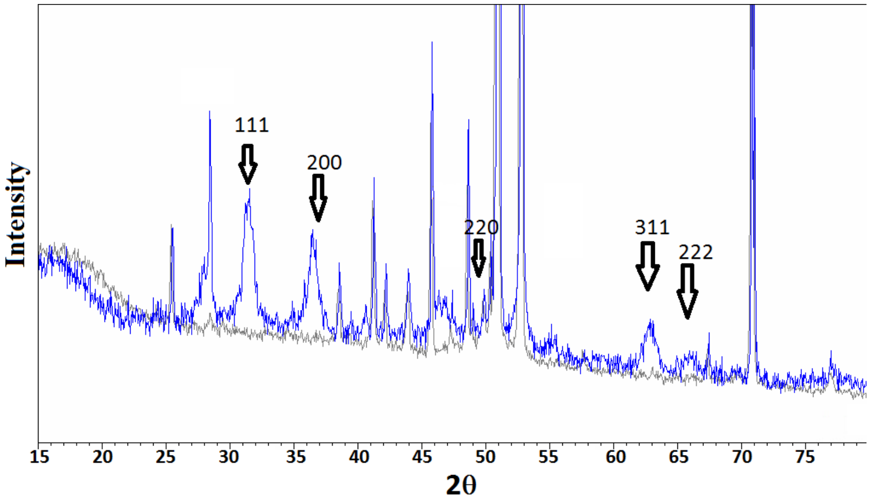

Figure 25: XRD of the product from the reduction of DyF_3 with Ca in the planetary ball mill. The indexed peaks are assigned to a fcc unit cell with a cell parameter, a = 4.90 Å. If this is assumed to be a fcc form of Dy metal, then the atomic radius would be 1.73 Å, which is close to the accepted literature value of 1.78 Å. The extra peaks around 28° and 47° 2θ are from CaF_2.

The black powder was then washed with hexane, which was decanted away as well, and allowed to dry for 2 hours in the glove box.

XRD analysis shows a large very broad peak consistent with Dy_2O_3 and a few low intensity peaks consistent with Dy metal. TEM-EDS shows extensive contamination from Fe, Cr, and Si, the first two of which are components of stainless steel and Si most likely from the detector. The individual particles were quite small (ca. 10 nm), but were agglomerated to about 0.5 µm to 1 µm particle size.

Physical Size Reduction of 40-mesh (<420 µm) Dysprosium Metal Particles With the difficulties presented through reduction of dysprosium salts, direct size reduction of 40-mesh dysprosium turnings was attempted through ball milling. It was found that ball milling dysprosium with 5 mm WC balls, ca. 5 mL of hexane, and 0.5 mL oleylamine produces promising particles of 1 µm to 10 µm. Figure 28 shows a representative SEM of the as received 40-mesh dysprosium particles, and Figure 29 shows the corresponding XRD pattern using the air-tight XRD holder. The as-received

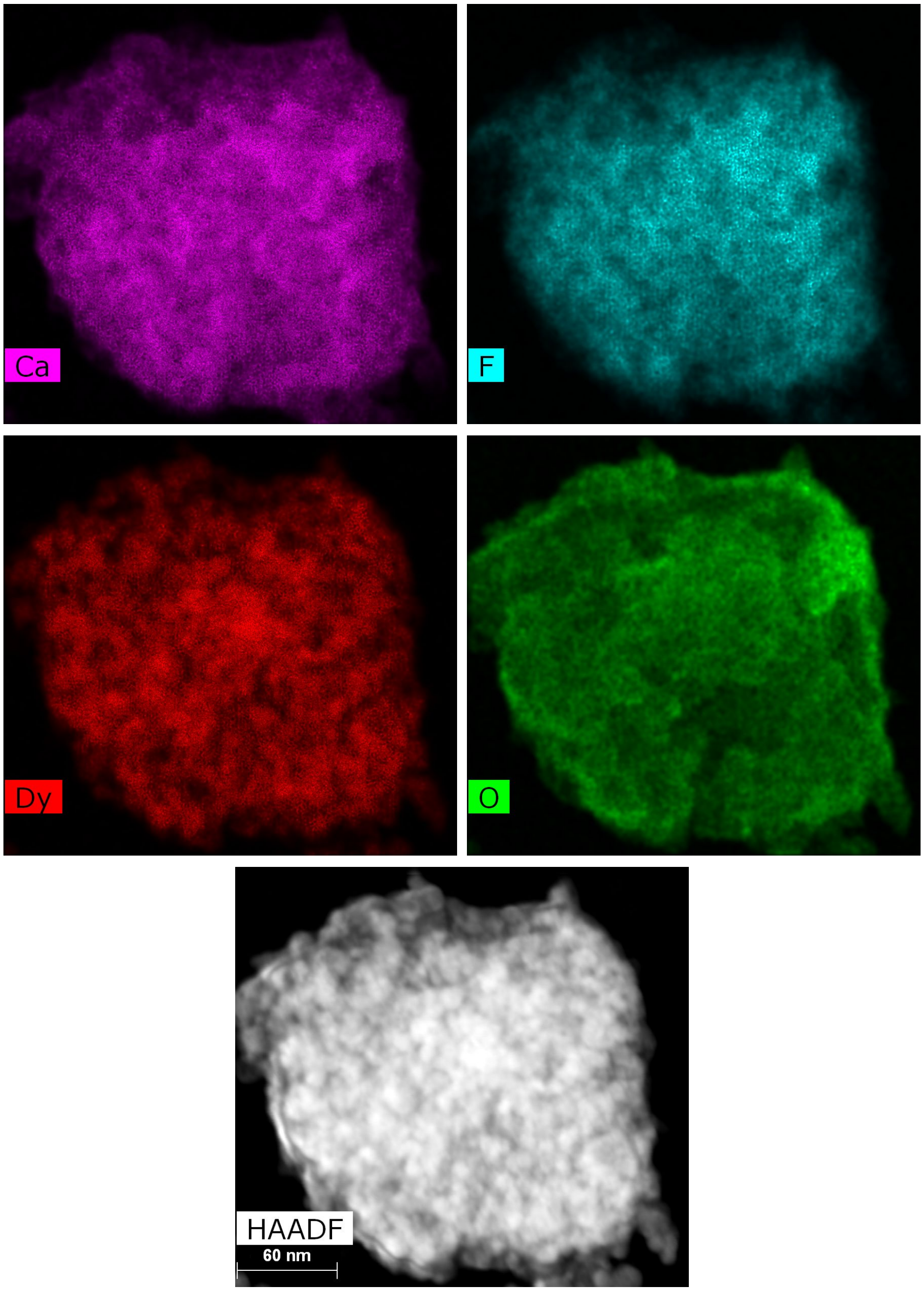

Figure 26: TEM-EDS mapping of product from ball milling DyF_3 with Ca pieces in a planetary ball miller for 5 hours at 600 RPM. Correlations can be noted between Ca and F, while Dy is absent, and vice versa indicating Dy and CaF_2 as coproducts; mapping of oxygen is consistent with absorbed O_2 on the surface. The agglomerate shown is about 250 nm wide.

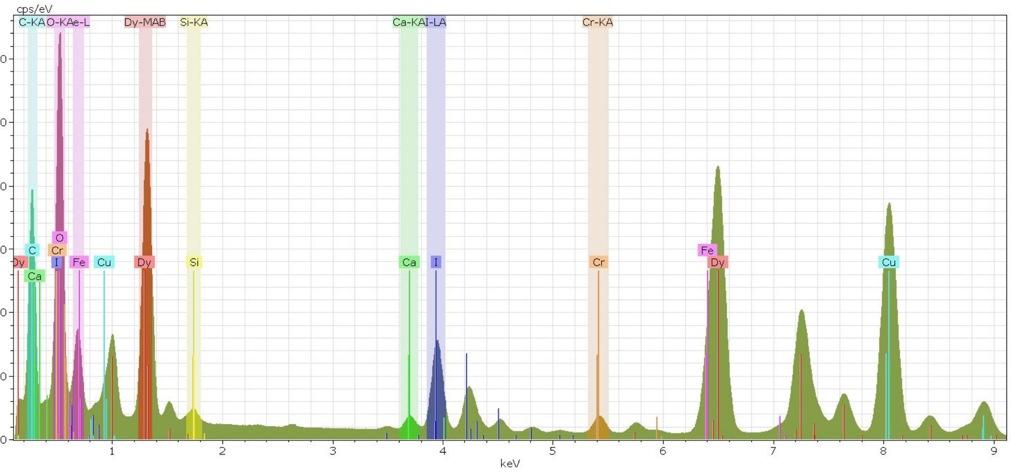

Figure 27: TEM-EDS spectrum from a typical particle from the reaction of DyI_3 mechanochemically reduced by Ca. There are zones of Fe, Cr, and Si within the Dy particle. The EDS spectrum shows Dy and O as the major elemental components, but Ca, I, Cr, Fe, and Si are also present in significant amounts. The Cu peak is due to the Cu grid, and not a signal in the sample. Fe and Cr are components of stainless steel, which is what the grinding chamber and media are made of. Si is most likely a contaminant from the detector.

dysprosium is under oil, and a hexane wash is used to remove all oil before grinding. In a glove box, 0.875 g of washed dysprosium is placed in the ball-milling chamber along with ca. 5 mL of hexane and 0.5 mL oleylamine. The chamber is sealed with an air-tight clamp in the glove box and brought out to be ground on the Retsch PM100 planetary ball mill for 30 min at 600 RPM with a -2:1 inner:outer spinning rate. Control experiments without the oleylamine show an unexpected diffraction peak in the XRD pattern at about 30° 2θ. Because the peak does not align with the expected position of Dy_2O_3, we are assigning it as a likely sub-oxide of dysprosium, just coating the surface. To mitigate the sub-oxide problem, grinding could only be performed for 10 minutes.

Adding oleylamine to hexane in the grinding chamber helped in a couple of different ways. First, the particles show an XRD pattern that more closely matches the expected intensities from the PDF card. Better alignment of the XRD patter is most likely due to a more equilibrium structure forming. Secondly, the sub-oxide peak

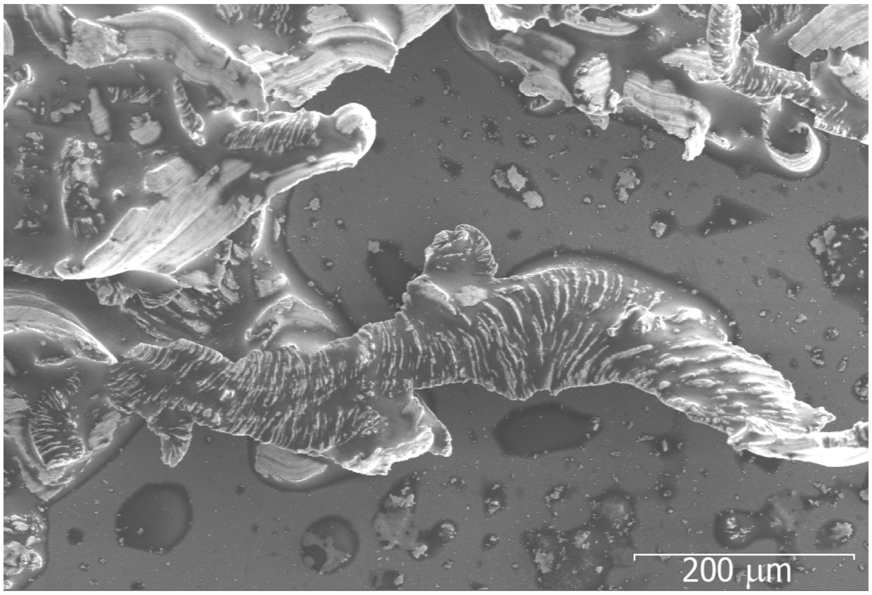

Figure 28: SEM of the as-received 40-mesh dysprosium. The particles are quite rough and not at all uniform in shape.

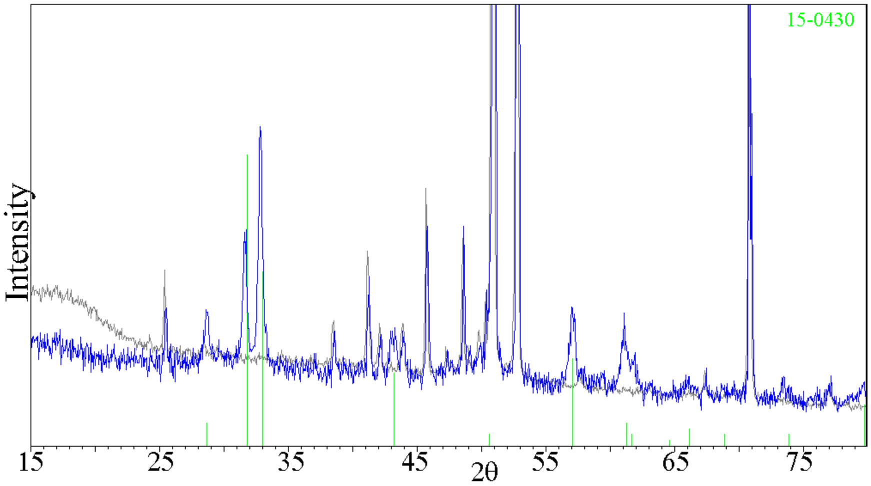

Figure 29: XRD of the as-received 40-mesh dysprosium. The green lines correspond to Dy (PDF# 15-0430). The grey trace is the background due to the air-free holder. The only peaks present are from dysprosium metal, however the intensities do not match the PDF card, so likely there is some preferential alignment.

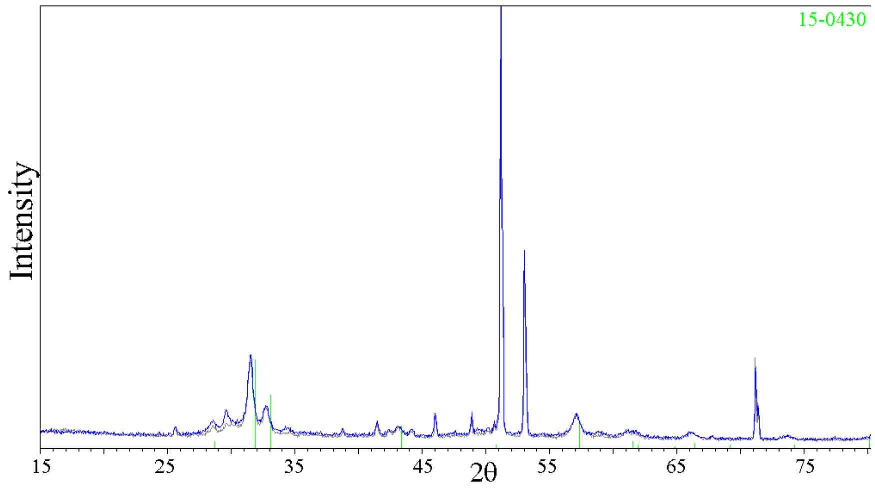

Figure 30: XRD pattern of product from ball milling 40-mesh dysprosium in a Retsch PM100 for 45 minutes at 600 RPM with hexane and oleylamine. The green lines are for dysprosium metal (PDF# 15-430), and the intensities match much more closely. An unidentified peak around 30° 2θ is visible (it was not visible in a sample milled for 20 minutes), and is assumed to be a sub-oxide coating on the surface of the dysprosium particles.

does not appear significantly in the XRD pattern until about 45 minutes of grinding, meaning smaller and more uniform particles should be obtainable, see Figure 30. After grinding, the vessel is brought back into the glove box to be opened. Then, using hexane, the ground powder is transferred to a centrifuge tube for particle size separation. To separate particles, the solution is agitated and allowed to settle for ca. 1 minute, then whatever is still suspended is transferred to a new centrifuge tube using a pipette as quickly as possible. Using this technique, reasonable particle size separation was obtained on a sample milled for 45 minutes, see SEM in Figure 31 (XRD of this product is Figure 30).

The particles were coated in a platinum capping layer. This capping layer was accomplished by suspending the freshly milled dysprosium in toluene with enough platinum hexafluoroacetylacetonate to coat the particles with ca. 10 nm of platinum. This suspension is refluxed overnight to initiate a transmetalation reaction. This suspension is allowed to cool and the platinum capped dysprosium particles are recovered through centrifugation at 3000 RPM. A black free-flowing highly magnetic powder is recovered.

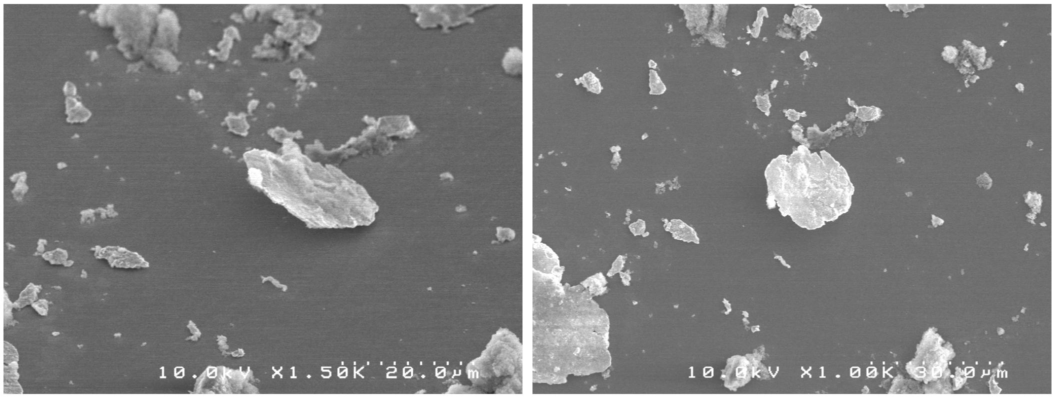

Figure 31: SEM image of product from ball milling 40-mesh dysprosium in a Retsch PM100 for 45 minutes at 600 RPM with hexane and oleylamine. Most of the particles are on the order of 5 µm to 10 µm, however there are particles as small as 0.5 µm and as large as 60 µm within this sample.As the two images show, these particles are very flat (the second image is a 45° tilt of the first image).

The particles still appear flat, shaped more like flakes after milling. To induce a more spherical shape, microwave heating was implemented. The idea is to heat the particles just enough to soften and lower their surface energy (which should be lowest with spherical shapes), but not enough to melt or to sinter into larger particles. Using one 30-second treatment at 300 W under an argon atmosphere, a slight rounding out of the particles was noted, see Figure 32 versus Figure 31.

Optimizing the rounding procedure with microwave treatment proved difficult. Instead rounding was performed by tumble milling. Tumble milling was performed in a glass vial with ca. 10 5 mm WC ball bearings, hexane and oleylamine for 72 hours, by spinning the vial with a rotary motor. SEM of a typical Dy size reduction reaction capped with Pt and then rounded by tumble milling is shown in Figure 33. EDS of this material shows that it is dysprosium metal co-localized with platinum. The SEM-EDS was taken on a carbon tab, which has oxygen adsorbed in the surface, see Figure 34. A line-scan profile of the EDS map confirms that the dysprosium and platinum are co-localized and the oxygen signal is constant across the sample (i.e. not from oxidized dysprosium), see Figure 35. This procedure yields the best quality micro-particulate powder of Pt-stabilized Dy metal yet achieved.

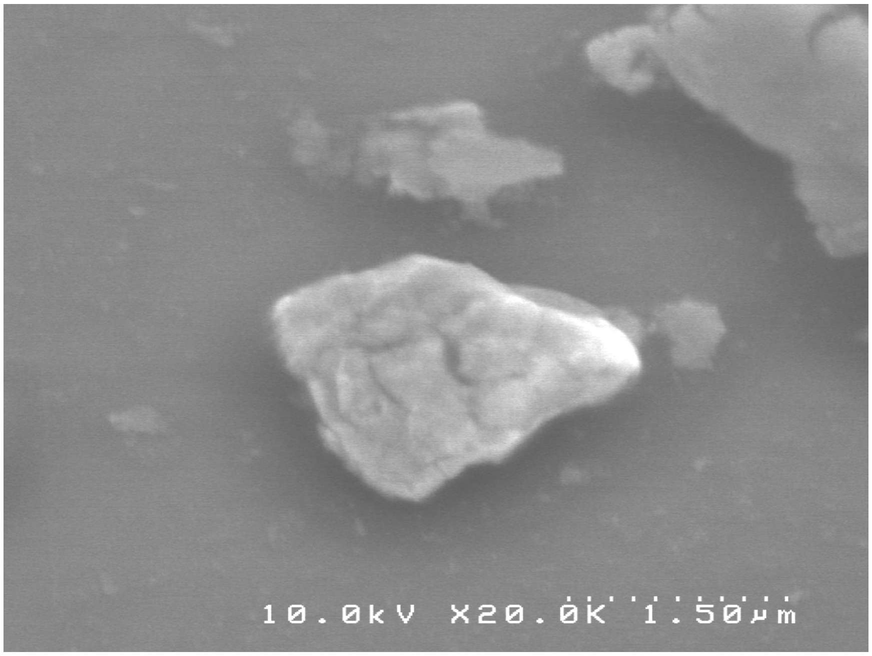

Figure 32: SEM of a typical particle from the microwave softening of dysprosium that was ball milled for 45 minutes with hexane and oleylamine. This image was taken at a 45° slant to emphasize that the particle is no longer flat like a flake (as it was originally). This particle is ca. 1.5 µm wide, 1 µm deep, and 1 µm tall. The particles are still between 5 µm to 10 µm on average, but this particle was isolated enough to demonstrate the rounding effect of the microwave softening.

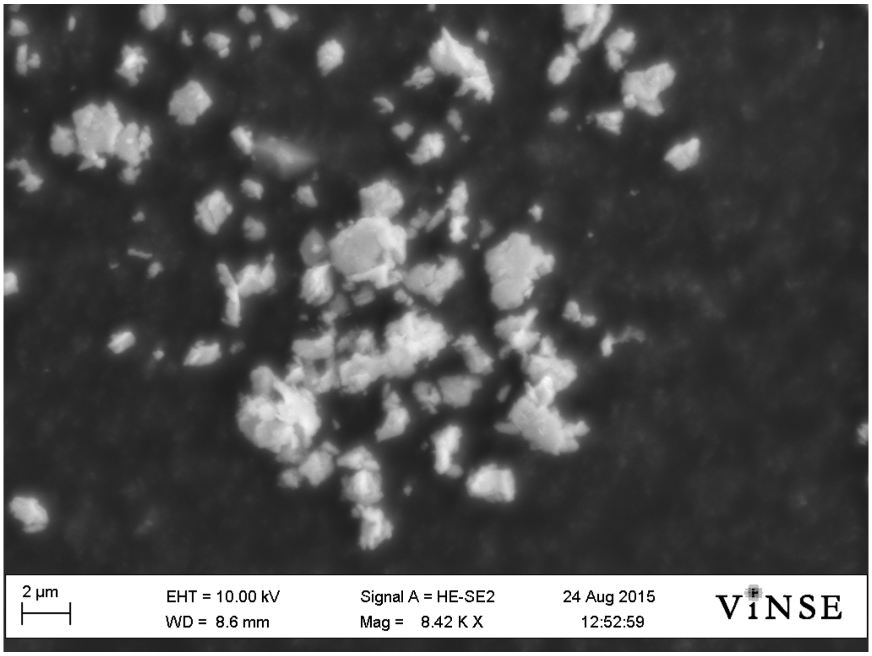

Figure 33: SEM of Pt-coated Dy particle rounded by tumble milling. The particles are about 1 µm to 10 µm and show about 20 % are spherical.

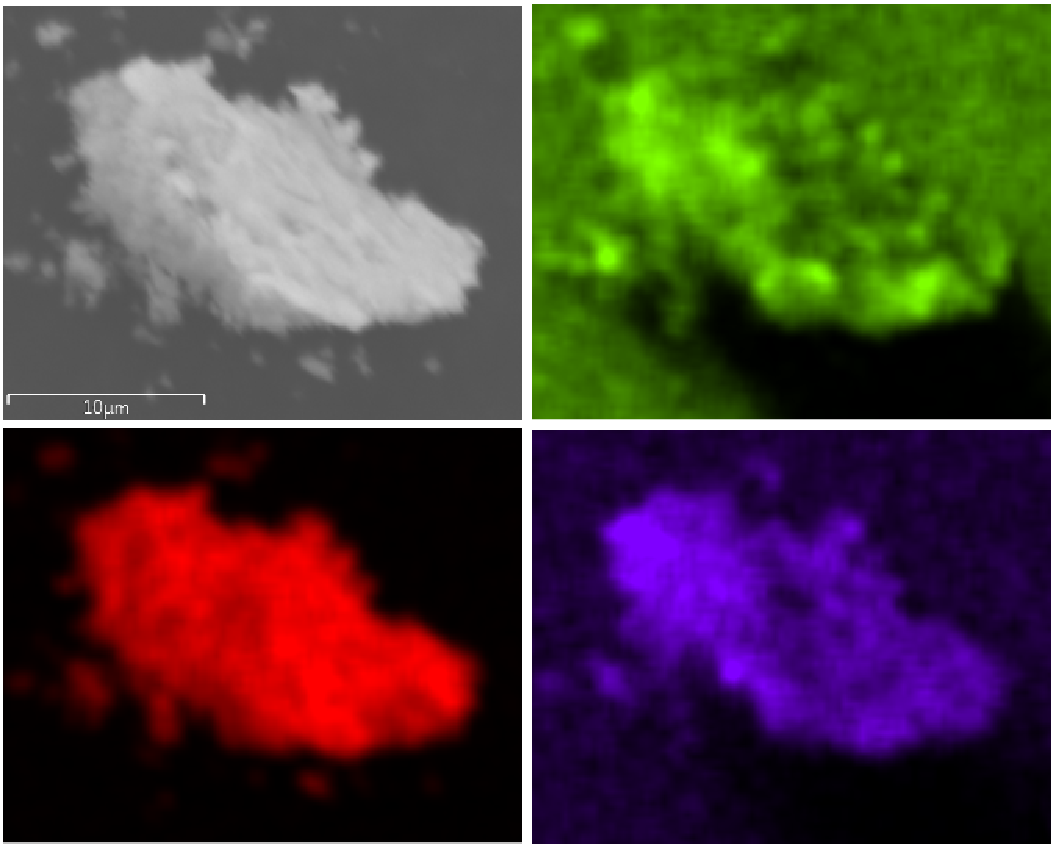

Figure 34: SEM-EDS showing selected elements in a typical Pt-coated Dy particle rounded by tumble milling. The Pt and Dy are colocalized together, and O is shown everywhere.

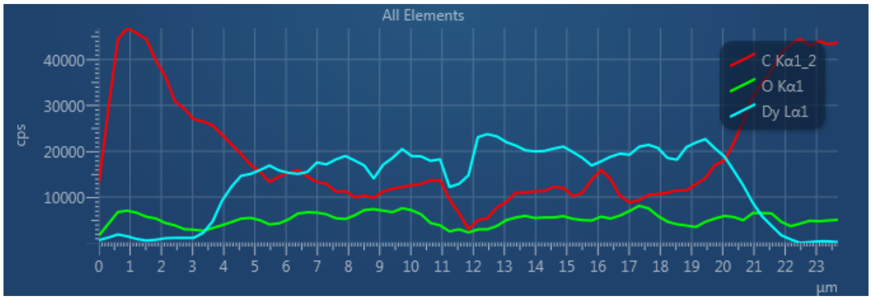

Figure 35: Line scan from SEM-EDS showing the change in concentration of selected elements across a particle. The scan was started and ended on a carbon background. The constant oxygen concentration across the scan indicates very minimal oxidation of the Dy particle.

The magnetic properties of the as synthesized dysprosium particles were measured. First the mass magnetization was measured as a function of temperature, see Figure 36. Dysprosium is known to go through two magnetic ordering transitions as temperature is lowered from about room temperature (300 K) to 4 K. The first transition is a paramagnetic to antiferromagnetic ordering transition at about 179 K, and the second transition is a antiferromagnetic to ferromagnetic ordering transition at about 85 K.[83] These known transitions correspond to what is seen the measured mass magnetization versus temperature curve with a paramagnetic to antiferromagnetic ordering transition occuring at about 179 K and a antiferromagnetic to ferromagnetic ordering transition occuring at about 73 K. Next the magnetic hysteresis at 4.2 K was measured, see Figure 37. Dysprosium is known to have magnetic saturation of about $350\,\mathrm{A\,m^2\,kg^{-1}}$.[83] This is about double what is seen for the as synthesized material; however, the literature value was measured for a single crystal and the synthesized sample is an agglomeration of polycrystaline microparticles. This difference in crystallite domain size could be responsible for this difference in magnetic saturation, but more experimentation is needed.

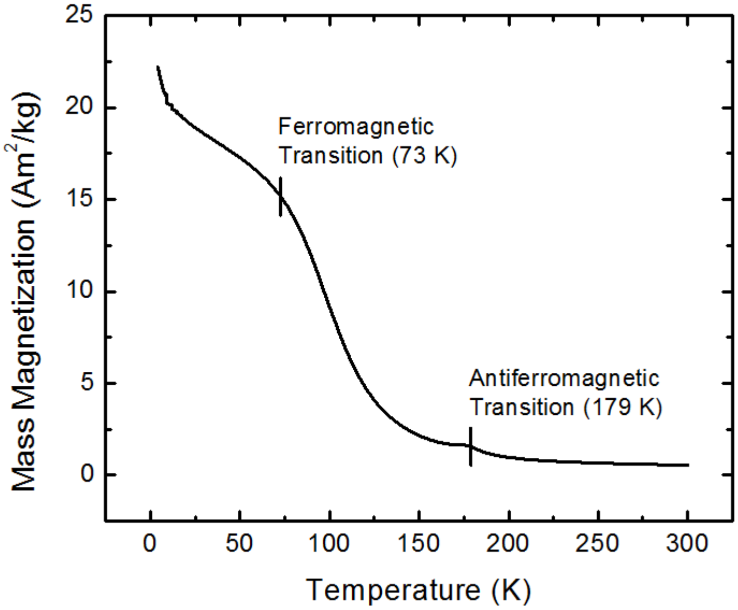

Figure 36: The temperature dependence of Pt coated Dy micropowder sample magnetisation measured in magnetic field of 1000 Oe. Two inflection points are seen, which correspond to two transitions in magnetic ordering in the sample. See text for discussion

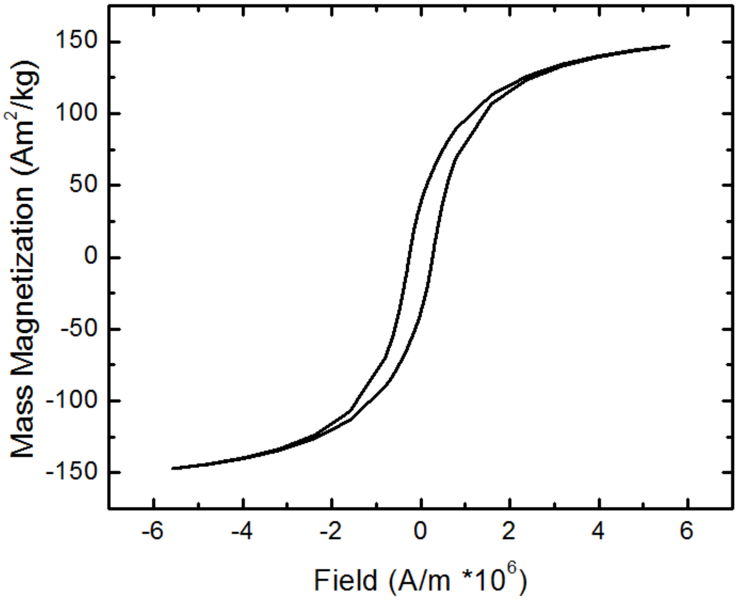

Figure 37: Magnetic hysteresis curve of Pt coated Dy micropowder sample recorded at 4.2 K. Magnetic saturation is seen at $147\,\mathrm{A\,m^2\,kg^{-1}}$. The coercivity is seen to be $259\,\mathrm{kA\,m^{-1}}$.

Discussion and Conclusion

From the three methods attempted to prepare microparticles of air-stabilized lanthanide metal several observations can be made. First, solution reduction of simple dysprosium salts or organometallic reagents is thwarted by incomplete reduction of dysprosium ions, dysprosium complexation to Lewis basic amine solvents, incomplete noble metal surface passivation, metal alloy formation, and complex mixtures of reaction products. Second, mechanochemical reduction of Dy(III) halide powders with calcium metal gives nanoparticulate Dy metal powders, elemental contamination by stainless steel grinding media, and formation of intractable co-products, such as CaF_2. Finally, planetary ball milling of commercial 40-mesh dysprosium powder with WC grinding media in the presence of oleylamine followed by platinum-metal surface passivation and rounded by tumble milling gives platinum-stabilized dysprosium micropowder specimens. Up to 0.5 g sample batches can be formed using this procedure. While the obtained microparticles have irregular shapes with rough surface topologies and a wide size distribution, powder sieves and SEM harvesting can be utilized to select specific particles for MRFM application. Approximately twenty percent of formed particles have appropriate shape and size for MRFM application.

APPENDIX A

CONFINED-PLUME CHEMICAL DEPOSITION AND PHOTOLUMINESCENCE CHARACTERIZATION OF YTTRIUM BORATE POWDERS DOPED WITH LANTHANIDE PHOSPHORS

General Introduction

Radiation detection is a necessary safety consideration in areas where high radiation dosage is expected. Most radiation is detected using scintillation detectors, which are short time period.[84,85] Long-term detection of radiation damage, where the maximum damage in an area can be detected at some future data, is also a safety consideration. Yttrium borate doped with a lanthanide is one such possible long-term radiation sensor.[86] Yttrium borate powders can be synthesized by a multitude of techniques, including sol-gel[87], spray pyrolysis[88], hydrothermal synthesis[89,90], solid-state reaction[91,92], and combustion synthesis[93]. These methods can be tuned to give microparticles, which are usually of high polydispersity and not well attached to any substrate. These powders are then pressed into pellets or otherwise modified to hold a particular shape using binder additives. These techniques are not able to give uniform thin layers of yttrium borate micropowders evenly coating a substrate. Walker, et al., found that the penetration depth for ionizing radiation was on the order of 15 to 20 µm, while light for photoluminescence (PL) measurements typically penetrate on the order of 100 µm.[86] For more information on photoluminescence measurements see Chapter 1 page 10. Since typical samples are pressed into pellets that are millimeters thick, most of the PL signal is generated by powder unaffected by ionizing radiation, which skews the effect to be measured.

Utilizing a new synthesis strategy devised in the Lukehart lab, namely Confined Plume Chemical Deposition (CPCD)[16], thin films of yttrium borate micropowder can be synthesized to improve radiation damage measurements. The materials for radiation damage measurements are usually modified with binder after synthesis, which requires more material to achieve strong luminescence. Synthesis also typically takes a long time. CPCD can produce materials quickly (ca. 15 minutes) and directly in the area of application without any additional binders. Using a laser, it is possible to decompose precursors to desired products with controlled thickness and overall size. For CPCD, the laser must be tuned to some absorption present in the precursor. The energy absorbed by the precursor then atomizes, and possibly even ionizes, atomic constituents. The plume that has been generated then rapidly cools, and the heaviest most stable phases are deposited on the substrate. CPCD nucleates and grows desired products directly from the substrate with relatively even coating, but minimal substrate damage.

Experimental

Reagents and General Methodologies Europium nitrate hexahydrate and cerium nitrate hexahydrate were purchased from Strem and used as received. Decaborane was purchased from Alfa Aesar and used as received. Yttrium nitrate was purchased from Johnson Matthey Catalog Company and used as received. Approximately 1.5 in × 1 in rectangular glass supports were cut from microscope slides as needed. A custom aluminum holder was cut at Vanderbilt in the machine shop and used as the sample holder for CPCD experiments. A 1 in × 1 in × 1 mm ultrahigh molecular weight polyethylene (UHMWPE) spacer with a 1 cm × 1 cm hole was cut.

Powder X-ray diffraction scans were obtained on a Scintag X1 θ/θ automated powder X-ray diffractometer with a Cu target, a Peltier-cooled solid-state detector, and a zero-background Si(510) sample support and UHMW-PE spacers. SEM images were obtained on a Hitachi S-2400 electron microscope with an accelerating voltage of 10 kV to 20 kV.

Confined Plume Chemical Deposition Processing Microsecond IR pulses are produced by a erbium doped yttrium aluminum garnet (Er:YAG) crystal pumped by

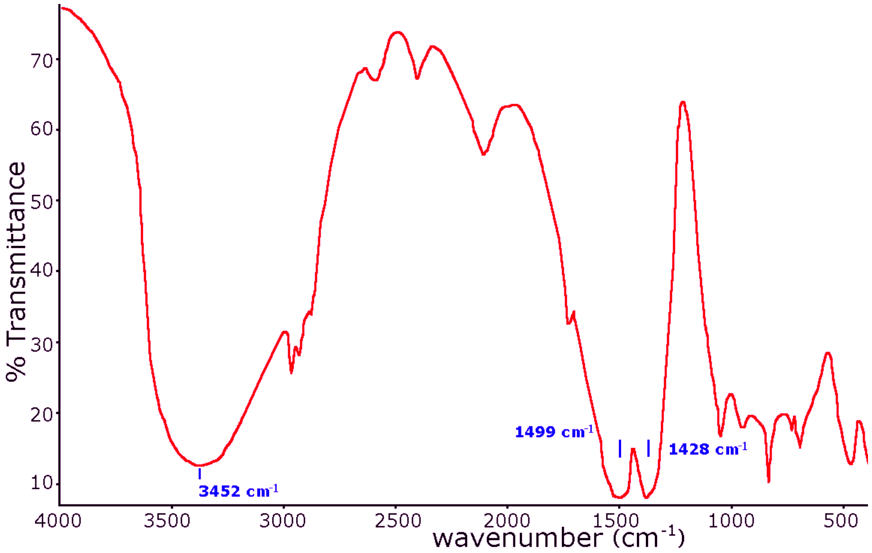

Figure 38: IR spectrum of $Y[O_2CN(H)Pr]_3$, the N-propyl carbamate of yttrium. The N-H stretching at $3452\,\mathrm{cm}^{-1}$ and $N\text{-}CO_2$ stretch at $1499\,\mathrm{cm}^{-1}$ and $1428\,\mathrm{cm}^{-1}$ are marked in the spectrum.

a Xe flash lamp at a fundamental wavelength of 2.94 µm. The pulse energy can be tuned between 100 mJ to 300 mJ with a repetition rate between 10 Hz to 30 Hz. For these experiments the repetition rate was kept constant at 10 Hz and the energy was between 250 mJ to 300 mJ. The laser beam is focused to about a 1 mm circle. This gives a peak power density of about $2.5 \times 10^5\,\mathrm{W\,cm^{-2}}$. For a precursor to absorb 2.94 µm, it must absorb energy around $3400\,\mathrm{cm}^{-1}$. This energy corresponds to vibrations in secondary amines or a hydroxyl group. To attempt a yttrium molecule with a primary amine, for the 2.94 µm laser, a new precursor was synthesized. Yttrium tris(N-propyl-carbamate) has good absorbance in the $3400\,\mathrm{cm}^{-1}$ range, see Figure 38. The band near $3400\,\mathrm{cm}^{-1}$ is due to the N-H vibration in the molecule; and the two bands at $1499\,\mathrm{cm}^{-1}$ and $1428\,\mathrm{cm}^{-1}$ are from C-O stretching bands in the $N\text{-}CO_2$ part of the molecule. All other bands are from the propyl side-chain (either C-H or N-C vibrations and motions).

To produce YBO_3, yttrium tris(N-propyl-carbamate) was mixed with decaborane such that boron was in a five times atomic excess to yttrium. This carbamate precur-

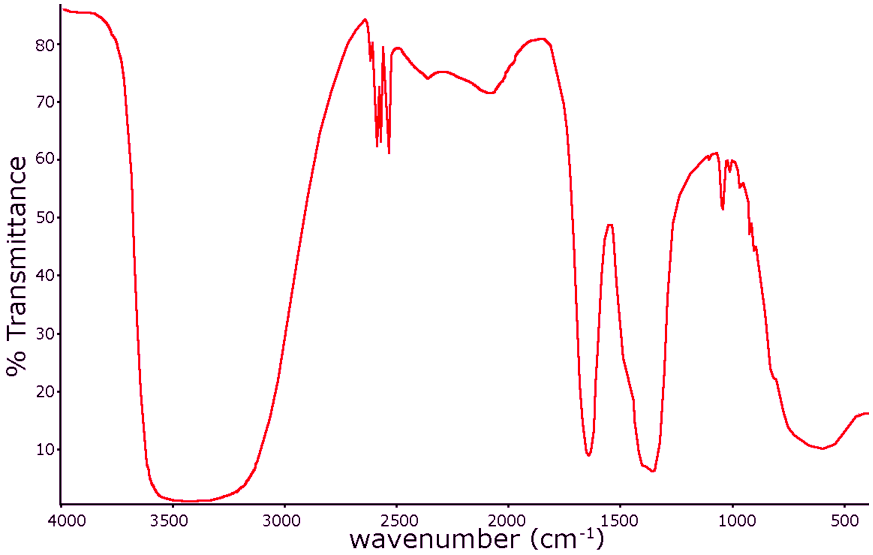

Figure 39: IR spectrum of $Y(NO_3)_3 \cdot H_2O$ mixed with $B_{10}H_{14}$ and $Ce(NO_3)_3 \cdot H_2O$. Strong absorption near $3400\,\mathrm{cm}^{-1}$ is obvious, and the peaks around $1500\,\mathrm{cm}^{-1}$ are from $[NO_3]^-$ vibration.

sor has good absorbance of the IR laser, giving a strong plume; however, XRD shows phase separation into yttria and borate and the powder is dark from carbon incorporation. Optimal conditions for CPCD of yttrium tris(N-propyl-carbamate) proved difficult to elucidate, so a different precursor was sought. Most likely the size of the N-propyl-carbamate ligand did not allow adequate mixing of the Y and B to form YBO_3, so phase separation is seen. The IR spectrum of yttrium nitrate hexahydrate showed strong absorbance around $3400\,\mathrm{cm}^{-1}$ as well, most likely due to the waters of crystallization, see Figure 39. This was also mixed with decaborane to give a five times atomic excess of boron to yttrium. This mixture plumed well under CPCD conditions, and gave a colorless powder that showed YBO_3 by XRD.

The final consideration is to add a lanthanide dopant without affecting the reaction too much. First cerium nitrate was added to yttrium nitrate and decaborane in an acetone solution; however, a reaction appears to occur as a yellow color develops in the initially colorless solution as acetone evaporates. Also after CPCD of the dried solid, phase separation was again an issue as determined by XRD. The product of mixing cerium nitrate, yttrum nitrate, and decaborane in a solvent was not further characterized. To achieve the desired YBO_3:Ln final material, the powders of cerium nitrate, yttrium nitrate, and decaborane were ground in a mortar and pestle to mix and grind into a fine powder. Then using a spacer cut out of a sheet of ultrahigh molecular weight polyethylene (UHMWPE) to help confine the powder, CPCD was attempted again. XRD shows YBO_3 as the primary phase with a small amount of B_2O_3, see Figure 41.

Results and Discussion

Yittrium nitrate mixed with decaborane and cerium nitrate in an acetone solution gives a yellow substance that, after being processed under CPCD conditions, affords a mixture of phases. YBO_3, Y_2O_3, and B_2O_3 are all present in the XRD pattern, see Figure 40. From relative peak areas, relative amounts can be estimated. Without further correction, only approximate amounts can be estimated. From Figure 40, B_2O_3 is the dominant phase followed by Y_2O_3, and YBO_3 only appears a small impurity. This likely means that whatever reaction takes place to turn the powder yellow also keeps the $Y(NO_3)_3$ from mixing well with $B_{10}H_{14}$. However, when the powders were mixed in a mortar and pestle, YBO_3 became the dominant phase, see Figure 41.

Europium-doped YBO_3 is also of interest for this project, since Eu has a strong photoluminescence (PL) signal from within an YBO_3 matrix. To synthesize YBO_3:Eu, yttrium nitrate, decarborane, and europium nitrate were mixed in a mortar and pestle. This powder mixture was then confined between two glass substrates with a UHMWPE spacer and subjected to CPCD processing. XRD of the final material also shows YBO_3 as the dominant phase, see Figure 42.

Since the XRD pattern confirms reasonably pure YBO_3, the samples were analyzed for photoluminescence (PL). To find the optimal cerium doping level, samples with

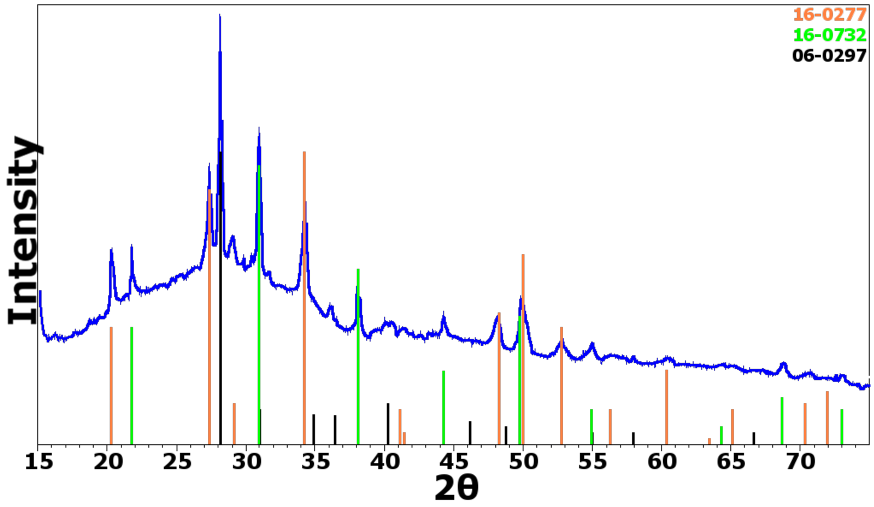

Figure 40: XRD pattern of the product from mixing $Y(NO_3)_3$, $B_{10}H_{14}$, and $Ce(NO_3)_3$ in acetone, allowing it to dry, then processing it in CPCD conditions. The red lines correspond to the line pattern for YBO_3 (PDF# 16-0277), the green lines correspond to Y_2O_3 (PDF#16-0732), and the black lines correspond to B_2O_3 (PDF# 06-0297).

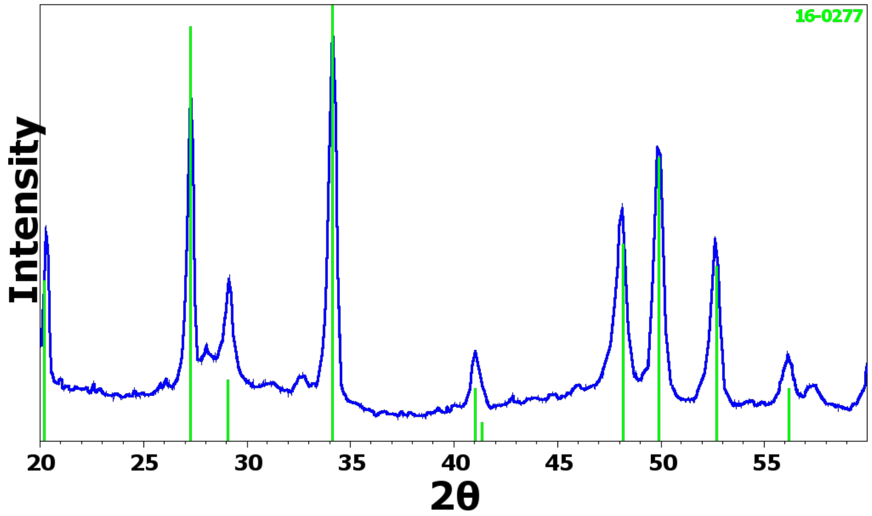

Figure 41: XRD pattern of the product from mixing $Y(NO_3)_3$, $B_{10}H_{14}$, and $Ce(NO_3)_3$ by mortar and pestle and processing under optimized CPCD conditions. The green lines correspond to YBO_3 (PDF# 16-0277).

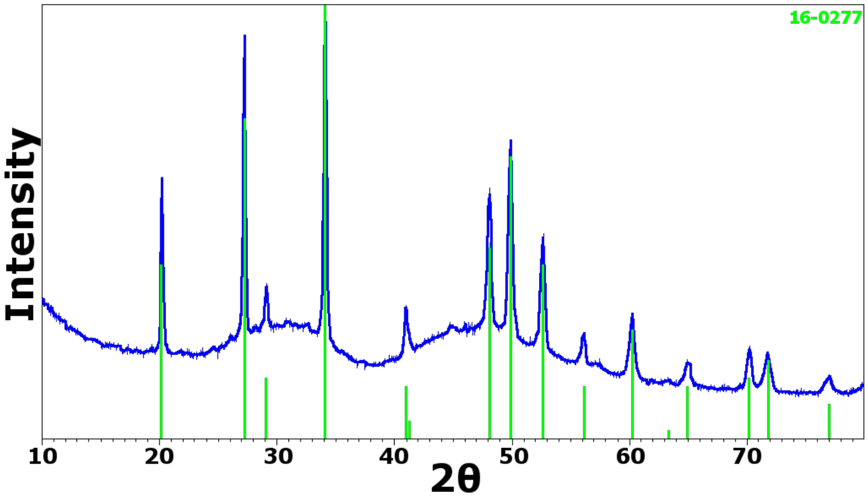

Figure 42: XRD pattern of the product from CPCD of $Y(NO_3)_3$, $B_{10}H_{14}$, and $Eu(NO_3)_3$ mixed by mortar and pestle. the green lines correspond to YBO_3 (PDF# 16-0277).

5 atomic percent (at%), 10 atomic percent (at%) and 20 atomic percent (at%) doping were mixed and processed under CPCD conditions. PL measurements show that approximately 5-10 at% doping is optimal for YBO_3:Ce, see Figure 43. Cerium has characteristic emission peaks at about 390 nm and 415 nm, corresponding to $^5D_0 \rightarrow {}^2F_{2/5}$ and $^5D_0 \rightarrow {}^7F_{2/7}$ transitions respectively.[94] Emission signal increases in intensity with increasing doping level until concentration quenching dominates and signal intensity decreases.[95] In traditional solid-state reactions, optimal cerium doping is around 3 at% to 5 at%.[96] Further investigation is needed to confirm that the doping amount used is the amount actually present in the final powders.

Since Eu has a much higher intensity PL response than Ce, doping of YBO_3 with Eu was also attempted by CPCD. To find the optimal europium doping level, samples with 15 at%, 30 at% and 45 at% doping were mixed and processed under CPCD conditions. PL measurements show that about 30 at% doping is optimal for YBO_3:Eu, see Figure 44. Europium has characteristic emission peaks at about 595 nm, 615 nm and 627 nm corresponding to $^5D_0 \rightarrow {}^7F_1$(595 nm) and $^5D_0 \rightarrow {}^7F_2$(615 nm and 627 nm) transitions. In traditional solid-state reactions, optimal europium doping is around

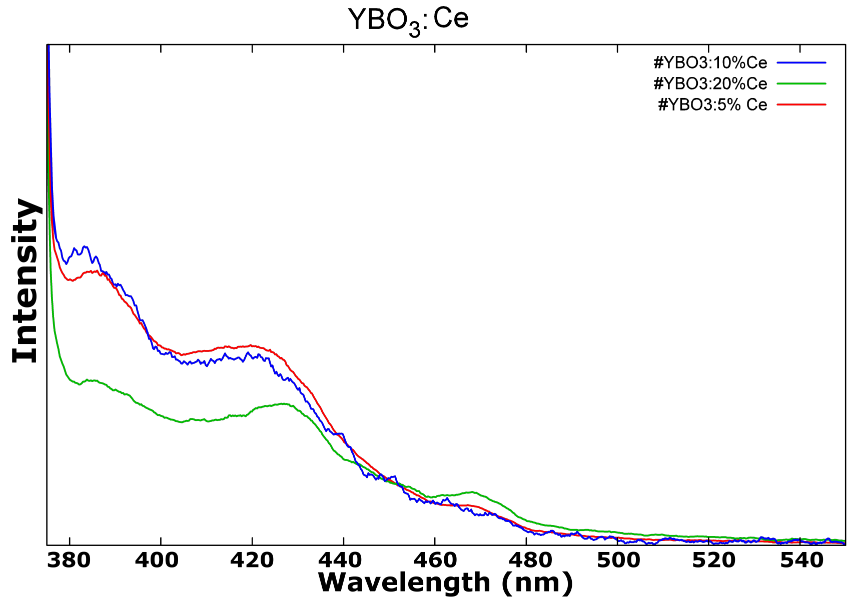

Figure 43: Photoluminescence measurements of YBO_3:Ce at 5 at%, 10 at% and 15 at% doping. The characteristic peaks at 395 nm and 415 nm are clearly visible. Optimal doping was found to be around 5 at% to 10 at%.

30 at%.[97] More experiments are needed between 30 at% to 45 at% doping to find the exact optimal doping level.

To test if the actual doping levels corresponded to the theoretical doping levels, SEM-EDS was performed over several particles. The averages of these particles for a sample of 40 at% Eu in YBO_3 and 42.5 at% Eu in YBO_3 were analyzed, see Tables 2 and 3 respectively. The relative atomic percents match within experimental error with the expected stoichiometry, with 33 at% Eu in $Y_{0.77}B_{0.91}O_{3.0}$ for the sample with a theoretical stoichiometry of $Y_{0.6}B_1O_3$:$Eu_{0.40}$ and 42 at% Eu in $Y_{0.58}B_{0.73}O_{2.3}$ for the sample a theoretical stoichiometry of $Y_{0.575}B_1O_3$:$Eu_{0.425}$. Analyzing heavy elements like europium is traditionally very difficult with SEM-EDS but the analysis indicates that most likely all the theoretical europium gets incorporated in the yttrium borate during synthesis by CPCD.

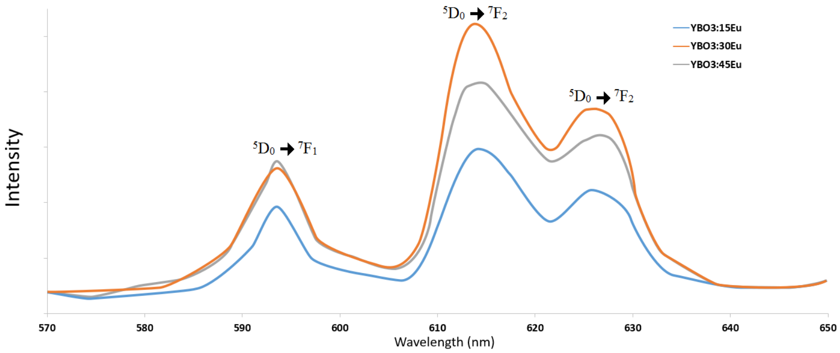

Figure 44: Photoluminescence measurements of YBO_3:Eu at 15 at%, 30 at% and 45 at% doping. The characteristic peaks at 595 nm, 615 nm and 627 nm are clearly visible. Optimal doping was found to be about 30 at%.

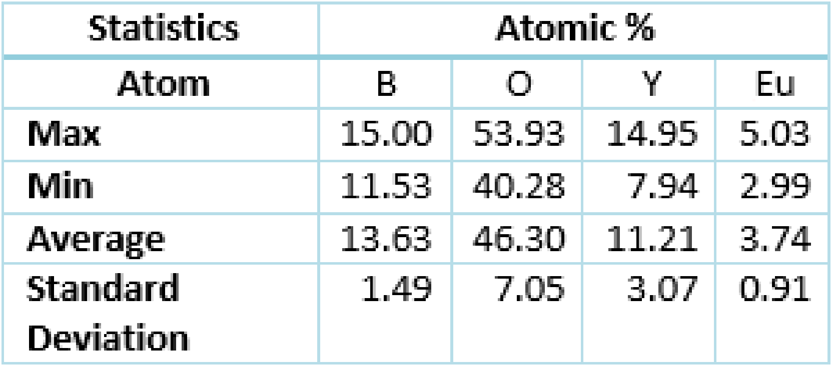

Statistics	Atomic %			
Atom	B	O	Y	Eu
Max	15.00	53.93	14.95	5.03
Min	11.53	40.28	7.94	2.99
Average	13.63	46.30	11.21	3.74
Standard Deviation	1.49	7.05	3.07	0.91

Table 2: Summary statistics from several particles of 40 at% doped YBO_3:Eu. These percents match well with the theoretical doping, see text for discussion.

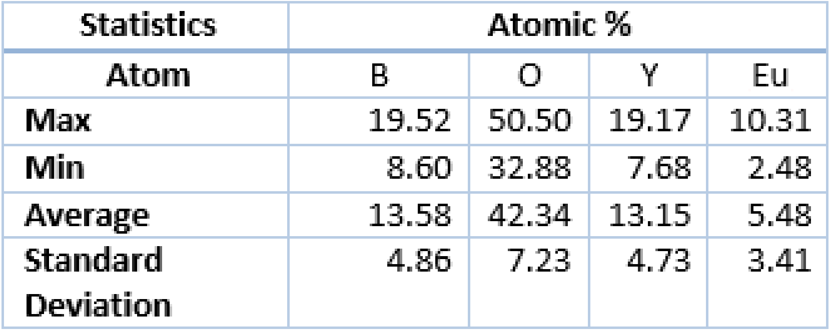

Statistics	Atomic %			
Atom	B	O	Y	Eu
Max	19.52	50.50	19.17	10.31
Min	8.60	32.88	7.68	2.48
Average	13.58	42.34	13.15	5.48
Standard Deviation	4.86	7.23	4.73	3.41

Table 3: Summary statistics from several particles of 42.5 at% doped YBO_3:Eu. These percents match well with the theoretical doping, see text for discussion.

Conclusions

Confined Plume Chemical Deposition has been shown to successfully synthesize lanthanide-doped yttrium borate powders. Optimal doping for europium-doped yttrium borate was found to be 30 at% and for cerium-doped yttrium borate was found to be between 5 at% to 10 at%. The optimal doping appears to be a little higher than literature values, but it may be because not all of the dopant gets incorporated. In order to form YBO_3 powder a 5 to 1 boron to yttrium ratio is necessary, which further supports the theory that not all dopant atoms get incorporated. Further investigation is needed to confirm the actual doping in the yttrium borate powders and more precisely what doping level is optimal utilizing CPCD.

APPENDIX B

LASER-BEAM SHAPING THROUGH SHADOW MASKING AND CYLINDRICAL OPTICS

General Introduction

Confined-Plume Chemical Deposition (CPCD) is strongly dependent on the shape of the laser beam being utilized. Beam shaping is the process of redistributing the irradiance of a beam. The beam intensity profile is usually either Gaussian or flattop. The native beam emitted by a laser is usually Gaussian, so the objective is to shape the beam to a flattop profile. CPCD is dependent on the intensity of the laser striking the sample. Currently a spherical focusing optic gives the best results, as intensity is focused to a small area and the plume is of uniform temperature. However, the rate of product formation could be greatly increased if a cylindrical focus was utilized.

A Gaussian beam focused through cylindrical optics gives an elliptical Gaussian beam with the irradiance highest in the center of the beam and dropping off in a shallow exponential in one axis and in a steep exponential in the perpendicular axis. This means that under CPCD conditions, the temperature in the plume will be highest in the center and follow the exponential curves; however, this is undesirable as the exact mechanism of plume formation is unknown, so nonuniform temperatures only complicates processing outcomes. To achieve uniform temperatures over a wide area, a flattop beam profile is desirable.

Experimental

Equipment The beam mask was cut from a piece of silicon from Sigma Aldrich. Femtosecond UV pulses are produced in an amplified titanium-sapphire (Ti:sapphire)-based laser system operating at a fundamental wavelength of 795 nm. A continuous wave (cw) pumped mode-locked Ti:sapphire oscillator, producing <100 fs pulse widths at a repetition rate of 82 MHz, is used to seed the Ti:sapphire amplifier which increases the energy of the femtosecond pulses to ca. 1 mJ/pulse in a regenerative and linear double-pass amplifier arrangement while maintaining pulse widths of ca. 150 fs. This gives a peak power of 6.6 GW. This is focused through either a cylindrical optics into a line of approximately 400 µm by 6 mm, giving a peak intensity of $2.7\,\mathrm{TW\,cm^{-2}}$, or a spherical optic into a spot of approximately 0.5 mm, giving a peak intensity of $130\,\mathrm{GW\,cm^{-2}}$.

Methodologies To measure the irradiance profile, knife-edge measurements were utilized. A razor blade was set up on an x,y-stage and scanned across the laser beam while measuring the total energy. By measuring both the x and y axis from full energy to no energy, a profile of the laser beam can be generated. Then using this profile, a beam mask can be calculated that after cylindrical focusing gives a flattop beam profile. This mask was cut out of a piece of silicon using the UV laser focused to a spot through the spherical focus.

Results and Discussion

Using a razor blade, knife-edge measurements of the laser beam were made, see Figure 45. Knife-edge measurements were also made of the beam after cylindrical focusing to an elliptical Gaussian, see Figure 46. Then a mask shape was calculated that could be integrated along one axis to give a flattop profile, see Figures 47 and 48. This shape was then cut into a piece of silicon using a LabView program to control the x,y-stage. The code for this program is in Figure 49 and Figure 50. Knife-edge measurements of the final beam measured along the long axis show improved shape, but not completely flattop, see Figure 51. More work is needed to align the beam mask to the cylindrical focus optics better and a better beam profile measurement system is needed; with these improvements better masks could be designed and utilized to achieve a more flattop profile.

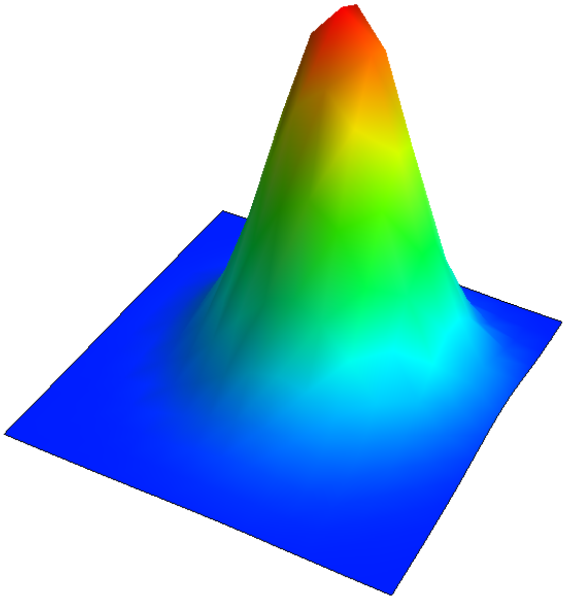

Figure 45: Gaussian beam of the 795-nm laser. Fitting the total irradiance data to the cumulative distribution function, a Gaussian function was generated. The x-Gaussian and y-Gaussian were then combined to give a three-dimensional beam profile.

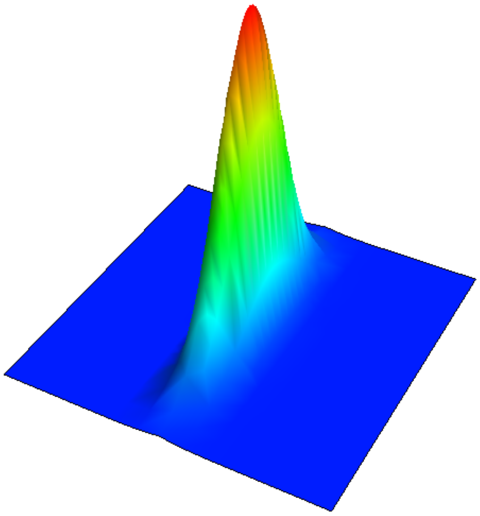

Figure 46: Elliptical Gaussian beam profile of the 795-nm laser after cylindrical focusing. The long axis was measured irradiance, but the short axis is simulated based on visual estimation.

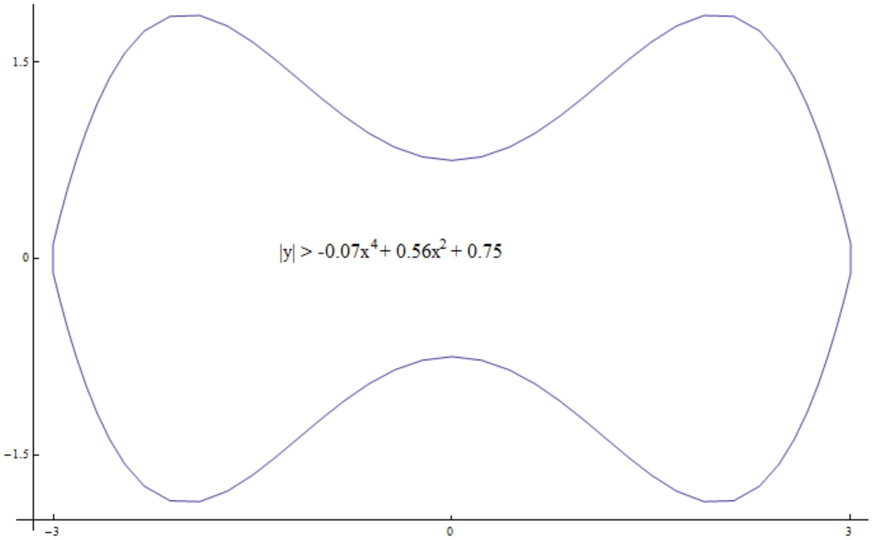

Figure 47: The formula and shape of the mask to transform a Gaussian beam into a flattop after a cylindrial focus optics.

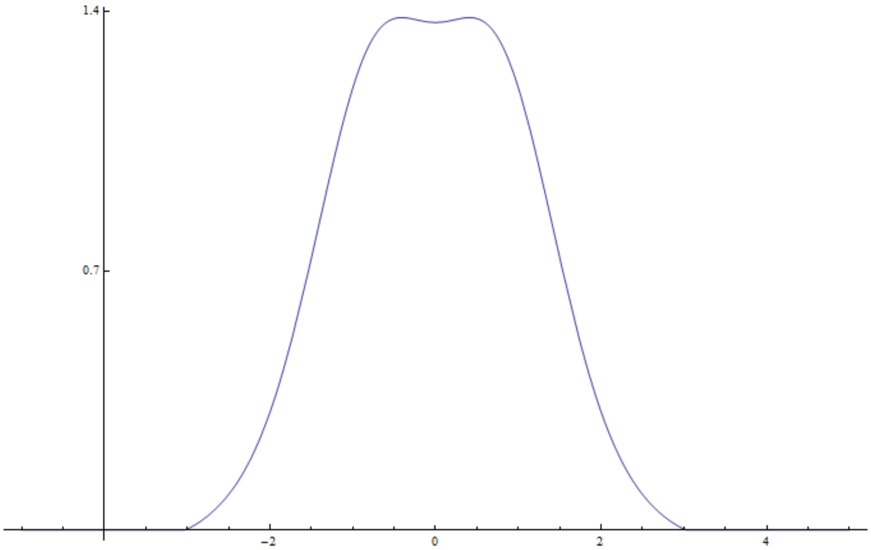

Figure 48: Calculated line profile of the laser beam after the mask and integration in one direction.

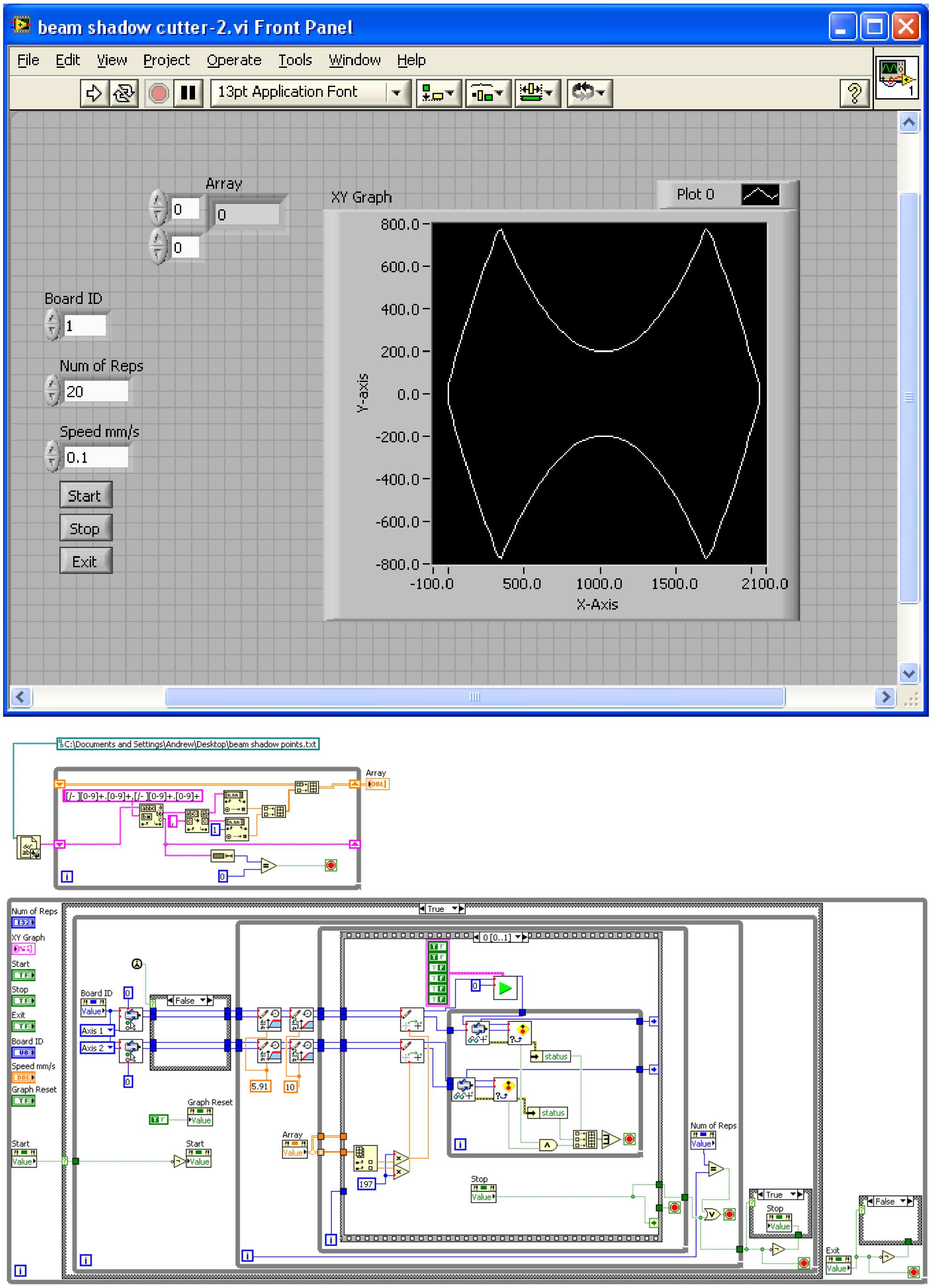

beam shadow cutter-2.vi Front Panel

Array: 0 0 0

Board ID: 1

Num of Reps: 20

Speed mm/s: 0.1

Figure 49: Pictures of the LabView code used to cut the mask shape into a piece of silicon.

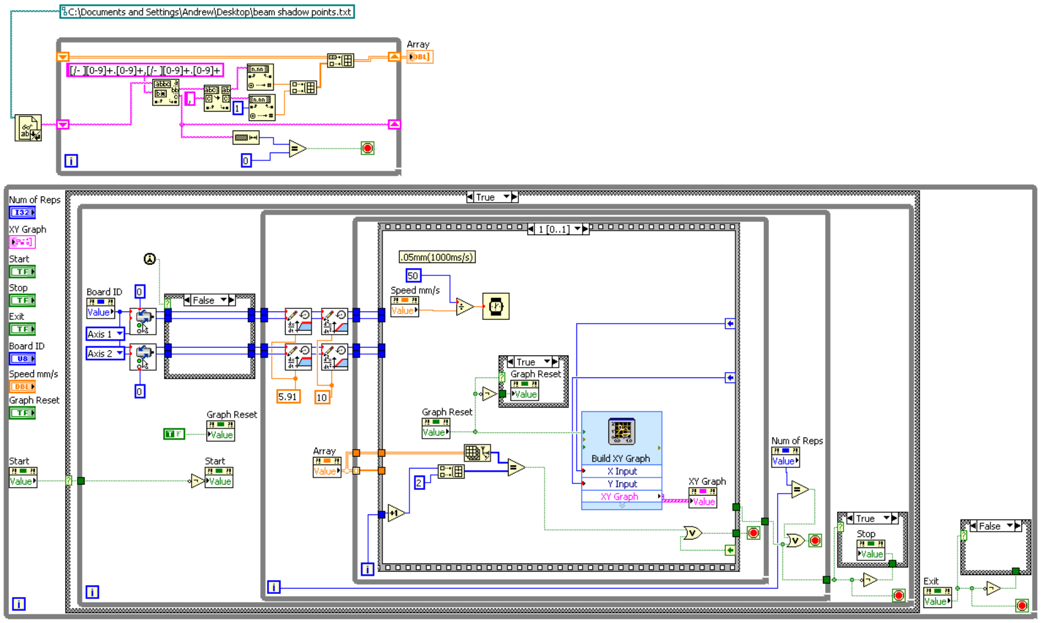

Figure 50: Continuing pictures of the LabView code used to cut the mask shape into a piece of silicon.

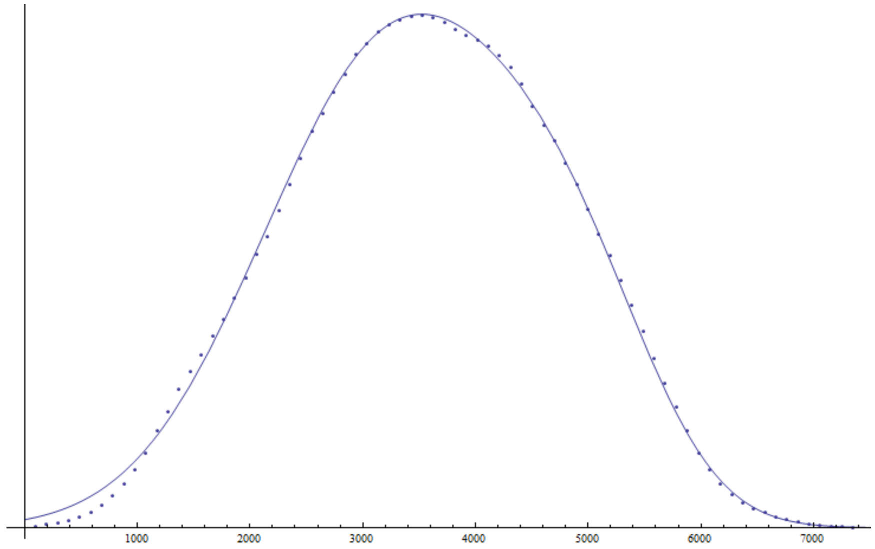

Figure 51: Gaussian profile fitting knife-edge measurements of the final beam after mask and cylindrical focus. The total irradiance data was fit with a cumulative distribution function to generate the parameters of a Gaussian profile.

Conclusions

Progress was made toward improving CPCD by utilizing a flattop line-focused beam. While the masked, cylindrically focused beam was not exactly flattop, it was much less Gaussian than initially emitted. With more uniform beam irradiance, CPCD can be performed more uniformly and more easily. Using LabView, any shape can be cut by modifying the formula controlling stage movement.

Bibliography

(1) Science and Public Policy Commission, C. o. t. S. o. M. S. . E., *Materials and Man's Needs: Materials Science and Engineering*; National Academies Press: Washington, DC, USA, 1974.

(2) Krlik, M.; Biffis, A. Catalysis by metal nanoparticles supported on functional organic polymers. *Journal of Molecular Catalysis A: Chemical* **Dec. 2001**, *177*, 113–138.

(3) Steigerwalt, E. S.; Deluga, G. A.; Lukehart, C. M. PtRu/Carbon Fiber Nanocomposites: Synthesis, Characterization, and Performance as Anode Catalysts of Direct Methanol Fuel Cells. A Search for Exceptional Performance. *The Journal of Physical Chemistry B* **Jan. 2002**, *106*, 760–766.

(4) Yan, C.; Wagner, M. J. Air- and Water-Stable Gold-Coated Gadolinium Metal Nanocrystals. *Nano Lett.* **June 2013**, *13*, 2611–2614.

(5) Wang, C.; Daimon, H.; Onodera, T.; Koda, T.; Sun, S. A General Approach to the Size- and Shape-Controlled Synthesis of Platinum Nanoparticles and Their Catalytic Reduction of Oxygen. *Angewandte Chemie International Edition* **Apr. 2008**, *47*, 3588–3591.

(6) Wigen, P. E.; Roukes, M. L.; Hammel, P. C. In *Spin Dynamics in Confined Magnetic Structures III*, Hillebrands, B., Thiaville, A., Eds.; Topics in Applied Physics 101, DOI: 10.1007/10938171_3; Springer Berlin Heidelberg: 2006, pp 105–136.

(7) Sanchez, C.; Rozes, L.; Ribot, F.; Laberty-Robert, C.; Grosso, D.; Sassoye, C.; Boissiere, C.; Nicole, L. Chimie douce: A land of opportunities for the designed construction of functional inorganic and hybrid organic-inorganic nanomaterials. *Comptes Rendus Chimie* **Jan. 2010**, *13*, 3–39.

(8) Yoshimura, M. Soft solution processing: concept and realization of direct fabrication of shaped ceramics (nano-crystals, whiskers, films, and/or patterns) in solutions without post-firing. *J Mater Sci* **Mar. 2006**, *41*, 1299–1306.

(9) Fendler, J. H. Colloid chemical approach to nanotechnology. *Korean J. Chem. Eng.* **Jan. 2001**, *18*, 1–13.

(10) Thangadurai, V; Knittlmayer, C; Weppner, W Metathetic room temperature preparation and characterization of scheelite-type ABO4 (A = Ca, Sr, Ba, Pb; B = Mo, W) powders. *Materials Science and Engineering: B* **Feb. 2004**, *106*, 228–233.

(11) Livage, J. Chimie douce: from shake-and-bake processing to wet chemistry. *New J. Chem.* **Jan. 2001**, *25*, 1–1.

(12) West, A. R., *Solid State Chemistry and Its Applications*; Wiley: Chichester, Dec. 1987.

(13) Adam, D. Microwave chemistry: Out of the kitchen. *Nature* **Feb. 2003**, *421*, 571–572.

(14) Bilecka, I.; Niederberger, M. Microwave chemistry for inorganic nanomaterials synthesis. *Nanoscale* **Aug. 2010**, *2*, 1358–1374.

(15) Bond, G.; Moyes, R. B.; Whan, D. A. Recent applications of microwave heating in catalysis. *Catalysis Today* **Oct. 1993**, *17*, 427–437.

(16) Ivanov, B. L.; Wellons, M. S.; Lukehart, C. M. Confined-Plume Chemical Deposition: Rapid Synthesis of Crystalline Coatings of Known Hard or Superhard Materials on Inorganic or Organic Supports by Resonant IR Decomposition of Molecular Precursors. *J. Am. Chem. Soc.* **Aug. 2009**, *131*, 11744–11750.

(17) Connelly, N. G.; Geiger, W. E. Chemical Redox Agents for Organometallic Chemistry. *Chem. Rev.* **Jan. 1996**, *96*, 877–910.

(18) In *CRC Handbook of Chemistry and Physics, 95th Edition*, Haynes, W. M., Ed., 95 edition; CRC Press: Boca Raton, Fla., June 2014.

(19) Parr, R. G. Density Functional Theory. *Annual Review of Physical Chemistry* **1983**, *34*, 631–656.

(20) *Characterization of Nanophase Materials*; Wang, Z. L., Ed.; Wiley-VCH Verlag GmbH: Weinheim Germany, 1999.

(21) Perdew, J. P.; Burke, K.; Ernzerhof, M. Generalized Gradient Approximation Made Simple. *Phys. Rev. Lett.* **Oct. 1996**, *77*, 3865–3868.

(22) Vanderbilt, D. Soft self-consistent pseudopotentials in a generalized eigenvalue formalism. *Phys. Rev. B* **Apr. 1990**, *41*, 7892–7895.

(23) Hardy, R. J.; Binek, C., *Thermodynamics and Statistical Mechanics: An Integrated Approach*, 1 edition; Wiley: Chichester, West Sussex, June 2014.

(24) Steele, B. C. H.; Heinzel, A. Materials for fuel-cell technologies. *Nature* **Nov. 2001**, *414*, 345–352.

(25) Bashyam, R.; Zelenay, P. A class of non-precious metal composite catalysts for fuel cells. *Nature* **Sept. 2006**, *443*, 63–66.

(26) Watanabe, M.; Motoo, S. Electrocatalysis by ad-atoms: Part II. Enhancement of the oxidation of methanol on platinum by ruthenium ad-atoms. *Journal of Electroanalytical Chemistry and Interfacial Electrochemistry* **Apr. 1975**, *60*, 267–273.

(27) Oetjen, H.-F.; Schmidt, V. M.; Stimming, U.; Trila, F. Performance Data of a Proton Exchange Membrane Fuel Cell Using H_2 / CO as Fuel Gas. *J. Electrochem. Soc.* **Dec. 1996**, *143*, 3838–3842.

(28) Christoffersen, E; Liu, P; Ruban, A; Skriver, H. L; Nrskov, J. K Anode Materials for Low-Temperature Fuel Cells: A Density Functional Theory Study. *Journal of Catalysis* **Apr. 2001**, *199*, 123–131.

(29) Tritsaris, G. A.; Rossmeisl, J. Methanol Oxidation on Model Elemental and Bimetallic Transition Metal Surfaces. *J. Phys. Chem. C* **June 2012**, *116*, 11980–11986.

(30) Steigerwalt, E. S.; Deluga, G. A.; Cliffel, D. E.; Lukehart, C. M. A PtRu/Graphitic Carbon Nanofiber Nanocomposite Exhibiting High Relative Performance as a Direct-Methanol Fuel Cell Anode Catalyst. *The Journal of Physical Chemistry B* **Aug. 2001**, *105*, 8097–8101.

(31) Endo, M.; Kim, Y. A.; Ezaka, M.; Osada, K.; Yanagisawa, T.; Hayashi, T.; Terrones, M.; Dresselhaus, M. S. Selective and Efficient Impregnation of Metal Nanoparticles on Cup-Stacked-Type Carbon Nanofibers. *Nano Lett.* **June 2003**, *3*, 723–726.

(32) Kleis, J.; Greeley, J.; Romero, N. A.; Morozov, V. A.; Falsig, H.; Larsen, A. H.; Lu, J.; Mortensen, J. J.; Duak, M.; Thygesen, K. S.; Nrskov, J. K.; Jacobsen, K. W. Finite Size Effects in Chemical Bonding: From Small Clusters to Solids. *Catal Lett* **June 2011**, *141*, 1067–1071.

(33) Pehlke, E.; Scheffler, M. Evidence for site-sensitive screening of core holes at the Si and Ge (001) surface. *Phys. Rev. Lett.* **Oct. 1993**, *71*, 2338–2341.

(34) Mtensson, N.; Nilsson, A. On the origin of core-level binding energy shifts. *Journal of Electron Spectroscopy and Related Phenomena* **Dec. 1995**, *75*, 209–223.

(35) Krling, M.; Hglund, J. Cohesive and electronic properties of transition metals: The generalized gradient approximation. *Phys. Rev. B* **June 1992**, *45*, 13293–13297.

(36) Radmilovic, V.; Gasteiger, H. A.; Ross, P. N. Structure and Chemical Composition of a Supported Pt-Ru Electrocatalyst for Methanol Oxidation. *Journal of Catalysis* **June 1995**, *154*, 98–106.

(37) Antolini, E.; Giorgi, L.; Cardellini, F.; Passalacqua, E. Physical and morphological characteristics and electrochemical behaviour in PEM fuel cells of PtRu /C catalysts. *J Solid State Electrochem* **Feb. 2001**, *5*, 131–140.

(38) Ekioglu, B.; Nadarajah, A. Structural analysis of conical carbon nanofibers. *Carbon* **Feb. 2006**, *44*, 360–373.

(39) Jiang, D.-e.; Du, M.-H.; Dai, S. First principles study of the graphene/Ru(0001) interface. *The Journal of Chemical Physics* **Feb. 2009**, *130*, 074705.

(40) Zhu, Y. A.; Sui, Z. J.; Zhao, T. J.; Dai, Y. C.; Cheng, Z. M.; Yuan, W. K. Modeling of fishbone-type carbon nanofibers: A theoretical study. *Carbon* **July 2005**, *43*, 1694–1699.

(41) Tsong, T. T.; Ren, D. M.; Ahmad, M. Atomic-layer by atomic-layer compositional depth profiling: Surface segregation and impurity cosegregation of Pt-Rh and Pt-Ru alloys. *Phys. Rev. B* **Oct. 1988**, *38*, 7428–7435.

(42) Walle, L. E.; Grnbeck, H.; Fernandes, V. R.; Blomberg, S.; Farstad, M. H.; Schulte, K.; Gustafson, J.; Andersen, J. N.; Lundgren, E.; Borg, A. *Surf. Sci.* **2012**, *23/24*, 1777.

(43) Henkelman, G.; Arnaldsson, A.; Jnsson, H. A fast and robust algorithm for Bader decomposition of charge density. *Computational Materials Science* **June 2006**, *36*, 354–360.

(44) Siegbahn, K. Electron spectroscopy for atoms, molecules, and condensed matter. *Rev. Mod. Phys.* **July 1982**, *54*, 709–728.

(45) Chaudhuri, A.; Lerotholi, T. J.; Jackson, D. C.; Woodruff, D. P.; Dhanak, V. Local Methylthiolate Adsorption Geometry on Au(111) from Photoemission Core-Level Shifts. *Phys. Rev. Lett.* **Mar. 2009**, *102*, 126101.

(46) Grnbeck, H.; Odelius, M. Photoemission core-level shifts reveal the thiolate-Au(111) interface. *Phys. Rev. B* **Aug. 2010**, *82*, 085416.

(47) Bjrneholm, O.; Nilsson, A.; Tillborg, H.; Bennich, P.; Sandell, A.; Hernns, B.; Puglia, C.; Mrtensson, N. Overlayer structure from adsorbate and substrate core level binding energy shifts: CO, CCH3 and O on Pt(111). *Surface Science* **Aug. 1994**, *315*, L983–L989.

(48) Weststrate, C. J.; Baraldi, A.; Rumiz, L.; Lizzit, S.; Comelli, G.; Rosei, R. A surface core-level shift study of hydrogen interaction with Rh(111). *Surface Science* **Sept. 2004**, *566568, Part 1*, 486–491.

(49) Beard, J. D.; Aleksandrov, S.; Walker, C. H.; Wolverson, D.; Mitchels, J. M.; Gordeev, S. N. Magnetically enhanced plasma coating of nanostructures with ultrathin diamond-like carbon films. *RSC Adv.* **June 2014**, *4*, 26635–26644.

(50) Chua, D. H. C.; Teo, K. B. K; Tsai, T. H; Milne, W. I; Sheeja, D; Tay, B. K; Schneider, D Correlation of surface, mechanical and microproperties of tetrahedral amorphous carbon films deposited under different magnetic confinement conditions. *Appl. Surf. Sci.* **Jan. 2004**, *221*, 455–466.

(51) Lu, F. X.; Zhong, G. F.; Sun, J. G.; Fu, Y. L.; Tang, W. Z.; Wang, J. J.; Li, G. H.; Zang, J. M.; Pan, C. H.; Tang, C. X.; Lo, T. L.; Zhang, Y. G. A new type of DC arc plasma torch for low cost large area diamond deposition. *Diamond Relat. Mater.* **June 1998**, *7*, 737–741.

(52) Ohtsu, Y.; Tsurume, Y.; Fujita, H. A new sputtering device of radio-frequency magnetron discharge using a rectangular hollow-shaped electrode. *Rev. Sci. Instr.* **Apr. 1998**, *69*, 1833–1836.

(53) Bohlmark, J.; stbye, M.; Lattemann, M.; Ljungcrantz, H.; Rosell, T.; Helmersson, U. Guiding the deposition flux in an ionized magnetron discharge. *Thin Solid Films* **Dec. 2006**, *515*, 1928–1931.

(54) Butt, M. Z.; Ali, D.; Ahmad, F. Pulsed laser deposition and characterization of Alnico5 magnetic films. *Applied Surface Science* **Sept. 2013**, *280*, 975–980.

(55) Vazquez Luna, J. G.; Zehe, A.; Zelaya-Angel, O. Chemical CdS Thin-Film Deposition Influenced by External Electric and Magnetic Fields. *Cryst. Res. Technol.* **Sept. 1999**, *34*, 949–958.

(56) Balela, M. D. L.; Yagi, S.; Matsubara, E. Fabrication of Cobalt Nanowires by Electroless Deposition under External Magnetic Field. *J. Electrochem. Soc.* **Apr. 2011**, *158*, D210–D216.

(57) Wu, M.; Xiong, Y.; Jia, Y.; Niu, H.; Qi, H.; Ye, J.; Chen, Q. Magnetic field-assisted hydrothermal growth of chain-like nanostructure of magnetite. *Chemical Physics Letters* **Jan. 2005**, *401*, 374–379.

(58) Ren, B.; Ruditskiy, A.; Song, J. H. K.; Kretzschmar, I. Assembly Behavior of Iron Oxide-Capped Janus Particles in a Magnetic Field. *Langmuir* **Jan. 2012**, *28*, 1149–1156.

(59) Martinez-Boubeta, C.; Simeonidis, K.; Makridis, A.; Angelakeris, M.; Iglesias, O.; Guardia, P.; Cabot, A.; Yedra, L.; Estrad, S.; Peir, F.; Saghi, Z.; Midgley, P. A.; Conde-Leborn, I.; Serantes, D.; Baldomir, D. Learning from Nature to Improve the Heat Generation of Iron-Oxide Nanoparticles for Magnetic Hyperthermia Applications. *Scientific Reports* **Apr. 2013**, *3*, DOI: `10.1038/srep01652`.

(60) Nkurikiyimfura, I.; Wang, Y.; Pan, Z. Effect of chain-like magnetite nanoparticle aggregates on thermal conductivity of magnetic nanofluid in magnetic field. *Experimental Thermal and Fluid Science* **Jan. 2013**, *44*, 607–612.

(61) Choi, C. J; Tolochko, O; Kim, B. K Preparation of iron nanoparticles by chemical vapor condensation. *Mater. Lett.* **Oct. 2002**, *56*, 289–294.

(62) Karlsson, M. N. A.; Deppert, K.; Wacaser, B. A.; Karlsson, L. S.; Malm, J.-O. Size-controlled nanoparticles by thermal cracking of iron pentacarbonyl. *Appl. Phys. A* **2005**, *80*, 1579–1583.

(63) Liu, D.; Kottke, I.; Adam, D. Localization of cadmium in the root cells of Allium cepa by energy dispersive x-ray analysis. *Biol. Plantarum* **June 2007**, *51*, 363–366.

(64) Gonzalez, M. E.; Barrett, D. M.; McCarthy, M. J.; Vergeldt, F. J.; Gerkema, E.; Matser, A. M.; Van As, H. 1H-NMR Study of the Impact of High Pressure and Thermal Processing on Cell Membrane Integrity of Onions. *J. Food Sci.* **Sept. 2010**, *75*, E417–E425.

(65) Cunha, A. G.; Zhou, Q.; Larsson, P. T.; Berglund, L. A. Topochemical acetylation of cellulose nanopaper structures for biocomposites: mechanisms for reduced water vapour sorption. *Cellulose* **Aug. 2014**, *21*, 2773–2787.

(66) Wu, X.; Lu, C.; Zhou, Z.; Yuan, G.; Xiong, R.; Zhang, X. Green synthesis and formation mechanism of cellulose nanocrystal-supported gold nanoparticles with enhanced catalytic performance. *Environ. Sci. Nano* **2014**, *1*, 71.

(67) Mallikarjuna, N. N.; Varma, R. S. Microwave-Assisted Shape-Controlled Bulk Synthesis of Noble Nanocrystals and Their Catalytic Properties. *Cryst. Growth Des.* **Apr. 2007**, *7*, 686–690.

(68) Tuchscherer, A.; Schaarschmidt, D.; Schulze, S.; Hietschold, M.; Lang, H. Gold nanoparticles generated by thermolysis of all-in-one gold(i) carboxylate complexes. *Dalton Trans.* **2012**, *41*, 2738.

(69) Yamamoto, M.; Nakamoto, M. New Type of Monodispersed Gold Nanoparticles Capped by Myristate and PPh3 Ligands Prepared by Controlled Thermolysis of [Au(C13H27COO)(PPh3)]. *Chemistry Letters* **2003**, *32*, 452–453.

(70) Wan, X.-K.; Lin, Z.-W.; Wang, Q.-M. Au $_{20}$ Nanocluster Protected by Hemilabile Phosphines. *J. Am. Chem. Soc.* **Sept. 2012**, *134*, 14750–14752.

(71) Foos, E. E.; Twigg, M. E.; Snow, A. W.; Ancona, M. G. Competition Between Thiol and Phosphine Ligands During the Synthesis of Au Nanoclusters. *J. Clust. Sci.* **Dec. 2008**, *19*, 573–589.

(72) Suslov, D Cellulose orientation determines mechanical anisotropy in onion epidermis cell walls. *J. Exp. Bot.* **May 2006**, *57*, 2183–2192.

(73) Rugar, D.; Budakian, R.; Mamin, H. J.; Chui, B. W. Single spin detection by magnetic resonance force microscopy. *Nature* **July 2004**, *430*, 329–332.

(74) Sidles, J. A.; Garbini, J. L.; Bruland, K. J.; Rugar, D.; Zger, O.; Hoen, S.; Yannoni, C. S. Magnetic resonance force microscopy. *Rev. Mod. Phys.* **Jan. 1995**, *67*, 249–265.

(75) Yannoni, C. S.; Zger, O.; Rugar, D.; Sidles, J. A. In *Encyclopedia of Nuclear Magnetic Resonance*, D. M. Grant, R. K. Harris, Eds.; Wiley: Chichester, 1996, pp 2093–2100.

(76) Pelekhov, D. V.; Martin, I.; Suter, A.; Reagor, D. W.; Hammel, P. C. In *Quantum Dot Devices and Computing*, ed. by Lott, J. A.; Ledentsov, N. N.; Malloy, K. J.; Kane, B. E.; Sigmon, T. W., Mar. 2002; Vol. 4656, pp 1–9.

(77) Longenecker, J. G. High-Gradient Nanomagnet-On-Cantilever Fabrication For Scanned Probe Detection Of Magnetic Resonance., Dissertation, Cornell University, Jan. 2013.

(78) Stepankin, V. Magnetically aligned polycrystalline dysprosium as ultimate saturation ferromagnet for high magnetic field polepieces. *Physica B: Condensed Matter* **May 1995**, *211*, 345–347.

(79) Donald Lawrence Strandburg Electrical and magnetic properties of holmium in single crystals., Ph.D. Thesis, Iowa State University of Science and Technology, 1961.

(80) Vansek, P. In *CRC Handbook of Chemistry and Physics, 95th Edition*, Haynes, W. M., Ed., 95 edition; CRC Press: Boca Raton, Fla., June 2014.

(81) Ramezanalizadeh, H.; Heshmati-Manesh, S. Mechanochemical Reduction of MoO3 Powder by Al and Si to Synthesize Nanocrystaline MoSi2. *Int. J. Mod. Phys. Conf. Ser.* **Jan. 2012**, *05*, 119–126.

(82) Krill, C. E.; Merzoug, F.; Krauss, W.; Birringer, R. Magnetic properties of nanocrystalline Gd and W/Gd. *Nanostructured Materials* **1997**, *9*, 455–458.

(83) Behrendt, D. R.; Legvold, S.; Spedding, F. H. Magnetic Properties of Dysprosium Single Crystals. *Phys. Rev.* **Mar. 1958**, *109*, 1544–1547.

(84) Knitel, M. J.; Dorenbos, P.; van Eijk, C. W. E.; Plasteig, B.; Viana, B.; Kahn-Harari, A.; Vivien, D. Photoluminescence, and scintillation/thermoluminescence yields of several Ce3+ and Eu2+ activated borates. *Nuclear Instruments and Methods in Physics Research Section A: Accelerators, Spectrometers, Detectors and Associated Equipment* **Apr. 2000**, *443*, 364–374.

(85) McKigney, E. A.; Del Sesto, R. E.; Jacobsohn, L. G.; Santi, P. A.; Muenchausen, R. E.; Ott, K. C.; Mark McCleskey, T.; Bennett, B. L.; Smith, J. F.; Wayne Cooke, D. Nanocomposite scintillators for radiation detection and nuclear spectroscopy. *Nuclear Instruments and Methods in Physics Research Section A: Accelerators, Spectrometers, Detectors and Associated Equipment* **Aug. 2007**, *579*, 15–18.

(86) Gollub, S.; Harl, R.; Rogers, B.; Walker, D. Displacement damage from particle radiation in yttrium borate phosphor doped with cerium(III) or europium(III). *Journal of Luminescence* **Apr. 2014**, *148*, 267–273.

(87) Boyer, D; Bertrand, G; Mahiou, R A spectroscopic study of the vaterite form YBO3:Eu3+processed by solgel technique. *Journal of Luminescence* **Aug. 2003**, *104*, 229–237.

(88) Xu, C.; Watkins, B. A.; Sievers, R. E.; Jing, X.; Trowga, P.; Gibbons, C. S.; Vecht, A. Submicron-sized spherical yttrium oxide based phosphors prepared by supercritical CO2-assisted aerosolization and pyrolysis. *Applied Physics Letters* **Sept. 1997**, *71*, 1643–1645.

(89) Jin, D.; Yu, X.; Xu, X.; Wang, L.; Wang, L.; Wang, N. Hydrothermal synthesis of amorphous spherical-shaped YBO3:Eu3+ and its photoluminescence property. *J Mater Sci* **Sept. 2009**, *44*, 6144–6148.

(90) Zhang, X.; Marathe, A.; Sohal, S.; Holtz, M.; Davis, M.; Hope-Weeks, L. J.; Chaudhuri, J. Synthesis and photoluminescence properties of hierarchical architectures of YBO3:Eu3+. *J. Mater. Chem.* **Mar. 2012**, *22*, 6485–6490.

(91) Chen, J.; Guo, H.; Li, Z.; Zhang, H.; Zhuang, Y. Near-infrared quantum cutting in Ce3+, Yb3+ co-doped YBO3 phosphors by cooperative energy transfer. *Optical Materials* **July 2010**, *32*, 998–1001.

(92) Wei; Sun; Liao; Yin; Jiang; Yan; L, S. Size-Dependent Chromaticity in YBO3:Eu Nanocrystals: Correlation with Microstructure and Site Symmetry. *J. Phys. Chem. B* **Oct. 2002**, *106*, 10610–10617.

(93) Tukia, M.; Hls, J.; Lastusaari, M.; Niittykoski, J. Eu3+ doped rare earth orthoborates, RBO3 (R = Y, La and Gd), obtained by combustion synthesis. *Optical Materials* **July 2005**, *27*, 1516–1522.

(94) Smirnova, R. I.; Blank, Y. S.; Rumyantseva, T. Y. The dependence of the cathode -luminescence properties of YBO3 Ce on the concentration of cerium. *J Appl Spectrosc* **Sept. 1971**, *15*, 1169–1172.

(95) Shinde, K. N.; Dhoble, S. J.; Swart, H. C.; Park, K. In *Phosphate Phosphors for Solid-State Lighting*; Springer Berlin Heidelberg: Berlin, Heidelberg, 2012; Vol. 174, pp 41–59.

(96) Brakefield, B. L.; Gollub, S.; Walker, D. The Effect of Cerium Concentration on YBO3:Ce3+. *Young Scientist Journal* **2013**, *3*.

(97) Sharma, P. K.; Dutta, R. K.; Pandey, A. C. Size dependence of EuO charge transfer process on luminescence characteristics of YBO_3:Euˆ3+ nanocrystals. *Optics Letters* **July 2010**, *35*, 2331.